Title
Rational Design of Nanocatalysts for Renewable Energy Conversion

Author
Chen, Shouping

Publication Date
2021

Peer reviewed|Thesis/dissertation

Rational Design of Nanocatalysts for Renewable Energy Conversion

By

Shouping Chen

A dissertation submitted in partial satisfaction of the

requirements for the degree of

Doctor of Philosophy

in

Engineering – Materials Science and Engineering

in the

Graduate Division

of the

University of California, Berkeley

Committee in charge:

Professor Peidong Yang, Chair
Professor Junqiao Wu
Professor Bryan D. McCloskey

Fall 2021

Shouping Chen

Fall 2021

Abstract

Rational Design of Nanocatalysts for Renewable Energy Conversion

by

Shouping Chen

Doctor of Philosophy in Engineering – Materials Science and Engineering

University of California, Berkeley

Professor Peidong Yang, Chair

Increasing fossil fuel consumption and CO_2 emission have raised great concerns about our energy and environment future. In order to solve these problems, on the one hand, it is critical to develop alternative, renewable energy sources, such as fuel cell powered by H_2, on the other hand, it is also important to reduce the existing CO_2 into value-added products, such as fuels and fine chemicals. Electrocatalysis using nanomaterials plays an essential role in completing these two tasks by transforming the reactants into the target products efficiently along with the energy conversion process. The activity, stability, and selectivity of nanocatalysts highly depend on their structures, which require careful and rational design to achieve desired properties. Therefore, this dissertation focuses on the development of multiple effective strategies to improve the performance of different nanocatalysts for either fuel cell or CO_2 reduction reaction (CO_2RR) electrocatalysis.

First, post-synthesis treatment has been recognized as a key step to tailor the catalytic behavior of Pt-based alloys. In the second chapter, we present the effects of catalyst processing on the electrocatalytic property of Pt−Ni nanoframes for cathodic oxygen reduction reaction (ORR) in fuel cell. The Pt−Ni nanoframes are made by corroding the Ni-rich phase from solid rhombic dodecahedral particles. Among the three different corrosion procedures, electrochemical corrosion leads to the highest initial specific activity by retaining more Ni in the nanoframes. However, the high activity gradually goes down in a subsequent stability test due to continuous Ni loss and concomitant surface reconstruction. In contrast, the best stability is achieved by a more-aggressive corrosion using oxidative nitric acid. Although the initial activity is compromised, this procedure imparts a less-defective surface, and thus, the specific activity drops by only

7% over 30,000 potential cycles. These results indicate a delicate trade-off between the activity and stability of Pt−Ni nanoframe electrocatalysts.

Second, controlled synthesis of nanoparticles with optimal morphology and composition is crucial to promoting their catalytic performance. In the third chapter, we demonstrate the integration of highly open nanoframe morphology and catalytically active Pt−Co composition to develop Pt−Co nanoframes. Their ORR mass activity in acidic media is as high as 0.40 A mg_{Pt}^{-1} initially and 0.34 A mg_{Pt}^{-1} after 10,000 potential cycles at 0.95 V versus reversible hydrogen electrode (V_{RHE}). Moreover, their mass activity for anodic methanol oxidation reaction (MOR) in alkaline fuel cell is up to 4.28 A mg_{Pt}^{-1} and is 4-fold higher than that of commercial Pt/C catalyst. Experimental studies indicate that the weakened binding of intermediate carbonaceous poisons contributes to the enhanced MOR behavior. More impressively, the Pt−Co nanoframes also show excellent stability under long-term testing, which could be attributed to the negligible electrochemical Co dissolution.

Third, introducing a second material, such as the metal−organic framework (MOF), is a promising strategy to add catalytic functions beyond metal nanoparticles. In the fourth chapter, we demonstrate the combination of Pt−Ni nanoframe and zeolitic imidazolate framework-8 (ZIF-8), which is a special MOF, into an individually encapsulated frame-in-frame structure. Via surface functionalization, the Pt−Ni nanoframe is first embedded in ZIF-8 to achieve a single core−shell structure, as evidenced by the three-dimensional tomography. The growth trajectory of such frame-in-frame nanocomposite is tracked, revealing that ZIF-8 first nucleates in the solution, then attaches to the surface of the nanoframe, and finally grows to capture the entire nanoframe, enabling the one-in-one encapsulation. Next, by utilizing ZIF-67 as the sacrificial layer, the Pt−Ni nanoframe is further solely encased in ZIF-8 to form a single yolk−shell structure, which has a cavity between the core and the shell. The obtained frame-in-frame structures have potential applications in size-selective or tandem catalysis to produce fine chemicals.

Fourth, long-range atomic ordering in nanocrystals holds the promise of unique catalytic properties for many reactions. In the fifth chapter, we report the preparation of Cu_3Au intermetallic nanowires by using Cu@Au core−shell nanowires as the precursors. With appropriate Cu/Au stoichiometry, the Cu@Au core−shell nanowires are transformed into fully ordered Cu_3Au nanowires under thermal annealing. Thermally-driven atomic diffusion, which is facilitated by the abundant twin boundaries, accounts for the ordering process. The resulting Cu_3Au intermetallic nanowires have uniform and accurate atomic positioning in the crystal lattice, which enhances the nobility of Cu. No obvious copper oxides are observed in fully ordered Cu_3Au nanowires after annealing in air at 200 °C, a

temperature that is much higher than those observed in Cu@Au core−shell and pure Cu nanowires. The acquired Cu_3Au intermetallic nanowires are promising candidates for either ORR or CO_2RR electrocatalysis.

Fifth, covalently bonded surface ligands often block the active metal sites and limit the reactivity of nanocluster catalysts. In the sixth chapter, we investigate the ligand removal process for Au_{25} nanoclusters using both thermal and electrochemical treatments, as well as its impact on the CO_2 electroreduction to CO. The Au_{25} nanoclusters are synthesized with 2-phenylethanethiol as the capping agent and anchored on sulfur-doped graphene. The thiolate ligands can be readily removed under either thermal annealing at ≥180 °C or electrochemical biasing at ≤ -0.5 V_{RHE}. However, these ligand-removing conditions also trigger the structural evolution of Au_{25} nanoclusters concomitantly. The thermally and electrochemically treated Au_{25} nanoclusters show enhanced activity and selectivity for the electrochemical CO_2-to-CO conversion than their pristine counterpart, which is attributed to the increased exposure of undercoordinated Au sites on the surface after ligand removal.

Table of Contents

List of Publications

1. S. Chen,† M. Li,† S. Yu, S. Louisia, W. Chuang, M. Gao, C. Chen, J. Jin, M. B. Salmeron, and P. Yang,* "Ligand Removal of Au_{25} Nanoclusters by Thermal and Electrochemical Treatments for Selective CO_2 Electroreduction to CO", *The Journal of Chemical Physics* **2021**, *155*, 051101.
2. Z. Niu,† S. Chen,† Y. Yu, T. Lei, A. Dehestani, K. Schierle-Arndt, and P. Yang,* "Morphology-Controlled Transformation of Cu@Au Core−Shell Nanowires into Thermally Stable Cu_3Au Intermetallic Nanowires", *Nano Research* **2020**, *13*, 2564–2569.
3. S. Chen, X.-Y. Liu, J. Jin, M. Gao, C. Chen, Q. Kong, Z. Ji, G. A. Somorjai, O. M. Yaghi, and P. Yang,* "Individually Encapsulated Frame-in-Frame Structure", *ACS Materials Letters* **2020**, *2*, 685–690.
4. S. Chen,† M. Li,† M. Gao, J. Jin, M. A. van Spronsen, M. B. Salmeron, and P. Yang,* "High-Performance Pt–Co Nanoframes for Fuel-Cell Electrocatalysis", *Nano Letters* **2020**, *20*, 1974–1979.
5. S. Chen,† Z. Niu,† C. Xie, M. Gao, M. Lai, M. Li, and P. Yang,* "Effects of Catalyst Processing on the Activity and Stability of Pt–Ni Nanoframe Electrocatalysts", *ACS Nano* **2018**, *12*, 8697–8705.
6. P.-C. Chen, M. Li, J. Jin, S. Yu, S. Chen, C. Chen, M. B. Salmeron, and P. Yang,* "Heterostructured Au–Ir Catalysts for Enhanced Oxygen Evolution Reaction", *ACS Materials Letters* **2021**, *3*, 1440–1447.
7. M. Li,† B. Zhang,† T. Cheng, S. Yu, S. Louisia, C. Chen, S. Chen, S. Cestellos-Blanco, W. A. Goddard III, and P. Yang,* "Sulfur-Doped Graphene Anchoring of Ultrafine Au25 Nanoclusters for Electrocatalysis", *Nano Research* **2021**, *14*, 3509–3513.
8. B. Zhang, C. Chen, W. Chuang, S. Chen, and P. Yang,* "Size Transformation of the $Au_{22}(SG)_{18}$ Nanocluster and Its Surface-Sensitive Kinetics", *Journal of the American Chemical Society* **2020**, *142*, 11514–11520.

† Indicates equal contribution. * Indicates corresponding author.

List of Figures and Tables

Acknowledgements

First, I would like to thank my advisor, Professor Peidong Yang, for his great guidance and support during my Ph.D. career. As one of the best scientists in the world, Peidong has deeply inspired me on how to ask big scientific questions, how to develop scientific thinking, and how to conduct scientific research proactively and efficiently. In addition to science, Peidong has also offered me tremendous help in other aspects, for example, when I met difficulties in personal life, when I pursued my future career, etc. I feel very lucky and honored to complete my Ph.D. degree under his mentoring.

Next, I want to thank my collaboration faculty members, Professor Miquel B. Salmeron, Professor Omar M. Yaghi, and Professor Gabor A. Somojai, for their insightful advice on my various projects. I also want to thank my dissertation and qualifying exam committee members, Professor Junqiao Wu, Professor Bryan D. McCloskey, Professor Ting Xu, and Professor Mary Scott, for kindly instructing me to develop my Ph.D. dissertation.

Then, I must thank all the graduate students and postdoctoral fellows that I have been working with over the years. In particular, I would like to thank my mentors, Dr. Mufan Li, Dr. Zhiqiang Niu, and Dr. Nigel B. Becknell, for teaching me the experimental skills and training me on how to become an independent researcher. And also, I would like to thank my collaborators, Sunmoon Yu, Sheena Louisia, Dr. Xiao-Yuan Liu, Chubai Chen, Dr. Chenlu Xie, Wesley Chuang, Mengyu Gao, Jianbo Jin, Dr. Teng Lei, Dr. Minliang Lai, Dr. Qiao Kong, Dr. Yi Yu, Dr. Zhe Ji, Dr. Matthijs A. van Spronsen, and Xiao Zhao, for their considerable contributions in different projects.

Furthermore, I am grateful to meet all my friends at Berkeley, including but not limited to Jingyang Wang, An Ju, Hongyu Zhang, Yonghuan Ren, Huazhe Xu, Qianyi Xie, Yang Gao, Qing Tian, Yixuan Liu, and Ruiyang Song. We had a wonderful time travelling, hanging out, playing sports, eating and drinking, etc., which made my life more colorful, and cheered me up when I was down.

Last and most importantly, I want to express my most sincere gratitude to my parents and family. Their everlasting love and support have always motivated me to overcome the challenges and pursue my goals. They are always ready to help whenever I need, and I would not be able to complete this journey without their accompany.

Chapter. 1 Introduction

1.1 Energy and Environment Challenges

Energy and environment issues have drawn significant attention in human society since the Industrial Revolution.[1-3] Over the past decades, two major concerns have been raised. The first one is the increasing fossil fuel consumption. Although the utilization of fossil fuel has vastly facilitated the development of modern civilization, its fast-growing usage now becomes a threat to our energy future. The global fossil fuel consumption has risen by more than 10 times over the last hundred years (Figure 1-1a), and the years of global coal, oil, and gas reserves left were reported to be only 114, 51, and 53, respectively, in 2016.[4] Hence, the overreliance on fossil fuel may lead to serious energy shortage in the future. As a result of massive fossil fuel combustion, the second concern is the ascending CO_2 emission. The world CO_2 release has increased by more than 15 folds since 1900s (Figure 1-1b), resulting in a continuous climb in atmospheric CO_2 concentration at the same time.[4,5] The anthropogenic CO_2 emission has caused catastrophic damages to the climate and environment, including global warming,[6] glaciers melting,[7] sea-level rise,[8] ocean acidification,[9,10] ecological disruption,[11,12] etc. Moreover, it also brings economic loss and health risks to human beings.[13]

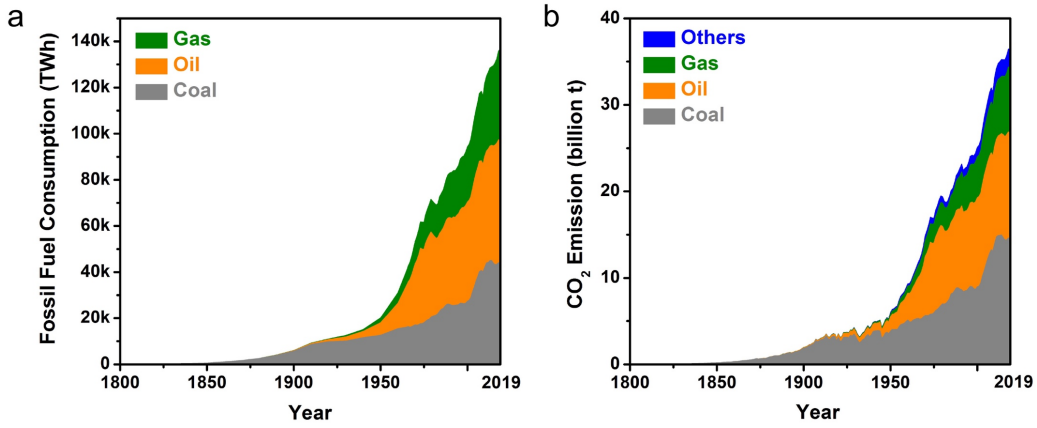

Figure 1-1 Fossil fuel consumption and CO_2 emission. Global (a) fossil fuel consumption and (b) CO_2 emission per year from 1800 to 2019. Data source: Our World in Data.[4]

These two challenges are correlated with each other in the carbon cycle (Figure 1-2).[14,15] On the one hand, the conversion of CO_2 into biomass and fossil fuel is slowly conducted by nature, which requires as long as millions of years to complete. However, on the other hand, the combustion of fossil fuel into CO_2 to produce heat or electricity is dramatically accelerated by the industrialization that happened within the recent hundreds of years, thus breaking the balance of natural carbon cycle. In order to solve the aforementioned

problems, two aspects must be considered. First, it is important to develop alternative carbon-free and renewable energy sources to replace traditional fossil fuel, which helps to reduce the fossil fuel usage and CO_2 generation. In this respect, fuel cell with H_2 as the energy storage material is one of the most promising clean power supplies with H_2O as the only product.[16] Second, it is also essential to transform the existing CO_2 in the atmosphere into value-added chemicals, which assists to lower the CO_2 level and create fuels sustainably.

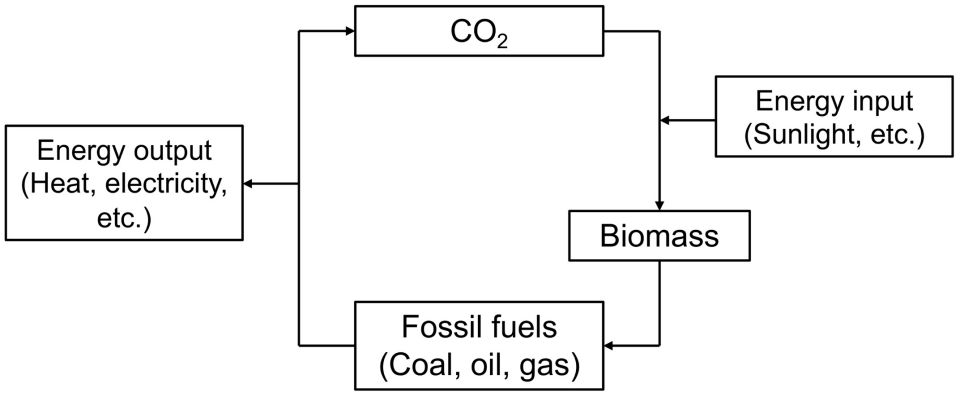

Figure 1-2 Carbon cycle. Schematic of material transformation and energy conversion in carbon cycle.

Electrocatalysis plays a key part in these material transformation and energy conversion technologies by employing electricity or electrons.[17-19] It is impressive as it can proceed at improved efficiency, rate, and selectivity.[20] The following introduction, as well as the entire dissertation, will focus on discussing fuel cell and CO_2 reduction reaction (CO_2RR) electrocatalysis as two prominent ways to tackle the energy and environment challenges in our society.

1.2 Fuel Cell Electrocatalysis

The most common fuel cell is the proton-exchange membrane fuel cell (PEMFC), which has wide applications at the transportation sector.[21,22] In a PEMFC, H_2 is the fuel at the anode and O_2 is the oxidant at the cathode, and these two electrodes are separated by a proton-exchange membrane, which is responsible for transferring protons (Figure 1-3). So, the anodic reaction is hydrogen oxidation reaction (HOR), i.e., $H_2 - 2e^- \rightarrow 2H^+$, and the cathodic reaction is oxygen reduction reaction (ORR), i.e., $O_2 + 4e^- + 4H^+ \rightarrow 2H_2O$, both of which are performed by the catalyst layer (Figure 1-3).

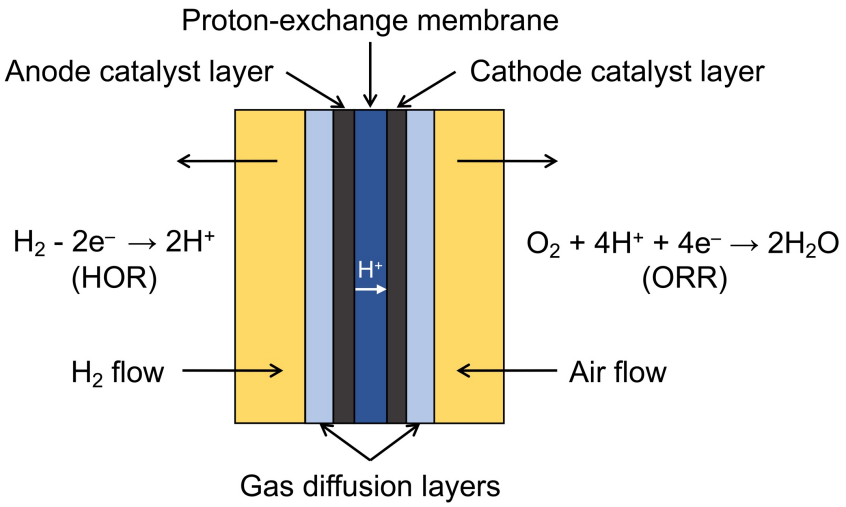

Figure 1-3 Proton-exchange membrane fuel cell. Components of a PEMFC.

The overall performance of fuel cell is primarily limited by the sluggish cathodic ORR, which requires a relatively large overpotential to drive.[23] The proposed mechanisms for ORR contain two rate-limiting steps, which are the initial adsorption and protonation of gaseous O_2, as well as the desorption of H_2O after final protonation.[24,25] For each step, its kinetics is determined by the interaction between the metal atom on the catalyst surface and the oxygen atom in the corresponding reaction intermediate.[24] According to the scaling relations, the adsorption energies of different oxygenated intermediates, such as O*, HO*, and HOO* (* represents the active site), on the metal surface scale linearly because of their analogous oxygen−metal atomic bonding motif.[26,27] Hence, when the binding energy is too low, the initial adsorption of O_2 slows down, and when the binding energy is too high, the final desorption of H_2O becomes sluggish. As a consequence, the best ORR catalyst should possess neither too strong nor too weak affinity to the oxygenated species to achieve the highest activity, thereby forming the volcano plot.[24,26,27]

Among all the metal elements in the periodic table, Pt exhibits the best ORR activity due to its optimal binding energy of oxygen in the volcano plot (Figure 1-4a).[28] Unfortunately, the scarcity and high cost of Pt set a major restriction on the commercialization of fuel cells.[29] Therefore, the catalyst design principle is to improve the ORR performance while reducing the amount of Pt loading. As shown in the volcano plot, Pt still binds to oxygen more strongly than the true optimum (Figure 1-4a). To resolve this, alloying Pt with a proper transition metal can downshift its *d*-band center and decrease its oxygen binding energy, thus realizing a major breakthrough in further increasing the ORR rate (Figure 1-4b).[30,31] This can be explained by the *d*-band theory: the lowering of Pt *d*-band center after transition metal doping causes greater filling of the metal−adsorbate antibonding states, which, in turn, weakens the Pt−O bonding.[32-34] Among all the transition metals,

Ni is the most popular candidate to alloy with Pt due to its ease of synthesis and superior ORR property.[35,36] In addition, introducing compressive lattice strain is another method to downshift the *d*-band of Pt and weaken the adsorption of oxygen, leading to an ORR activity enhancement.[37,38] By following the above guidance, Pt-based alloy nanoparticles with various size,[39,40] morphology,[41-45] composition,[46,47] etc., have been widely explored for catalyzing ORR efficiently.

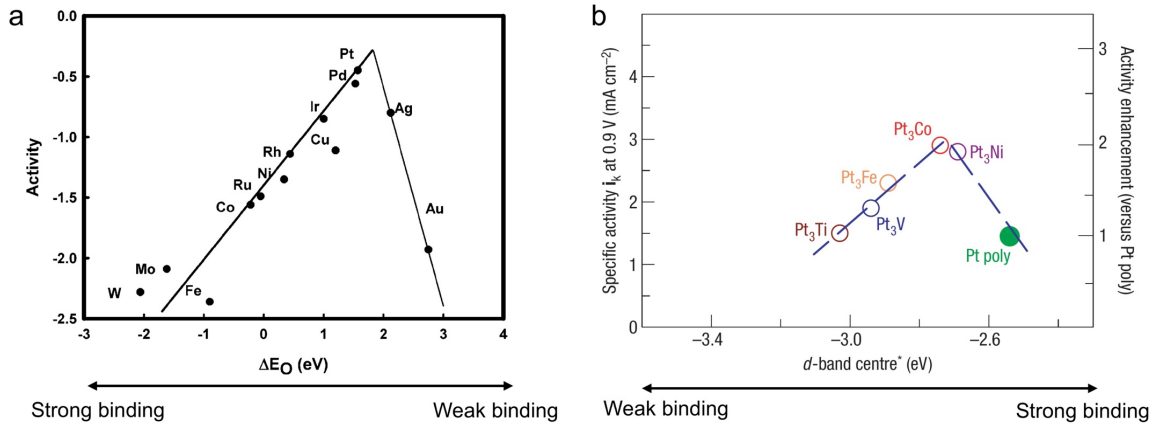

Figure 1-4 ORR volcano plots. ORR volcano plots for (a) single metal elements and (b) Pt-based alloys, which demonstrate the relationships between ORR activity and oxygen binding energy. (a) Reproduced with permission from ref 28. Copyright 2004 American Chemical Society.[28] (b) Reproduced with permission from ref 30. Copyright 2007 Nature Publishing Group.[30]

Besides activity, the issue of long-term degradation still remains as a challenge for ORR catalysts. During the electrocatalysis, several problems including Pt dissolution, particle detachment, agglomeration, Ostwald ripening, carbon support corrosion, and transition metal leaching out can occur and result in poor stability.[48-50] In this regard, not only the activity but also the durability needs to be further promoted for the next generation of ORR catalysts.

The ORR electrochemical measurement is conducted through the rotating disk electrode (RDE), which can overcome the mass transport limitation by accelerating the transfer of O_2 molecules to the surface of the electrode.[51-53] And, the most general electrolyte for ORR test is $HClO_4$, which has the least interference with the Pt surface compared with other solutions, thus revealing the intrinsic catalytic behavior.[54-56] Lastly, there are some key ORR properties to evaluate: electrochemically active surface area (ECSA), specific activity and mass activity, and stability.[53,57,58] First, the ECSA is determined from the cyclic voltammogram (CV). In a CV, the charge associated with hydrogen underpotential deposition (H_{upd}) is used to calculate the total surface area, which is then divided by Pt mass loading to gain the ECSA (Figure 1-5a). Second, the specific and mass activities are obtained by normalizing the kinetic current to total surface area and Pt mass loading,

respectively. The kinetic current is derived from the ORR polarization curve at a certain potential, which is normally 0.95 (or 0.90) V versus reversible hydrogen electrode (V_{RHE}), using Koutecky−Levich (K−L) equation (Figure 1-5b):

$$\frac{1}{I} = \frac{1}{I_d} + \frac{1}{I_k}$$

where I is the total current, I_d is the diffusion current, and I_k is the kinetic current. Third, the stability refers to the ECSA, specific activity, and mass activity after given numbers of potential cycling, compared with the initial values (Figure 1-5c).

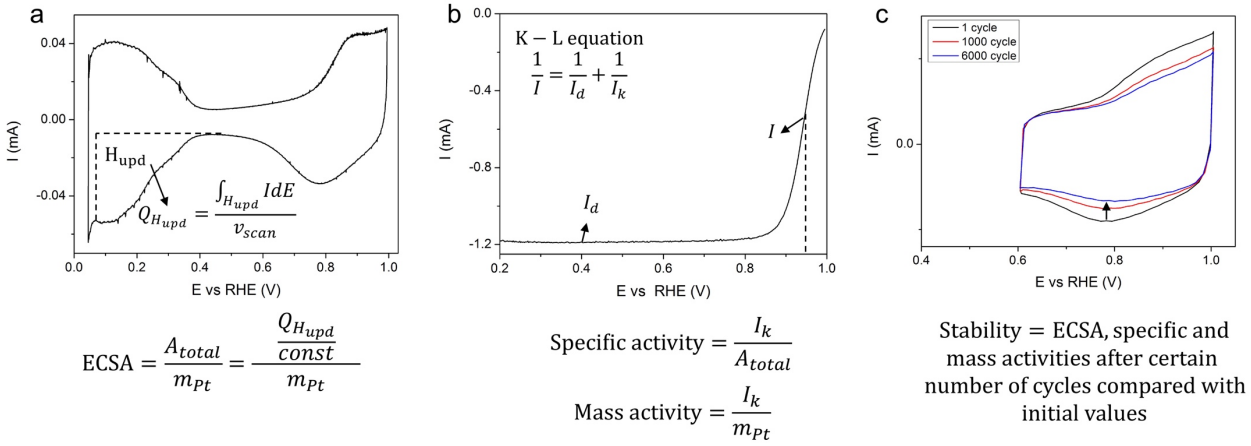

Figure 1-5 Evaluations of ORR properties. Calculations of (a) ECSA, (b) specific and mass activities, and (c) stability for the ORR measurement.

1.3 CO_2 Reduction Reaction Electrocatalysis

Compared with other common catalytic reactions, like aforementioned ORR, CO_2RR is a more complicated process because it can undergo various numbers of electron transfer and create a wide range of products (Figure 1-6).[18,59] These products can be classified by the number of carbon atoms (C_1, C_{2+}) or the number of electron transfer ($2e^-$ or $>2e^-$). Owing to its complexity, understanding the CO_2RR mechanism clearly is crucial for the rational catalyst design. The possible mechanistic pathways of CO_2RR can be divided into two parts. The first one is the C_1 product formation, which consists of $2e^-$ reduction to CO or formate and $>2e^-$ reduction to methane or methanol. In the formation of CO, CO_2 is adsorbed through the carbon atom, and the rate-limiting step is the first single electron transfer for CO_2 activation.[60,61] The formate production shares a similar pathway to CO, except that the intermediate binds via the oxygen atom.[62,63] For the $>2e^-$ products (methane and methanol), *CO is the key intermediate and its protonation is the rate-determining step, which is pH dependent on the standard hydrogen electrode (SHE) scale.[64-66] The C_1 production requires the catalyst to have an appropriate binding energy to the carbon (or oxygen) atom. The second part is the C_{2+} product formation, including

ethylene, ethanol, etc. For all these >2e⁻ products, *CO is still the critical intermediate and its dimerization is the rate-limiting step, which is pH independent on the SHE scale as it is decoupled from proton transfer.[64,67,68] In addition to *CO dimerization, alternate mechanisms for C−C coupling have also been reported, such as *CH_2 dimerization,[69,70] *CH_3 dimerization,[71] CO insertion,[69,70] etc. The C_{2+} production demands that the catalyst should have the capability to form C−C bonds.

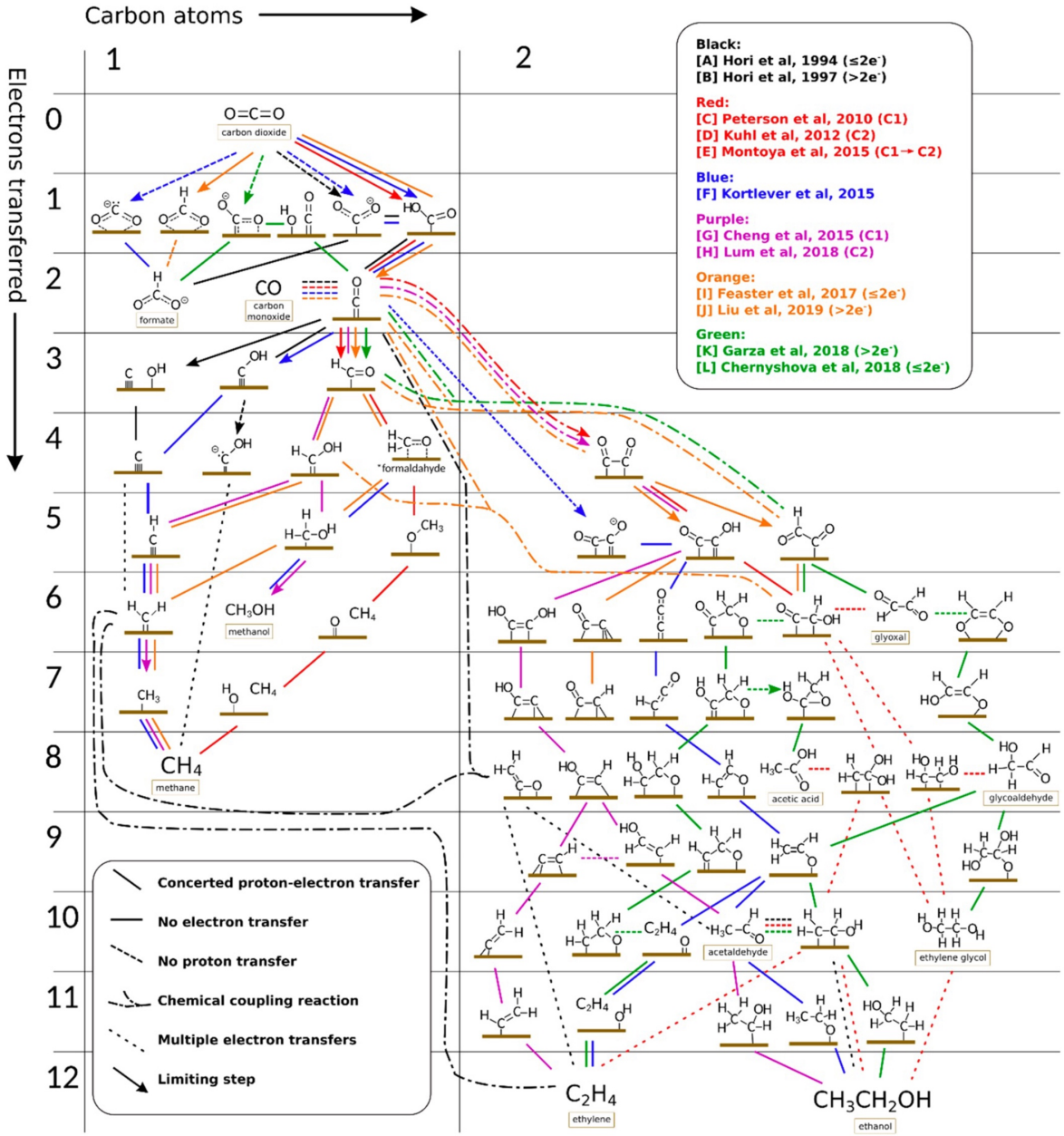

Figure 1-6 Mechanistic pathways of CO_2RR. Proposed mechanistic pathways of CO_2RR to C_1 and C_2 products on polycrystalline Cu. Reproduced with permission from ref 59. Copyright 2019 American Chemical Society.[59]

In an attempt to promote the CO_2RR electrocatalysis, a couple of goals must be pursued. First, since CO_2RR is normally carried out in the aqueous solution, hydrogen evolution reaction (HER) exists as a non-negligible competing reaction. Table 1-1 summarizes the standard reduction potentials of common CO_2RR products on the RHE scale, which is a thermodynamic zero point for reducing protons to H_2.[18,59] Although the majority of the thermodynamic potentials are slightly above 0 V_{RHE}, in practice, an overpotential of as large as hundreds of mV is typically needed to overcome the kinetic barrier and initiate the CO_2RR, which implies that HER can also readily take place at the applied negative potential.[18] So, the ideal catalyst should be specifically active for CO_2RR and be inactive for HER. Second, a good catalyst should be able to reduce CO_2 into valuable products at a relatively low overpotential and a decent rate, which can increase the energy efficiency. Third, since CO_2RR can lead to a variety of products, a desired catalyst should generate only one or a few of them. Otherwise, the post-reaction product separation will involve additional power input and cost.[72] Fourth, since the multicarbon products generally have higher industrial and economic values, a promising electrocatalyst should direct CO_2RR into the $>2e^-$ pathway and create high-order products.[73,74] Fifth, the CO_2RR also needs to maintain a great stability in the long term. It has been reported that the structural degradation of catalysts over time can trigger the performance decay, which should be prohibited.[75,76]

Table 1-1 Standard reduction potentials of CO_2RR products. The potentials are presented on the RHE scale.[18,59]

Number of carbons	Product	E (V_{RHE})
C_1	Carbon monoxide (CO)	−0.10
	Formic acid (HCOOH)	−0.12
	Methane (CH_4)	0.17
	Methanol (CH_3OH)	0.03
C_2	Ethylene (C_2H_4)	0.08
	Ethane (C_2H_6)	0.14
	Ethanol (C_2H_5OH)	0.09
	Acetaldehyde (CH_3CHO)	0.06
	Acetic acid (CH_3COOH)	0.11
C_3	Propanol (C_3H_7OH)	0.10
	Acetone (CH_3COCH_3)	0.10

The CO_2RR metal catalysts can be categorized by the products they can make, which depends on their adsorption energies for *CO and *H (Figure 1-7).[77] First, if the metals bind to *CO strongly, such as Pt, they will be poisoned by *CO and mostly generate H_2. Next, on the contrary, the metals that bind to *CO weakly, for example, Au and Ag, will

favor the production of CO. Up to now, Au and Ag nanoparticles with different size,[78,79] shape,[80,81] and ligand[82] have been demonstrated to be highly selective for the CO_2-to-CO electroreduction. Finally, among all the elements, Cu is the only candidate capable of creating >2e⁻ products, which could be related to its unique negative binding energy for *CO but positive binding energy for *H. Therefore, Cu catalysts are of special interest and attract the most research focus for CO_2RR. So far, a good number of Cu structures have been shown competent to synthesize a useful amount of C_{2+} products, containing electrochemically scrambled Cu nanoparticles,[83,84] highly fragmented Cu structures,[85] Cu nanocavities with confiement,[86] Cu/N-doped nanodiamond interface,[87] Cu nanoflowers with large surface area,[88] Cu nanowires with stepped surface,[89] Cu nanosheets exposing (111) surface,[90] etc. Coupling Cu with other metals is a widely used strategy to further enhance its CO_2RR performance. Two effects have been identified in these bimetallic (or multimetallic) systems.[18,59] The first one is the electronic effect, i.e., the alloying of Cu with other metals can influence its electronic structure and alter its binding strength to the intermediates.[91] For example, Cu−Zn alloys[92] and Cu−Ag surface alloys[93] facilitate the formation of multicarbon products. The second one is the tandem effect, i.e., other metals, such as Ag or Au, can first produce CO and then spill it over to Cu for further reduction. For instance, a mixture of Cu and Ag particles,[94] as well as Au particles on Cu foil,[95] are very active and selective for the CO_2-to-C_{2+} transformation.

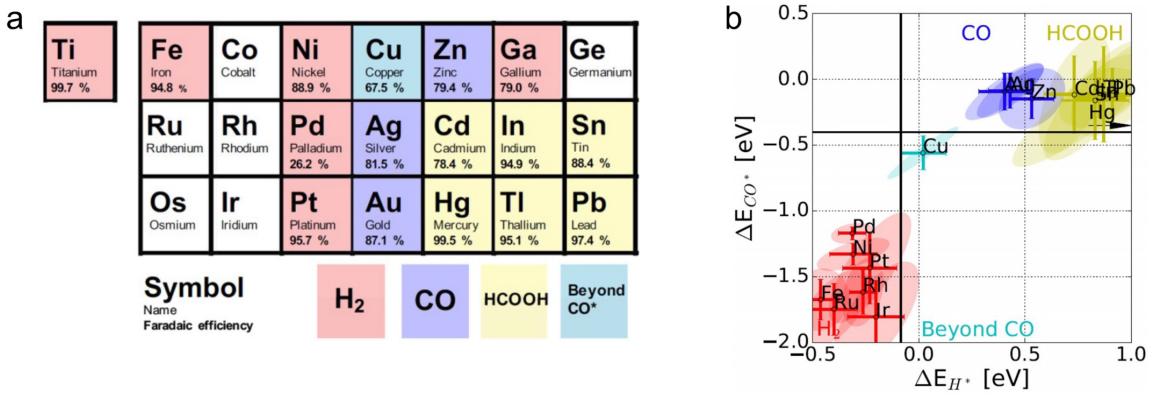

Figure 1-7 Metal classification of CO_2RR. Metal catalysts categorized by their major products (H_2, CO, HCOOH, and beyond CO) of CO_2RR, according to (a) the position in periodic table and (b) the binding energies to *CO and *H. Reproduced with permission from ref 77. Copyright 2017 Wiley-VCH Verlag GmbH & Co. KGaA, Weinheim.[77]

Traditionally, the CO_2RR electrochemical measurement is performed in H-cell in CO_2-saturated 0.1 M $KHCO_3$ aqueous solution. More recently, the flow cell in combination with gas diffusion electrode (GDE) has been developed for testing CO_2RR in alkaline or neutral pH, which can eliminate the slow gas transport kinetics and increase the local concentration of CO_2 by constructing a three-phase interface, thus boosting the catalytic

reactivity.[96,97] For CO_2RR, the gas products are analyzed by gas chromatography (GC), and the liquid products are detected by proton nuclear magnetic resonance (^{1}H NMR) spectroscopy. The CO_2RR properties to be estimated consist of the following. First, the activity of a product refers to its partial current density, which equals the partial current responsible for generating this product normalized to geometric area, total surface area, or metal mass loading. Second, the selectivity of a product is represented by its faradaic efficiency, which is the amount of charge consumed for this product divided by the total charge passed. Third, the stability is the change of activity and selectivity over long-term electrocatalysis.

1.4 Nanocatalyst Design

Since catalysis only happens on the surface, nanomaterials become appealing candidates due to the high surface area-to-volume ratio.[98] Till now, a wide range of design principles have been explored for diverse nanocatalysts towards different chemical reactions. Some of the published strategies are listed below in this section.

Facet control. According to the studies on single-crystal surfaces, different planes with unique atomic arrangements have distinct binding energies to the reaction intermediates and thus different catalytic properties.[99] The same rule is also applicable to nanocatalysts. For example, Pt−Ni octahedral nanoparticles exposing (111) surfaces are notably more active for ORR than Pt−Ni cubic nanoparticles exposing (100) surfaces, due to the peak adsorption energies of oxygenated species on (111) planes.[100,101] Besides, Cu nanosheets enclosed by (111) facets prefer the production of acetate compared with Cu nanocubes enclosed by (100) facets, which is attributed to the suppression of ethylene and ethanol formation on (111) surfaces.[90]

Shape control. As a result of the catalytic impacts from facets, nanoparticles featuring various shapes also possess distinct reactivity since they are covered by a collection of different surfaces. Led by the rapid advancement in colloidal synthesis, so far, abundant well-defined morphologies have been realized for metal nanocatalysts, including zero-dimensional (0D) nanopolyhedra[100] or nanocages[44], one-dimensional (1D) nanowires[102], as well as two-dimensional (2D) nanosheets[90] or nanoplates[42]. Among them, the Pt−Ni nanoframes attract a lot of research interest owing to their highly open structure with three-dimensional (3D) molecular accessibility.[45] As shown in Figure 1-8, the starting materials are solid Pt−Ni rhombic dodecahedra, which contain two segregated phases: Pt-rich phase and Ni-rich phase. The Pt-rich phase is only concentrated on the edges of the polyhedron, while the Ni-rich phase is homogeneously distributed inside the particle. During the following corrosion by acids or organic solvents, the Ni-rich phase is etched

away, whereas the Pt-rich phase is maintained to construct the hollow framework. As for catalysis, the Pt−Ni nanoframes exhibit remarkable ORR activity. This Pt-based nanoframe structure will be extensively discussed in Chapter 2, 3, and 4.

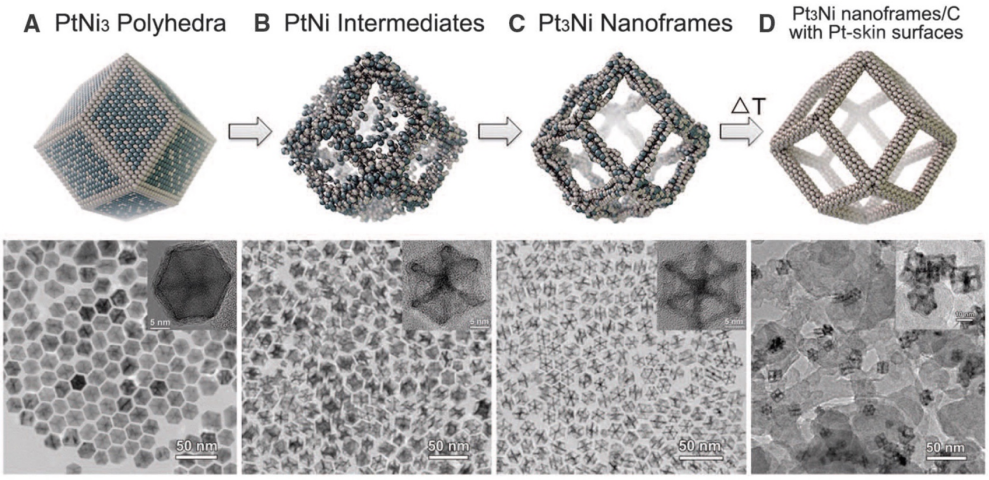

Figure 1-8 Formation process of Pt−Ni nanoframes. (a) Initial solid Pt−Ni rhombic dodecahedra, (b) Pt−Ni intermediates, (c) final hollow Pt−Ni nanoframes, and (d) annealed Pt−Ni nanoframes on carbon. Reproduced with permission from ref 45. Copyright 2014 American Association for the Advancement of Science.[45]

Composition control. The elemental composition and its distribution can influence the catalytic behaviors by tuning the adsorption energies of reaction intermediates on metal surface.[92,103] In addition to colloidal synthesis, post-synthesis treatment, especially heat treatment, is an alternative method to apply composition control.[104] Thermal annealing at elevated temperature has been reported to be an elegant approach to producing active intermetallic nanocatalysts, which possess uniform and precise atomic positioning.[105,106] The ordering process of Cu−Au core@shell nanowires to form intermetallic nanowires under thermal treatment will be revealed in Chapter 5.

Size control. The size of nanoparticles affects the catalytic properties in two ways. First, it alters the surface area-to-volume ratio, i.e., the number of active sites exposed on the surface per unit mass. Second, it changes the coordination number of metal atoms, which has been recognized as an important influencing factor for catalysis, through altering the proportion of atoms at the surfaces, edges, and corners.[84,107,108] For instance, Pt and Au nanoparticles of various sizes demonstrate different electrocatalytic behaviors for ORR and CO_2RR, respectively.[40,78] In particular, the size of metal particles can be decreased to as small as sub-2 nm, entering the scope of nanoclusters. Because of their ultrafine size, these metal clusters have quantized energy levels and low coordination numbers, which offer superior catalytic performances.[109-111] Among them, Au_{25} nanoclusters are efficient

catalysts for CO_2-to-CO conversion.[111] Figure 1-9 shows that the crystal structure of Au_{25} clusters contains a Au_{13} icosahedral core surrounded by a shell of six –S–Au–S–Au–S– semiring motifs.[111] As a consequence, the whole Au_{25} cluster is protected by 18 thiolate ligands. This Au_{25} nanocluster structure and its ligand removal will be presented in more detail in Chapter 6.

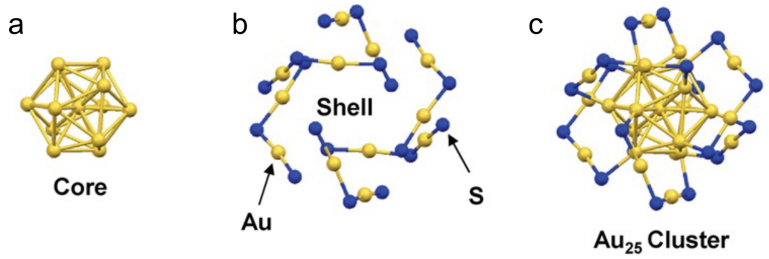

Figure 1-9 Structure of Au_{25} nanocluster. Structure of (a) Au_{13} icosahedral core, (b) shell consisting of six Au_2S_3 semiring structures, and (c) entire Au_{25} cluster. Yellow spheres represent Au atoms and blue spheres represent S atoms. Reproduced with permission from ref 111. Copyright 2012 American Chemical Society.[111]

Ligand control. Although the ligands play a significant role in controlling the shape and size of nanoparticles during colloidal synthesis, some of them are detrimental to catalysis and need to be removed.[112] For example, the thiolate ligands on Au_{25} clusters will impose steric restriction to molecular reactants and block the active surface centers from being exposed for catalysis.[113] Theoretical calculations have predicted that the ligand-removed sites on Au_{25} nanoclusters are responsible for improved CO_2RR property.[114] In contrast, some other ligands are instead beneficial to catalysis. For instance, tetradecylphosphonic acid (TDPA) ligands can construct a special interlayer on Ag, Au, or Pd nanoparticles for high-specificity CO_2 electroreduction to CO.[82] Furthermore, the surfactant tailoring on Cu can enhance the CO_2-to-ethylene conversion by adjusting the binding of *CO.[115]

In the subsequent chapters in this dissertation, we will present our own findings on the rational design of different catalysts, including Pt-based nanoframes, Cu−Au nanowires, and Au_{25} nanoclusters, for fuel cell and CO_2RR electrocatalysis.

Chapter. 2 Effects of Catalyst Processing on the Activity and Stability of Pt−Ni Nanoframe Electrocatalysts

The contents and figures of this chapter are adapted or reprinted with permission from S. Chen,† Z. Niu,† C. Xie, M. Gao, M. Lai, M. Li, and P. Yang,* "Effects of Catalyst Processing on the Activity and Stability of Pt–Ni Nanoframe Electrocatalysts", *ACS Nano* **2018**, *12*, 8697–8705. DOI: 10.1021/acsnano.8b04674. [116]

2.1 Preface

Post-synthesis treatment plays an important role in improving the catalytic performance. In Chapter 2, we present the effects of catalyst processing on the activity and stability of Pt−Ni nanoframe electrocatalysts for ORR. Among three different corrosion procedures, electrochemical corrosion results in the highest initial specific activity by retaining more Ni in the nanoframes, while nitric acid corrosion realizes the best stability by imparting a less-defective surface.

2.2 Introduction

The PEMFCs powered by H_2 from renewable sources serve as the most-promising power supplies for future transportation applications.[21] However, the high cost of Pt, which exhibits the highest activity for the overall efficiency-limiting cathodic ORR,[28] is the major limitation preventing the large-scale deployment of PEMFCs in automotive vehicles.[23] To achieve commercially viable PEMFCs, highly durable cathodic catalysts with low Pt loading are required. Pt-based alloys have been discovered to hold the promise to affordable PEMFCs due to their outstanding ORR activity.[30] Alloying Pt with a proper transition metal results in a downshift of the *d*-band center, which, in turn, weakens the Pt−OH_{ad} bonding and increases the ORR rate.[117,118] Different strategies, including size, shape, and composition control,[119,120] have been frequently used to optimize the activity and durability of Pt-based alloy catalysts.[44,100,102] The development of Pt−Ni octahedral nanoparticles is a representative example. As a nanoscale replica of the ideal (111) single-crystalline surface,[99] the Pt_3Ni octahedra are enclosed by high-coordination surface atoms that are favorable for the desorption of oxygenated species. Therefore, the Pt−Ni octahedra exhibit much-higher specific activity than the spherical analogues.[121,122]

Although the controlled synthesis plays an important role in the development of advanced ORR catalysts, post-synthesis treatment has been shown to be of equal importance in the tailoring of their catalytic behavior.[29,123-125] The near-surface structure and composition of freshly made nanostructures can change upon the exposure to air, moisture, heat, corrosive solvent, acid, and other unidentified environment factors. In particular, heat treatment is commonly adopted as a necessary step not only to form better contacts between catalytic particles and carbon support but also to induce the desired surface relaxation and reconstruction.[103,104,126-128] Studies have shown that carefully choosing the annealing temperature and atmosphere can generate an enhanced degree of alloying as well as an optimal extent of Pt surface enrichment. These structural changes have brought great benefits to both the ORR reactivity and durability.[103] Another widely used post-synthesis treatment is the pre-leaching of transition metals.[129-131] The electrochemical dissolution of transition metals during fuel cell operation can cause detrimental contamination to the membrane and ionomer.[29] Acid washing is therefore a necessity before the Pt-based alloy catalysts can be used in PEMFCs. Because the leaching of transition metals always starts from the topmost layers, a Pt-rich shell is concomitantly generated and, in turn, acts as a protective layer to prevent further acid corrosion of the transition metals. The as-obtained core−shell structures preserve a composition gradience and constitute one type of the most-active and -stable ORR catalysts.[131]

Our group recently developed the Pt−Ni nanoframe electrocatalysts by manipulating the spatial positioning of Pt and Ni in the solid rhombic dodecahedra (RD).[45,132,133] The elegant control over the morphology at nanoscale together with the formation of a smooth Pt-skin surface at atomic scale lead to exceptional ORR performance. The nanoframes were realized by removing the Ni-rich phase from the parent Pt−Ni RD through either ambient oxidation[45] or acetic acid treatment.[132,133] In the practice of ORR measurement, however, we noticed that the corrosion procedure had non-negligible influences on the catalytic performance. The ORR activity and durability of Pt−Ni nanoframes fluctuated in a wide range depending on how they were processed. In this regard, we here systematically compared three different corrosion procedures to provide a better understanding of how catalyst processing affects the composition and surface structure of Pt−Ni nanoframes and, thus, their catalytic activity and stability.

2.3 ORR Electrocatalytic Properties

To compare the effects of catalyst processing, we first synthesized Pt−Ni RD by the hot injection of metal precursors in oleylamine at 265 °C (for more details, see the Methods section at 2.6). The Pt−Ni RD were then subjected to different processing procedures,

as shown in Figure 2-1. In the first procedure, the as-synthesized Pt−Ni RD were directly loaded on carbon without removing the Ni-rich phase. We anticipated that excessive Ni in the solid RD would be eliminated by subsequent electrochemical corrosion. In the second and third procedures, the solid Pt−Ni RD were corroded before loading by a mild organic acid (acetic acid) and a strong oxidative acid (nitric acid), respectively. The acetic acid corrosion, a standard method to make nanoframes in our previous work,[132,133] was employed here as a benchmark. The nitric acid is certainly more aggressive than acetic acid, and a higher degree of chemical corrosion was therefore expected. After being loaded on carbon, the catalysts were annealed in air at 180 °C to remove the organic ligands. The air-annealed catalysts were stored in N_2 box with a dehumidification system at ambient temperature to exclude the influence of other environment factors.

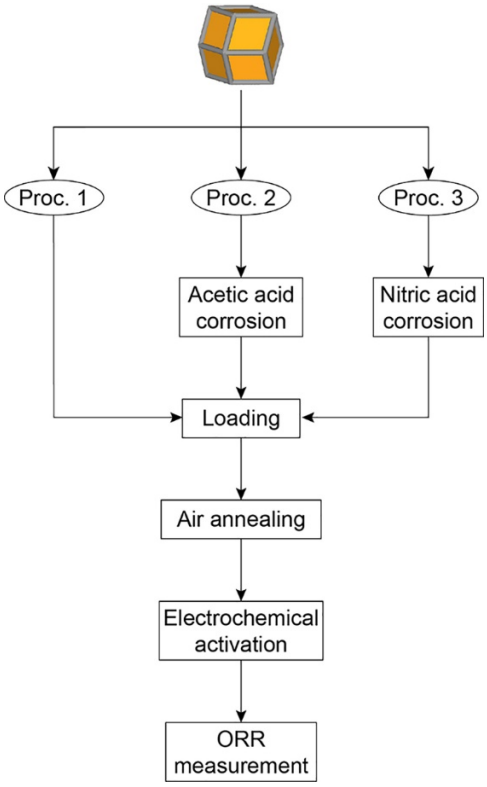

Figure 2-1 Catalyst processing procedures. Flow chart of three processing procedures applied to the as-synthesized Pt−Ni RD, termed as" Proc. 1", "Proc. 2", and "Proc. 3", respectively. In the geometrical model of RD, the gray color represents the Pt-rich phase, and the orange color represents the Ni-rich phase.

Before the evaluation of the electrocatalytic performance, the catalysts were pretreated or "activated" by potential cycling in Ar-saturated $HClO_4$ solution between 0.05 and 1.02 V_{RHE} with a sweep rate of 100 mV s^{-1} in a three-electrode RDE setup (Figure 2-1, electrochemical activation). This process was monitored by tracking the changes of the CV profiles until both the hydrogen and the hydroxyl adsorption−desorption regions

became stable. Figure 2-2 shows the CVs of the three samples at representative cycles. For the catalyst processed by procedure 1, the CVs kept enlarging significantly in the first 80 cycles (Figure 2-2a). This dramatic profile change can be explained by the massive Ni dissolution from the Ni-rich Pt−Ni RD driven by the potential cycling.[36] The expansion of the CV profiles is an indicator of the gradual exposure of Pt after the Ni dissolution. Electrochemical activation was also applied to the catalyst processed by procedure 2. The CVs exhibited a smaller expansion than that of procedure 1 and held steady after 50 cycles (Figure 2-2b). It suggests that there was still a small amount of unalloyed Ni species remained at outermost layers after acetic acid corrosion, which leached out during the electrochemical activation. For the catalyst processed by procedure 3, on the contrary, the CV variation was almost negligible from the very first cycle to the 35th cycle (Figure 2-2c). The barely changed CV profiles suggest that nitric acid corrosion was very effective to get rid of the excessive near-surface Ni and resulted in a fairly stable surface. The above explanations for the CV changes are mainly connected to the Ni dissolution, which were later validated by tracking the composition evolutions using energy-dispersive X-ray spectroscopy (EDX).

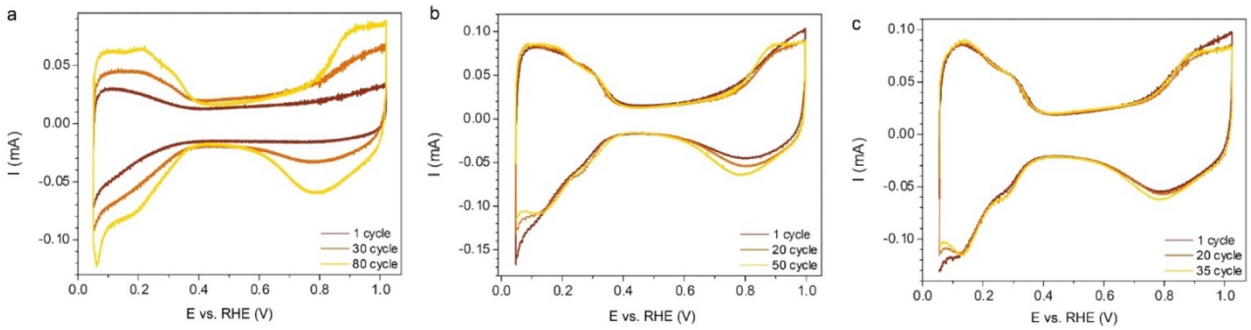

Figure 2-2 Electrochemical activation. CVs of the catalysts processed by procedures (a) 1, (b) 2, and (c) 3 at representative cycles during the electrochemical activation. The CVs become stable after 80 cycles for procedure 1, 50 cycles for procedure 2, and 35 cycles for procedure 3, respectively.

After the electrochemical activation, the ORR activity and stability of the three catalysts were evaluated (Figure 2-1, ORR measurement). Figures 2-3a−c shows the CV curves of each catalyst right after activation as well as after 1,000 and 30,000 cycles of accelerated durability testing (ADT). The ECSAs of each catalyst were calculated using the charges associated with H_{upd} normalized to the Pt mass loading. As shown in Figure 2-4a, the initial ECSAs for the three catalysts were 40.1 $m^2\ g_{Pt}^{-1}$ (procedure 1), 56.6 $m^2\ g_{Pt}^{-1}$ (procedure 2), and 54.8 $m^2\ g_{Pt}^{-1}$ (procedure 3), respectively. The catalysts obtained by acetic acid corrosion and nitric acid corrosion had similar surface areas that were consistent with the previously reported values for Pt−Ni nanoframes.[132,133] But, the electrochemical corrosion of Pt−Ni RD (procedure 1) resulted in a surprisingly low ECSA compared with the other two processes. Given that a substantial Ni dissolution

occurred during the electrochemical activation step, we attributed the low ECSA as a consequence of the surface reconstruction associated with the massive Ni loss. This interpretation was later supported by the catalyst morphology changes revealed by transmission electron microscopy (TEM). It should be mentioned that the ratios of CO_{ad} to H_{upd} for all the three catalysts are close to 1.0, where CO_{ad} represents the ECSA calculated from the CO-stripping.[134] The degradation trajectories of the ECSAs were also plotted in Figure 2-4a. In general, all the three catalysts underwent gradual decreases along with the potential cycles. The ECSAs after 30,000 ADT cycles were 34.5 $m^2\ g_{Pt}^{-1}$ (procedure 1), 41.2 $m^2\ g_{Pt}^{-1}$(procedure 2), and 47.2 $m^2\ g_{Pt}^{-1}$ (procedure 3), respectively. The catalyst treated by nitric acid corrosion had much less ECSA loss (14%) than that by acetic acid corrosion (27%), although their initial ECSAs were at the same level. Consistent with what has been learned from the earlier comparison of CV variations during the electrochemical activation, these results also suggest that a more-robust surface was delivered by nitric acid corrosion.

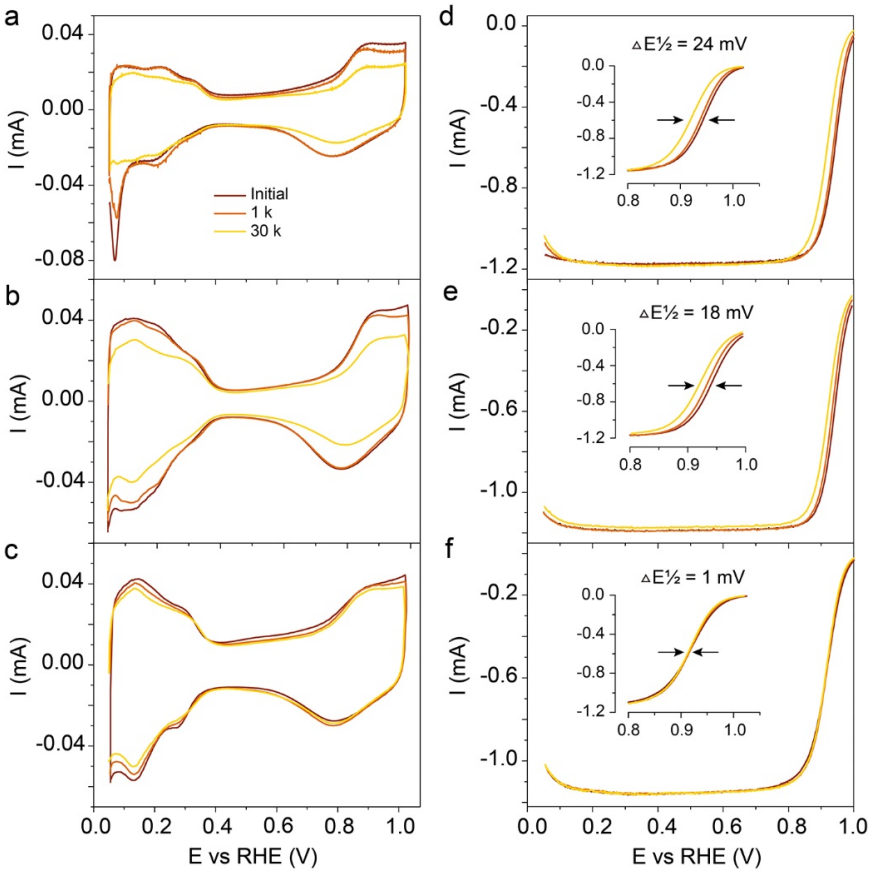

Figure 2-3 ORR electrocatalytic curves. (a−c) CVs and (d−f) ORR polarization curves of the catalysts processed by procedures (a, d) 1, (b, e) 2, and (c, f) 3. The initial measurement as well as after 1,000 and 30,000 ADT cycles were plotted for comparison. CV was measured in Ar-saturated 0.1 M $HClO_4$ electrolyte with a sweep rate of 50 mV s^{-1}. ORR activity was measured in O_2-saturated 0.1 M $HClO_4$ electrolyte with

a sweep rate of 20 mV s^{-1} and a rotation rate of 1,600 rpm. ADT was conducted in Ar-saturated 0.1 M $HClO_4$ electrolyte between 0.60 and 1.00 V_{RHE} with a sweep rate of 200 mV s^{-1}.

The ORR polarization curves of the three catalysts are compared in Figures 2-3d−f. The amplitudes of negative shift show direct visual evidence of the decreases in ORR activity following the order of procedure 1 > procedure 2 > procedure 3. The half-potential change after 30,000 cycles is 24 mV for procedure 1, 18 mV for procedure 2, and only 1 mV for procedure 3, respectively. The calculated kinetic currents at 0.95 V_{RHE} from the ORR polarization curves were normalized to the surface areas and Pt mass loadings to give the specific and mass activities, respectively. The results were listed in Figures 2-4b,c. Remarkably, the catalyst processed by electrochemical corrosion (procedure 1) exhibited an initial specific activity as high as 1.35 mA cm^{-2} (Figure 2-4b), almost an order of magnitude higher than that for commercial Pt/C (0.14 mA cm^{-2}). Considering that the specific activities of the hollow Pt−Ni nanoframes made in our lab were exclusively in the range of 0.5−1.0 mA cm^{-2}, the easily reproducible 1.35 mA cm^{-2} obtained by procedure 1 is quite unusual. The origins of this unusual specific activity and the aforementioned low ECSA were discussed later. For the catalyst treated by acetic acid (procedure 2), the initial specific activity was 0.97 mA cm^{-2} (Figure 2-4b), at a similar level to that in our previous report.[132] The initial specific activity for the catalyst corroded by nitric acid (procedure 3) was 0.44 mA cm^{-2} (Figure 2-4b), about one-third that of procedure 1. Despite the low initial activity, procedure 3 stands out when taking the durability into consideration. Only 7% specific activity loss was observed after 30,000 ADT cycles (Figure 2-4b). This long-term stability agrees with the above-discussed ECSA data and electrochemical activation CVs. In a sharp contrast, the highest specific activity obtained by procedure 1 suffered a steep decline and ended up with 58% loss (Figure 2-4b). This observation suggests that the highly reactive surface sites generated by electrochemical dealloying are vulnerable under long-term fuel cell operation. Different from both procedures 1 and 3, the degradation of the catalyst processed by procedure 2 featured a fast decrease before 3,000 cycles and thereafter reached a plateau (Figure 2-4b). Figure 2-4c charts the initial mass activities of the three catalysts and their deactivations. The initial mass activities for the catalysts of procedures 1 and 2 were both around 0.55 A mg_{Pt}^{-1}, while it was 0.24 A mg_{Pt}^{-1} for the catalyst of procedure 3. Notably, though the beginning-of-life mass activities were different, the end-of-life mass activities of the three catalysts all converged to 0.2 A mg_{Pt}^{-1}.

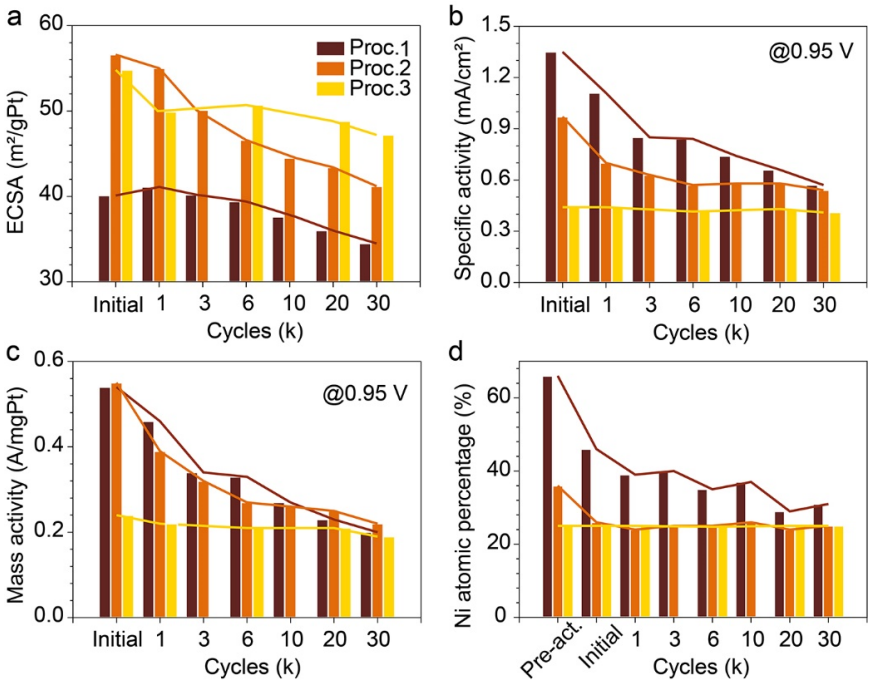

Figure 2-4 ORR electrocatalytic properties. (a) ECSA, (b) specific activity at 0.95 V_{RHE}, (c) mass activity at 0.95 V_{RHE}, and (d) Ni atomic percentage of the catalysts processed by procedures 1, 2, and 3 at representative stages. Here, "pre-act." represents the stage before the electrochemical activation, "initial" represents the initial ORR measurement after the activation, and numbers represent the stages after different ADT cycles, respectively.

2.4 Structural Characterizations

To elucidate the origins of the different catalytic behavior, catalysts after the ORR test were characterized in terms of composition, elemental distribution, morphology, and atom arrangement. Because the Ni composition in the near-surface region plays a key role in improving the ORR activity by weakening the binding of oxygenate species to Pt,[117,118,121,129] we first investigated the variations of Ni atomic percentage (quantified by EDX spectra) in Pt−Ni nanoframe catalysts through their entire lifetime, as shown in Figure 2-4d. For the catalyst processed by procedure 1, the Ni atomic percentage before the electrochemical activation was as high as 66%. Such a high Ni content is reasonable because no pre-leaching treatment was performed in procedure 1, and the composition of $Pt_{34}Ni_{66}$ agrees well with the solid Pt−Ni RD.[132] There was a rapid drop from 66% to 46% after the initial ORR test, suggesting a substantial Ni loss. This observation is consistent to the large expansion of CVs during the electrochemical activation step (Figure 2-1a). The decrease of the Ni composition slowed down after the initial ORR measurement. It gradually fell to 31% after 30,000 cycles of ADT. For the catalyst processed by procedure 2, the Ni composition was 36% before the electrochemical activation, decreased to 26% after the initial ORR measurement, and held steady

thereafter. The initial decrease of the Ni content is also reflected by the evolution of the CVs during the electrochemical activation (Figure 2-1b). It is worth noting that the dissolution of Ni stopped at a stable Pt_3Ni composition. Lastly, the catalyst treated by procedure 3 already reached a stable Pt_3Ni composition after nitric acid corrosion and stayed the same throughout the whole lifetime, which was, again, in good agreement with the results shown in Figure 2-1c.

Several implications can be drawn from the above composition study. First, the high initial Ni atomic percentage is very likely to be a major contributor to the unusual high specific activity for the catalyst processed by procedure 1. Second, the Ni depletion seems to be unstoppable before reaching the stable Pt_3Ni composition. Third, pre-leaching can provide additional handles with which to balance the initial ORR activity and long-term stability by changing the starting Ni content in the catalysts. Although the mass activities after 30,000 cycles were very close for all the three procedures, we think that procedure 3 is a more-appropriate practice for the future catalyst processing because it provides more-stable performance in the long run. Meanwhile, the minimum electrochemical dissolution of Ni in procedure 3 (Figure 2-4d) will not impair the performance of the ionomer and membrane in PEMFCs.[29]

However, comparing the composition evolutions of procedures 2 and 3 (Figure 2-4d), we noticed that the specific activities of procedure 2 were always higher than those of procedure 3 despite the same Ni atomic percentage. This independence implies that the near-surface compositions were different in these two cases. Further characterizing the spatial distribution of Ni within a single particle is therefore needed. Figure 2-5 shows the high-angle annular dark-field scanning transmission electron microscopy (HAADF-STEM) and the STEM−EDX mapping images of the catalysts at representative ADT cycles. The elemental maps of the catalysts after the initial ORR measurement clearly showed the surface enrichment of Ni in a descending order of procedure 1 ≫ procedure 2 > procedure 3. The more the Ni enriches in the near-surface region, the higher the ORR activity is. A thin Ni layer was still visible even after 1,000 cycles for procedure 1 (Figure 2-5a); it is no wonder that the high specific activity retained (up to 1.1 mA cm^{-2}). Although it is hard to tell the difference between procedures 2 and 3 after 1,000 cycles, more Ni surface enrichment can be confirmed for procedure 2 after 30,000 cycles. Furthermore, the particle morphologies are outlined by the HAADF-STEM images. Interestingly, while the catalysts treated by procedures 2 and 3 presented the typical hollow structures after the initial ORR test, the one by procedure 1 appeared to be more solid and more ill-defined (Figure 2-5a). Moreover, for procedure 2, the well-defined nanoframe was destroyed along with the stability test and became difficult to recognize

after 30,000 cycles (Figure 2-5b), whereas the morphology was preserved all along for procedure 3 (Figure 2-5c).

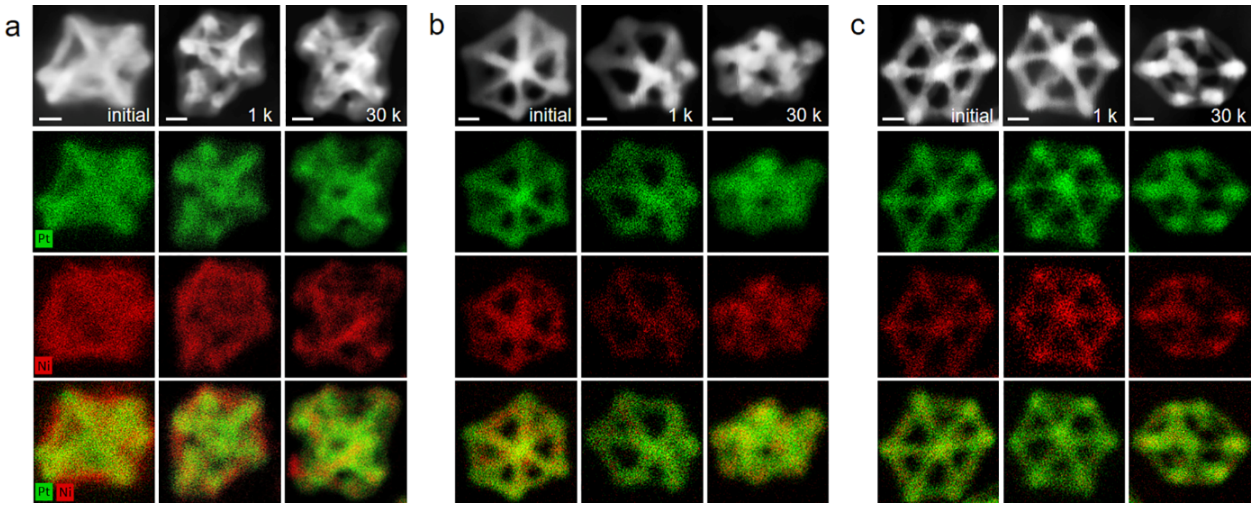

Figure 2-5 Elemental distributions. HAADF-STEM and EDX mapping images of the catalysts processed by procedures (a) 1, (b) 2, and (c) 3 after the initial ORR measurement as well as after 1,000 and 30,000 ADT cycles. In the EDX maps, green color represents Pt and red color represents Ni, respectively. Scale bar is 5 nm in all images.

The morphology evolutions of the catalysts were further investigated by TEM at low magnifications to picture the ensembles of the particles (Figure 2-6). Certainly, the low-magnification TEM images provide very strong support to the above conclusions. The electrochemical corrosion of the solid RD (Figure 2-6a) led to partly corroded particles (Figure 2-6b) rather than nanoframes. The semihollow morphology has an intrinsically small surface-area-to-volume ratio, rationalizing the observed low ECSA. These particles had hexagonal projections on the carbon support after the initial ORR measurement (Figure 2-6b). The contours of the particles became rough after 1,000 cycles (Figure 2-6c) and evolved to irregular shape after 30,000 cycles (Figure 2-6d). This morphology evolution is closely associated with the dissolution of Ni during the electrochemical measurement. As mentioned earlier, a 20% Ni loss occurred (from 66% to 46%) after the initial ORR measurement. Such a large amount of Ni dissolution could generate lots of surface vacancies and even porosities, leaving a so-called Pt-skeleton surface.[125,127,135] Given that defects can enhance the mobility and dissolution of Pt,[49,119,136] a succession of surface reconstruction is expected, eventually leading to the morphology change and ECSA loss. Under the same framework, the deconstruction of the nanoframe observed in procedure 2 (Figures 2-6e−h) could be governed by a similar dissolution–diffusion −reconstruction process. Figures 2-6i−l describes the morphology evolution of the catalyst pre-corroded by nitric acid (procedure 3). In addition to the well-maintained nanoframe configuration, the sharp corners of the frame gradually turned rounded,

especially after 30,000 cycles of ADT. This observation supports the notion that the under-coordinated surface atoms are more susceptible to surface diffusion and/or electrochemical dissolution.[48,137] These results collectively substantiated that the stable Pt_3Ni composition achieved by a pre-corrosion using nitric acid could prevent the undesired electrochemical Ni dissolution that triggered a series of adverse effects in the other two procedures.

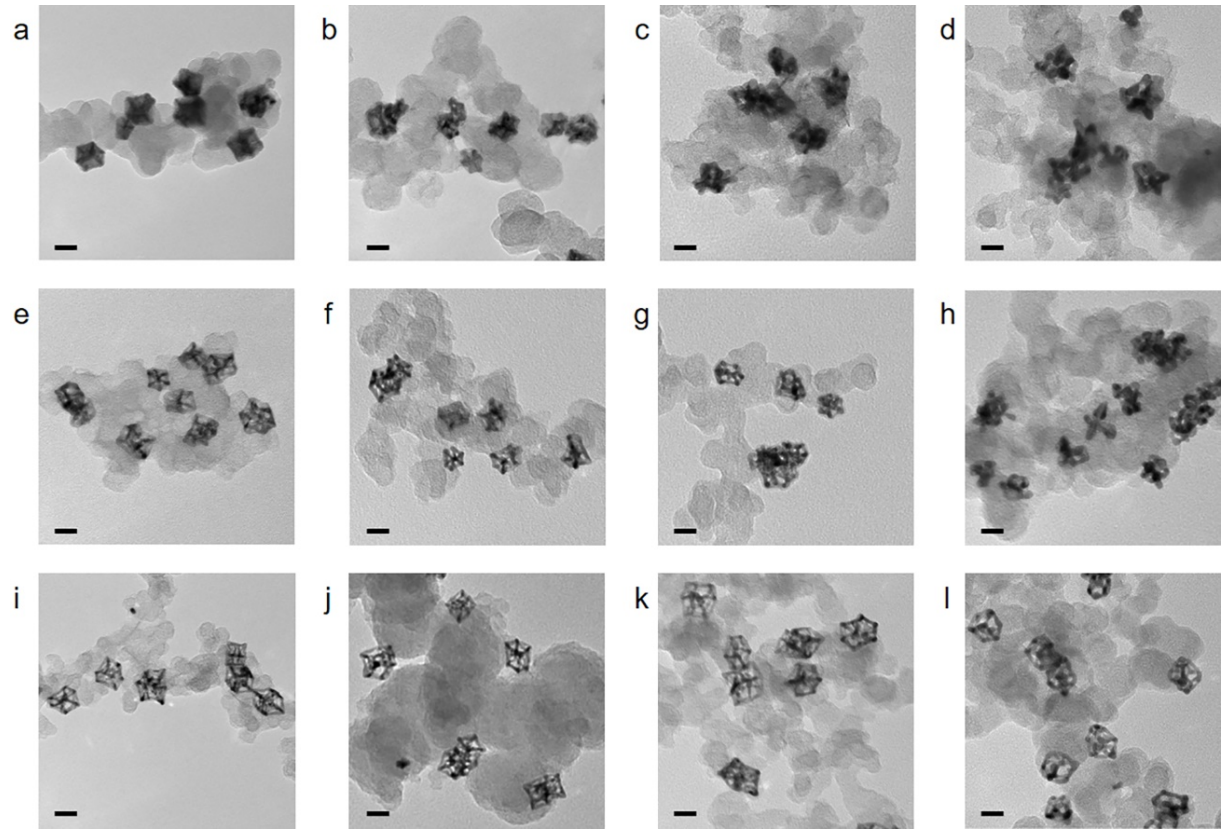

Figure 2-6 Morphologies. Low-magnification TEM images of the catalysts processed by procedures (a−d) 1, (e−h) 2, and (i−l) 3 (a, e, i) before the electrochemical activation, (b, f, j) after the initial ORR test, and after (c, g, k) 1,000 and (d, h, l) 30,000 ADT cycles. Scale bar is 20 nm in all images.

In an attempt to verify the existence of surface defects generated by the electrochemical Ni dissolution, the atom arrangements of the catalysts were studied by high-resolution TEM (HRTEM). Figure 2-7 shows the HRTEM images and the fast Fourier transforms (FFTs) of the catalysts after the initial ORR measurement. All three particles were highly crystalline featuring the face-centered cubic (fcc) structures. An obvious morphological difference was confirmed by comparing the particles of procedure 1 (Figure 2-7a) and procedure 3 (Figure 2-7c), both oriented to the <110> zone axis. Unfortunately, when focusing on the surface of each particle, we could hardly resolve the atom arrangement in accuracy due to the presence of ghost atoms.

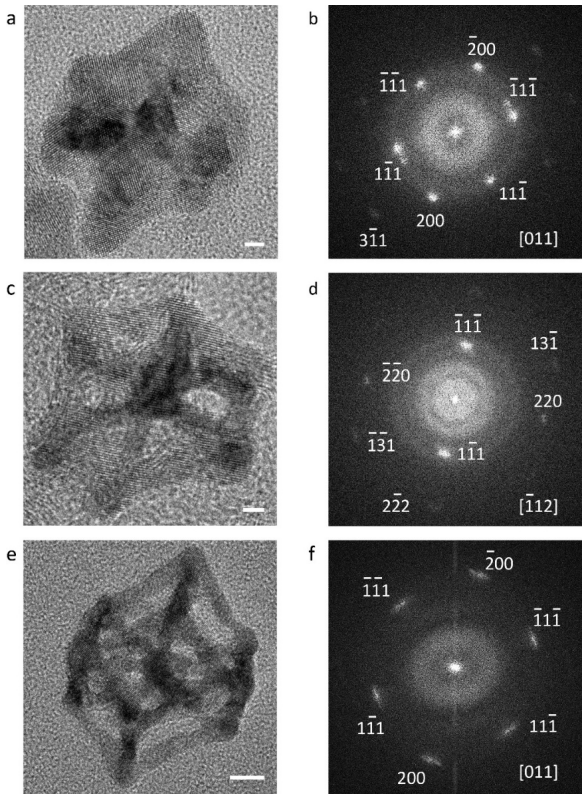

Figure 2-7 Lattices and atom arrangements. (a, c, e) HRTEM images and (b, d, f) corresponding FFTs of the catalysts processed by procedures (a, b) 1, (c, d) 2, and (e, f) 3 after the initial ORR measurement. Scale bar is 2 nm in (a, c) and 5 nm in (e).

We then turned our attention to the potential effects of the mild air annealing because thermal treatments were believed to be able to modify particle structures.[103,104,123,125-128] Overnight air annealing at 180 °C was applied to all the three catalysts for the purpose of surface cleaning (Figure 2-1). Powder X-ray diffraction (XRD) was performed to study the catalyst structural changes during this process. As shown in Figure 2-8a, the as-synthesized Pt−Ni RD exhibited asymmetric peaks, resulting from the coexistence of the Pt-rich and Ni-rich phases in the solid particles.[132] Catalyst loading did not alter the XRD patterns in terms of shape, position, and width (Figure 2-8b). After the air annealing, however, all the reflections shifted toward smaller Bragg angles and the peak profiles became more symmetric in procedure 1 (Figure 2-8c). These changes indicate an increased alloying extent through thermally driven atomic diffusion at the Pt-rich−Ni-rich interface. The increased alloying extent is in good agreement with the high Ni content remained after the electrochemical activation in procedure 1. Meanwhile, the full width at half-maximum (FWHM) of the XRD profiles had no obvious change, suggesting the grain sizes were well maintained during this low-temperature treatment. The evolutions of the XRD patterns of the catalysts processed by procedure 2 (Figures 2-8d−f) and procedure 3 (Figures 2-8g−i) were also followed. Different from what was

observed for procedure 1, the XRD profiles of the two catalysts before air annealing were in perfect Gaussian shapes, corresponding to the single-alloy phase. Not surprisingly, there was little change in the XRD patterns after air annealing. Because most Ni had been chemically corroded in advance, atomic interdiffusion lost necessary conditions. Moreover, the (111) reflections of the annealed catalysts (Figures 2-8c,f,i) possessed a progressive shift toward lower two theta values, reflecting the decreased Ni content in the order of procedure 1 > procedure 2 > procedure 3. While the XRD provides structural information on Ni in the bulk, our previous X-ray absorption spectroscopy (XAS) study has shown that surface Ni can be oxidized during air annealing and then removed during electrochemical measurement.[134]

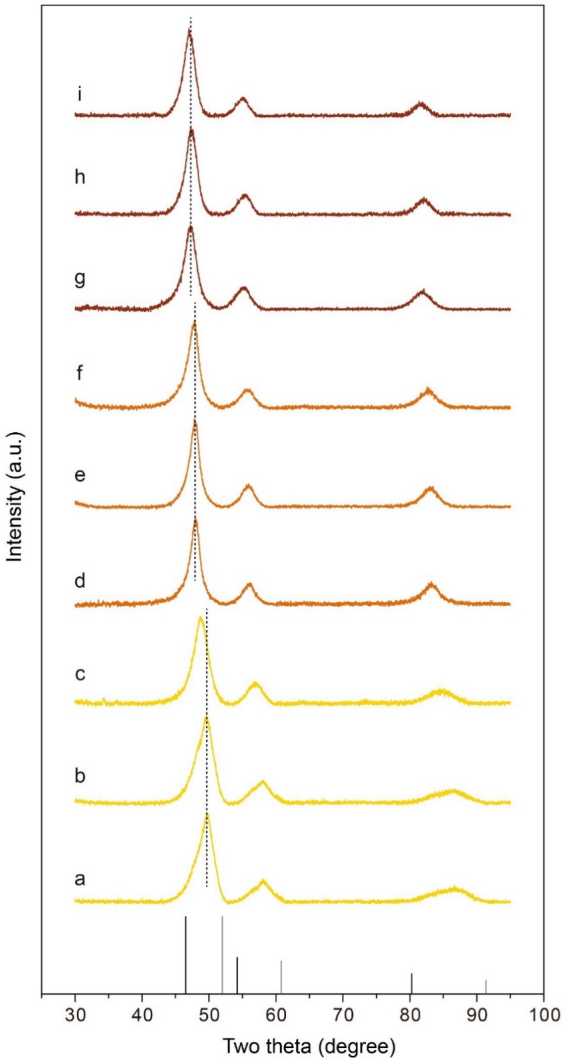

Figure 2-8 Crystal structures. XRD patterns of the catalysts processed by procedures (a−c) 1, (d−f) 2, and (g−i) 3 (a, d, g) before and (b, e, h) after being loaded on carbon, as well as (c, f, i) after air annealing. Black line, Pt, JCPDS#65-2868; grey line, Ni, JCPDS#65-2865.

With the thorough investigation of the degradation trajectories and the characterizations of the catalysts at representative stages, our hypothesis could be depicted as Figure 2-9. Among all the post-synthesis treatment procedures, we believe the acid corrosion and air annealing are the two key steps that regulate the delicate balance between the ORR activity and durability of Pt−Ni nanoframe catalysts. The acid corrosion was utilized to remove the Ni-rich phase in the solid Pt−Ni RD and, thus, to alter the Ni atomic percentage in the final Pt−Ni nanoframes (procedures 2 and 3). The air annealing was employed to remove the organic ligands (procedures 1−3), yet was also able to enhance the alloying extent via atomic interdiffusion (procedure 1). The combination of the two factors not only defines the starting Ni composition (and, thus, the initial activity) but also decides the magnitude of Ni dissolution during the electrochemical measurement (and, thus, the durability). We believe the magnitude of Ni dissolution is related to the formation of low-coordinated surface sites, which is a major trigger for the destruction of the surface structure and the particle morphology (and, hence, the decrease of ECSA, specific activity, and mass activity). Finding ways to annihilate the electrochemical Ni dissolution holds the key to less-defective surfaces and will be the focus of our future work.

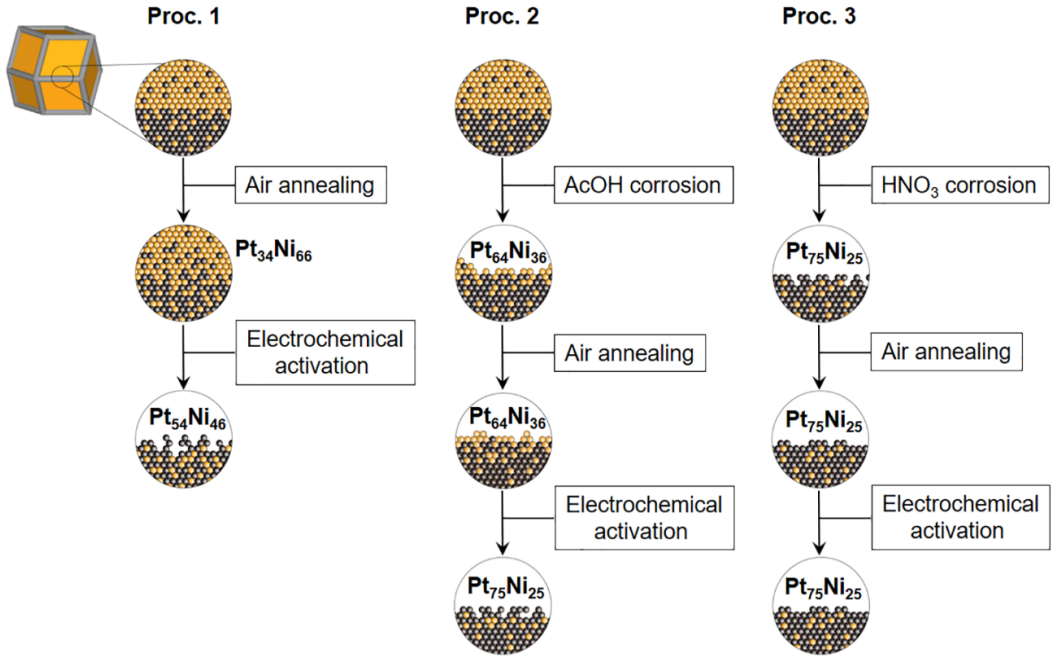

Figure 2-9 Proposed atomic structures. Schematic diagram of the atomic structures of the catalysts at representative stages in procedures 1, 2, and 3, respectively. The Pt-rich−Ni-rich interface in the solid RD was highlighted by a circle and depicted in detail. The orange color represents Ni, and the gray color represents Pt, respectively. The acid corrosion and air annealing are two key factors determining the remaining Ni content and surface roughness after the electrochemical activation.

2.5 Conclusions

In conclusion, we have developed three different catalyst processing procedures to understand the effects of post-synthesis treatment on the ORR performance of Pt−Ni nanoframe electrocatalysts. We systematically varied the chemical corrosion extents of the Pt−Ni RD before loading (namely, non-corrosion, mild corrosion, and strong corrosion). The initial ORR activities as well as the degradation trajectories of ECSA, specific activity, and mass activity were compared. The results indicate a compromise between the activity and stability of Pt−Ni nanoframes. By characterizing the evolutions of the bulk composition, elemental distribution, and morphology using TEM, HAADF-STEM, EDX, HRTEM, and XRD, we have correlated the resulting ORR activity and stability to the Ni content in the catalysts. While the initial Ni contents are the major contributors to the different ORR activities, the electrochemical Ni dissolution triggers a cascade of structural changes that account for the catalyst deactivation. These results could serve as a guideline on how to accomplish desired properties by catalyst processing for a variety of bimetallic electrocatalysts.

2.6 Methods

Synthesis of Pt−Ni RD. In a typical synthesis, 20 mg of $H_2PtCl_6{\cdot}6H_2O$ and 14.5 mg of $Ni(NO_3)_2{\cdot}6H_2O$ were dissolved in 0.7 mL of oleylamine in a small centrifuge tube. The precursor solution was injected into a three-necked flask charged with oleylamine (9 mL) that had been preheated at 160 °C for 1 h under N_2 purging. After the injection, the reaction was kept under vacuum for 2.5 min. Next, the reaction was heated to 265 °C with a ramping rate of 15 °C min^{-1} under N_2. The color of the solution changed from green to yellow, brown, and, finally, black after the temperature reached 265 °C. The reaction was stopped at 4 min after the solution turned black by carefully transferring the flask into a water bath to quench the growth. The products were washed twice with a hexane/ethanol mixture and collected by centrifugation at 12,000 rpm.

Acetic acid corrosion. The Pt−Ni RD collected by centrifugation were redispersed in 2 mL of toluene by brief sonication and then mixed with 5 mL of acetic acid. The mixture was heated at 90 °C under vigorous stirring for 2 h in air to allow the evolution from Pt−Ni RD to Pt−Ni nanoframes. The products were washed twice with a hexane/ethanol mixture and collected by centrifugation at 12,000 rpm.

Nitric acid corrosion. The Pt−Ni RD collected by centrifugation were redispersed in 10 mL of nitric acid (2M) aqueous solution by intense sonication. The mixture was heated at 70 °C under vigorous stirring for 12 h in air to corrode the Pt−Ni RD into Pt_3Ni

nanoframes. The products were first washed once with pure ethanol and then washed twice with a hexane/ethanol mixture. After each wash, the sample was collected by centrifugation at 12,000 rpm.

Electrochemical measurements. The as-synthesized or acid-corroded Pt−Ni RD were redispersed in chloroform and added to carbon in a ratio that produced a loading of 18−20 wt% Pt. The mixture was shaken or sonicated in chloroform for 3 to 5 min to complete the loading process. The loaded catalyst was washed twice with hexane and collected by centrifugation at 10,000 rpm. The resulting black powder was heated at 180 °C in air for 14 h to remove the organic ligands. The carbon supported catalyst was then dispersed in ultrapure water with a concentration of 0.5 $mg_{catalyst}$ mL^{-1}. The actual concentration of Pt in the ink was determined by inductively coupled plasma-optical emission spectroscopy (ICP-OES). The catalyst ink was deposited onto a glassy carbon RDE (Pine Instruments, 0.196 cm^2) in the appropriate volume to achieve about 10 μg_{Pt} cm^{-2} loading density. The commercial Pt/C catalyst had a loading density of 7.8 μg_{Pt} cm^{-2}. The electrochemical measurements were conducted in a three-compartment glass electrochemical cell with a Pine RDE setup and a Biologic VSP potentiostat. A saturated Ag/AgCl electrode and a Pt wire were used as reference and counter electrodes, respectively, and 0.1 M $HClO_4$ prepared from 67% $HClO_4$ was used as the electrolyte. All potentials are presented versus the RHE. The catalyst was typically held at 0.05 V_{RHE} between measurements, and the limits of CV were 0.05−1.02 V_{RHE}. H_{upd} measurements were performed by saturating the electrolyte with Ar gas before collecting the CV with a sweep rate of 50 mV s^{-1}. The ORR activity measurements were carried out under O_2-purging conditions and with a sweep rate of 20 mV s^{-1} with an RDE rotation rate of 1,600 rpm. The ADT was conducted by potential cycling in Ar-saturated 0.1 M $HClO_4$ electrolyte between 0.60 and 1.00 V_{RHE} with a sweep rate of 200 mV s^{-1} for different numbers of cycles. The currents for ORR were corrected for an ohmic potential drop (iR drop). All of the electrochemical measurements were conducted at room temperature.

Chapter. 3 High-Performance Pt−Co Nanoframes Advance Fuel-Cell Electrocatalysis

The contents and figures of this chapter are adapted or reprinted with permission from S. Chen,† M. Li,† M. Gao, J. Jin, M. A. van Spronsen, M. B. Salmeron, and P. Yang,* "High-Performance Pt–Co Nanoframes for Fuel-Cell Electrocatalysis", *Nano Letters* **2020**, *20*, 1974–1979. DOI: 10.1021/acs.nanolett.9b05251. Copyright 2020 American Chemical Society.[138]

3.1 Preface

Controlled synthesis of nanoparticles with rationally designed shape and component is the most straightforward way to tune their catalytic properties. In Chapter 3, we report the development of Pt–Co nanoframes, which combine the active Pt–Co composition and the hollow nanoframe morphology, to advance fuel-cell electrocatalysis. The as-prepared Pt–Co nanoframes exhibit superior activity and durability for both ORR and methanol oxidation reaction (MOR) in either acidic or alkaline environment.

3.2 Introduction

Fuel-cell technology represents a promising solution for sustainable energy supplies in the future, especially in the field of electrical automobiles and portable electronic devices.[21,139] In a typical fuel cell, the fuel (H_2, alcohol) is oxidized at the anode and the oxidant (O_2) is reduced at the cathode, both of which must be efficiently catalyzed for maximal overall power output.[100,140,141] Depending on the type and application of fuel cells, the electrolyte could be either acid or alkali to deliver the best behavior.[142,143] Hence, the development of high-performance electrocatalysts for both anodic and cathodic reactions within acidic/alkaline environments is critical for fuel-cell adoption. To date, because of the most appropriate binding energies of reaction intermediates, Pt has been universally recognized as the most active element for catalyzing various reactions in fuel cells, such as ORR and MOR.[28,144] However, its scarcity and high cost still remain as severe challenges in practical applications.[145]

In order to enhance the catalytic performance while reducing the usage of Pt, both the morphology and the composition of Pt-based nanomaterials must be rationally designed. With regard to the structural design, the catalyst should have an ideal morphology that exposes the most active sites (Pt) on the surface to contact the reactants.[102,146] Until now, considerable efforts have been made to synthesize Pt-based nanocatalysts with various

geometries, including 0D spherical or octahedral nanoparticles, 1D nanowires, and 2D nanoplates.[42,102,146-148] Among all of the different architectures, the highly open nanoframe configuration is of particular interest, because of its 3D surface molecular accessibility.[45] The Pt−Ni nanoframes have been reported to exhibit large surface area in the electrochemical measurement, which leads to remarkable ORR activity.[45,116,132,133] Composition-wise, the catalyst should also possess a favorable component that optimizes the binding energies of reaction intermediates. Alloying Pt with proper transition metals has been demonstrated as a significant way to improve catalytic properties.[99,149] Theoretical simulations have predicted that the Pt−Co component would exhibit the highest ORR activity, which has been later confirmed by various experimental studies.[25,30,105,150] Beyond ORR, the Pt−Co alloys have also been proved to greatly advance MOR electrocatalysis.[151] Here, we combine the hollow framework with the Pt−Co composition to develop Pt−Co nanoframes (NF), which are evolved from Pt−Co RD by etching away the Co-rich phase. The obtained Pt−Co NF exhibit excellent activity and stability for ORR and MOR in acidic/alkaline electrolyte.

3.3 Synthesis and Characterizations

We first synthesized Pt−Co RD by hot injection of Pt and Co precursors in a mixture of oleylamine and oleic acid at 240 °C (for more details, see the Methods section at 3.8). The reaction temperature, ratio of Pt to Co precursors, and proportion of oleylamine to oleic acid, were optimized to achieve good morphology and uniformity (Figure 3-1).

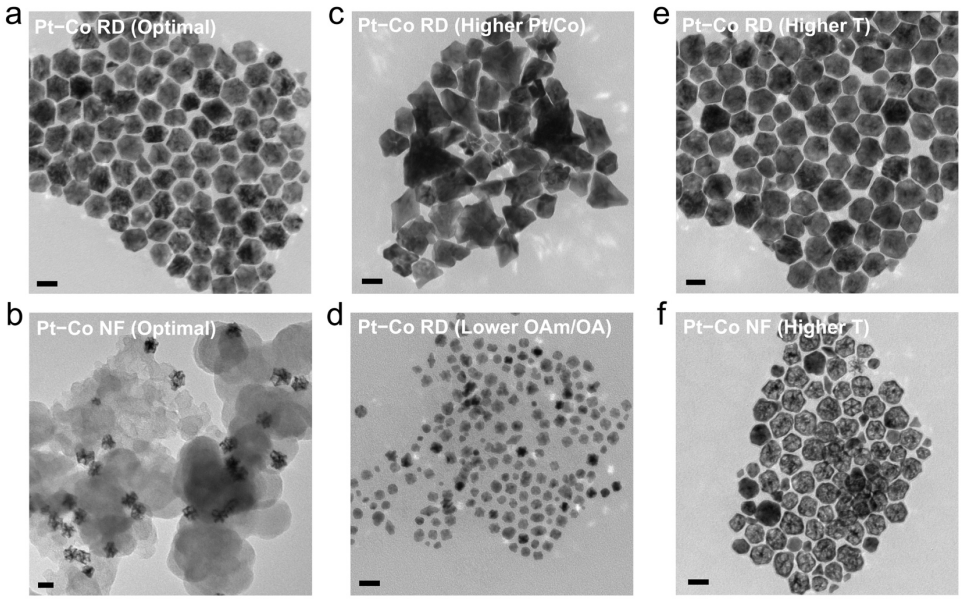

Figure 3-1 Synthetic optimization of Pt−Co RD. TEM images of (a) Pt−Co RD synthesized with the optimal reaction conditions (T = 240 °C, $m_{Pt\ precursor}/m_{Co\ precursor}$ = 400/842, $V_{oleylamine}/V_{oleic\ acid}$ = 8/2), (b)

Pt−Co NF evolved from (a) via nitric acid corrosion, (c−e) Pt−Co RD prepared with the same conditions as those of (a) except (c) $m_{Pt\ precursor}/m_{Co\ precursor}$ = 400/350, (d) $V_{oleylamine}/V_{oleic\ acid}$ = 6/4, and (e) T = 265 °C, and (f) Pt−Co NF obtained by nitric acid corrosion of (e). Scale bar is 20 nm in all images.

The TEM image (Figure 3-2b) outlines the as-prepared solid RD particles at ~23 nm with characteristic hexagonal projections. The EDX maps (Figure 3-2c) describe the elemental distribution of RD, in which Pt is mainly concentrated on the edges of the polyhedron while Co is uniformly distributed inside the particle. Such heterogeneous configuration was also confirmed by the HAADF-STEM image (Figure 3-2c), which shows a brighter contrast on the edges and suggests a local enrichment of heavier Pt atoms. These results indicate the phase segregation of Pt and Co in Pt−Co RD, which is analogous to the previously reported coexistence of Pt-rich and Ni-rich phases in Pt−Ni RD.[45,132] The composition of pristine RD measured by EDX is $Pt_{23}Co_{77}$, which is consistent with the ICP-OES result (Table 3-1).

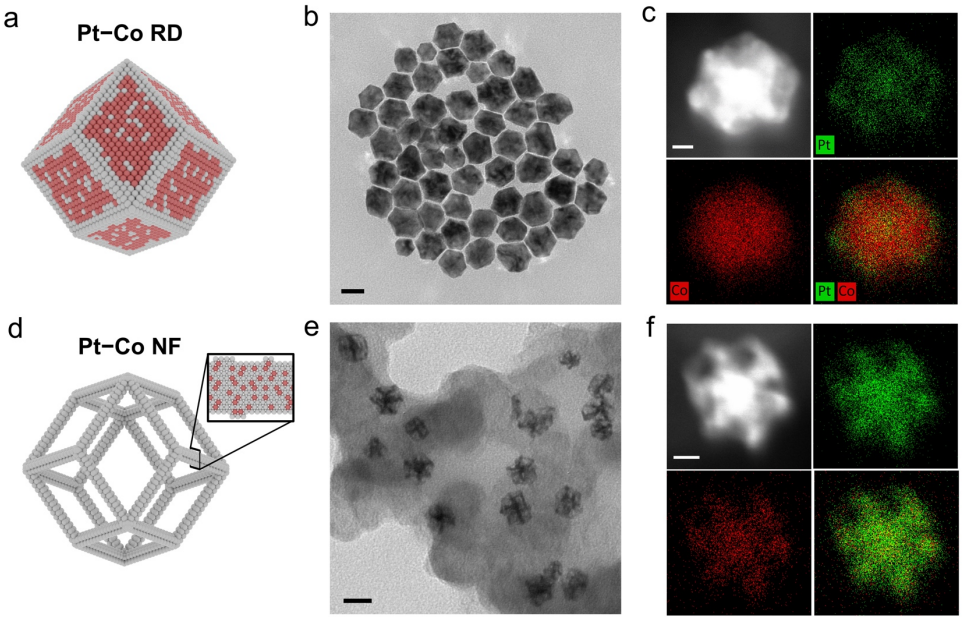

Figure 3-2 Structures of Pt−Co RD and NF. (a, d) Model schematics, (b, e) TEM images, and (c, f) HAADF-STEM images and EDX maps of Pt−Co (a−c) RD and (d−f) NF. In the models, gray spheres represent Pt atoms and red spheres represent Co atoms. In the EDX maps, green color represents Pt and red color represents Co. Scale bar is 20 nm in TEM images and 5 nm in HAADF-STEM images.

The Pt−Co RD were then loaded on carbon black support and corroded by nitric acid,[116] during which they evolved into Pt−Co NF. The as-treated particles featured the open framework and hollow interior, implying the successful preparation of 3D NF (Figure 3-2e). The HAADF-STEM image and EDX maps (Figure 3-2f) demonstrate that Pt and Co are homogeneously distributed along the NF without extra Co inside. Both ICP and EDX determined the composition of NF to be $Pt_{82}Co_{18}$ (Table 3-1), suggesting significant Co

dissolution. Hence, we can conclude that, during the evolution from Pt−Co RD to NF, the Co-rich phase in the interior was etched away by nitric acid and the Pt-rich phase on the edges was maintained to construct the hollow frame.

Table 3-1 Compositions of Pt−Co RD and NF. Compositions of as-prepared Pt−Co RD and NF, as well as Pt−Co NF after different electrocatalysis, measured by ICP and EDX.

	ICP	EDX
Pt−Co RD	$Pt_{21}Co_{79}$	$Pt_{23}Co_{77}$
Pt−Co NF	$Pt_{83}Co_{17}$	$Pt_{82}Co_{18}$
Acidic initial ORR	N/A	$Pt_{82}Co_{18}$
Acidic 10 k ORR	N/A	$Pt_{85}Co_{15}$
Alkaline initial ORR	N/A	$Pt_{83}Co_{17}$
Alkaline 6 k ORR	N/A	$Pt_{86}Co_{14}$
Alkaline initial MOR	N/A	$Pt_{83}Co_{17}$

The distinctive phase segregation of Pt and Co was further confirmed by XRD. Both Pt−Co RD and NF exhibited typical fcc structures (Figure 3-3). The peak separation in the (111) reflection of Pt−Co RD suggests two sets of diffraction patterns, which are assigned to a Pt-rich phase and a Co-rich phase. After nitric acid corrosion, only one symmetric (111) reflection peak was observed, corresponding to a single Pt-rich phase in Pt−Co NF.

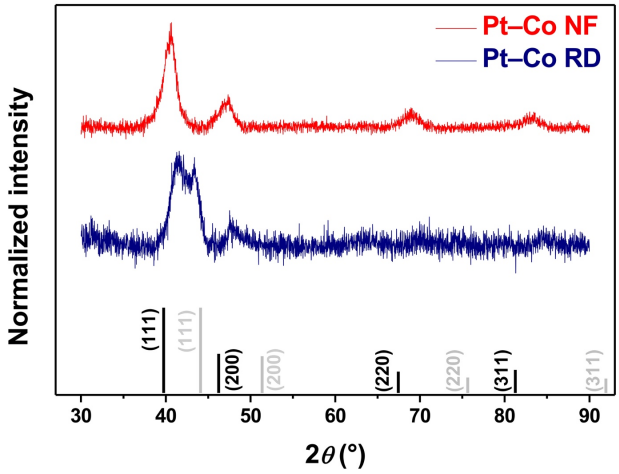

Figure 3-3 XRD patterns of Pt−Co RD and NF. Black line, Pt, PDF#03-065-2868; grey line, Co, PDF#01-071-4651.

The HRTEM images and FFTs (Figures 3-4a,b) also verified the morphology, crystal structure, and lattice spacing of Pt−Co RD and NF, which are consistent with the above results.

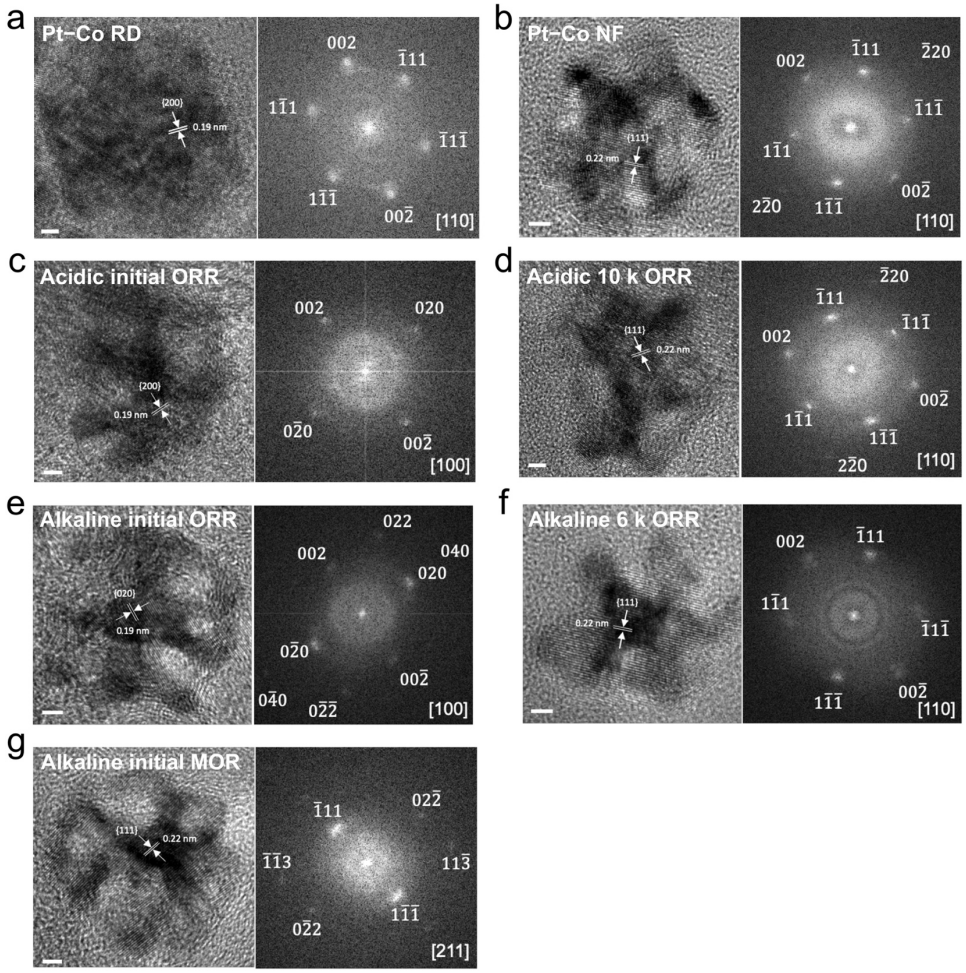

Figure 3-4 HRTEM images and FFTs of Pt−Co RD and NF. HRTEM images and FFTs of (a) as-synthesized Pt−Co RD, (b−g) Pt−Co NF after (b) nitric acid corrosion, (c) initial and (d) 10,000 cycles of acidic ORR, (e) initial and (f) 6,000 cycles of alkaline ORR, and (g) initial alkaline MOR. Scale bar is 2 nm in all images.

3.4 ORR Electrocatalytic Properties

Prior to evaluating the electrocatalytic properties, the Pt−Co NF were fully activated by CV in Ar-saturated $HClO_4$ solution between 0.05 V_{RHE} and 1.02 V_{RHE} with a sweep rate of 100 mV s^{-1}. After pretreatment, we first examined their ORR activity and stability in acidic electrolyte, which was 0.1 M $HClO_4$. Figure 3-5a shows the CV curves of Pt−Co NF for the initial ORR measurement, as well as after 10,000 cycles of ADT. The ECSA of the catalyst was calculated using the charges associated with H_{upd} normalized to the total mass of loaded Pt. The initial ECSA of Pt−Co NF was determined to be 50.0 m^2 g_{Pt}^{-1}, which was at a similar level to the previously reported values for Pt−Ni NF and supported the construction of hollow framework.[45,116,132,133] The CV curve only shrank slightly after 10,000 ADT cycles, resulting in an ECSA of 45.8 m^2 g_{Pt}^{-1}. Such a small

change in ECSA (8% loss) serves as the first proof that the obtained Pt−Co NF are highly stable in acidic ORR measurement. The excellent durability is attributed to the robust surface delivered by nitric acid corrosion and the negligible Co dissolution during the stability test (Table 3-1), as evidenced by our previous studies on Pt−Ni NF.[116] The ORR polarization curves of Pt−Co NF and commercial Pt/C catalyst are plotted in Figure 3-5b. The difference in half-potentials for initial measurements is as large as 26 mV, indicating a better ORR kinetics for Pt−Co NF. The improved kinetics was also confirmed by the smaller Tafel slope of Pt−Co NF, compared with that of commercial Pt/C (Figure 3-6). Remarkably, the initial specific and mass activities of Pt−Co NF calculated at 0.95 V_{RHE} using the K−L equation were 0.80 mA cm^{-2} and 0.40 A mg_{Pt}^{-1}, respectively, which were 6 and 4 times higher than those of commercial Pt/C (Figure 3-5c). It is worth mentioning that these initial activities also almost doubled those of Pt−Ni NF processed by nitric acid (Figure 3-5c).[116] These findings are in good accordance with the theoretical prediction that the composition of Pt−Co provides better ORR activity, because of the further downshift of the *d*-band center and the weakened binding energies of oxygenated species.[30] The ORR polarization curve of Pt−Co NF showed negligible shift after 10,000 ADT cycles (Figure 3-5b), further substantiating the long-term stability. The end-of-life specific and mass activities of Pt−Co NF were 0.75 mA cm^{-2} and 0.34 A mg_{Pt}^{-1}, both of which were even higher than the beginning-of-life activities of commercial Pt/C and Pt−Ni NF (Figure 3-5c).

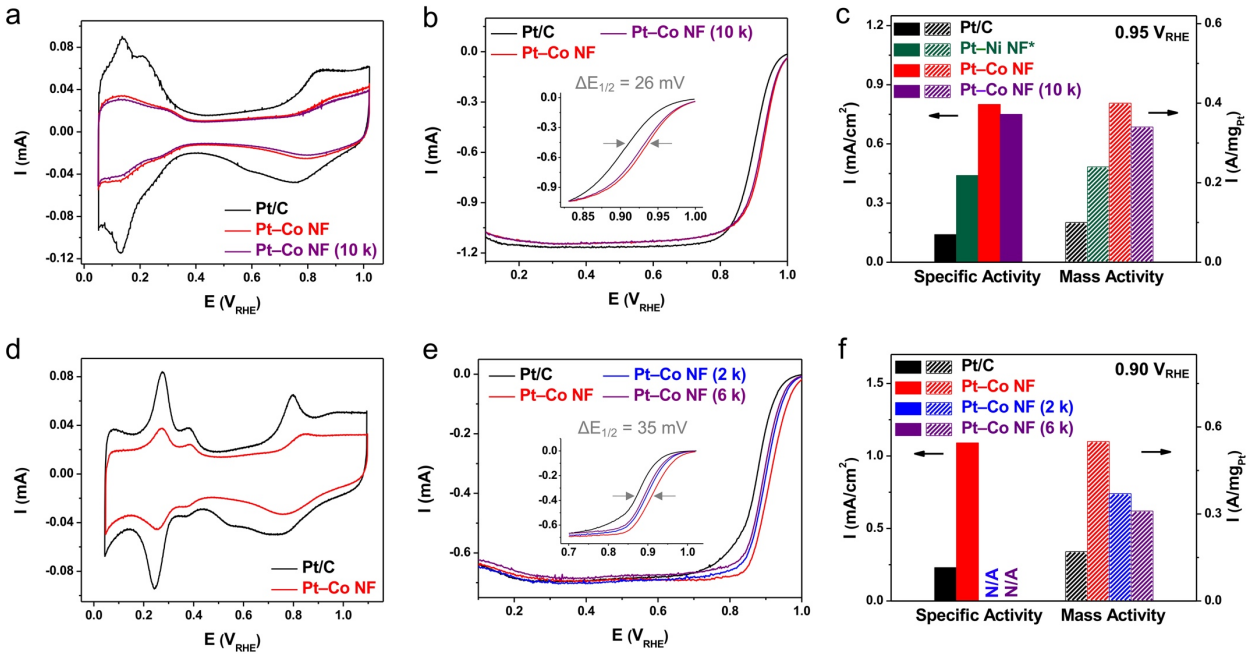

Figure 3-5 ORR performances of Pt−Co NF. (a, d) CV curves, (b, e) ORR polarization curves, and (c, f) specific and mass activities of Pt−Co NF and commercial Pt/C in (a−c) 0.1 M $HClO_4$ and (d−f) 1 M KOH electrolytes. CV was performed in Ar-saturated electrolyte with a sweep rate of 50 mV s^{-1}. ORR

polarization curves were recorded in O_2-saturated electrolyte with a sweep rate of 20 mV s^{-1}. ADT was conducted by potential cycling in Ar-saturated electrolyte with a sweep rate of 200 mV s^{-1}. Activities were calculated at 0.95 V_{RHE} in 0.1 M $HClO_4$ and 0.90 V_{RHE} in 1 M KOH. The asterisk symbol (*) in (c) indicates that the Pt−Ni NF were reported in ref 116 and obtained via nitric acid corrosion.[116]

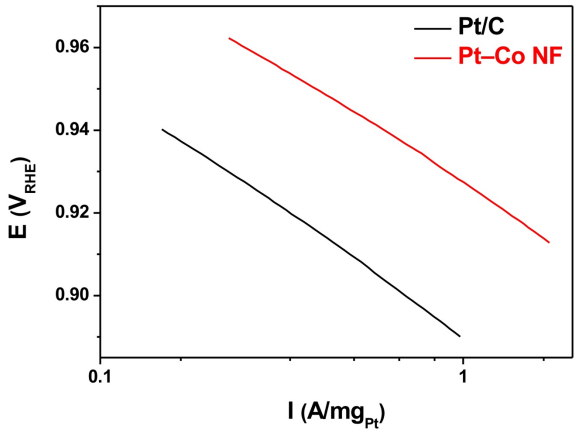

Figure 3-6 Acidic ORR mass activity Tafel plot of Pt−Co NF. The corresponding Tafel slopes are 60 and 66 mV $decade^{-1}$ for Pt−Co NF and commercial Pt/C, respectively.

In addition to the acidic media, the ORR properties of Pt−Co NF were also studied in an alkaline environment of 1 M KOH. CV was performed on Pt−Co NF in a similar manner to derive the ECSA (Figure 3-5d), which was equal to that measured in an acidic electrolyte. Figure 3-5e describes the ORR polarization curves of Pt−Co NF and commercial Pt/C in alkali, demonstrating a huge gap of 35 mV in half-potential for the initial test. The initial specific activity and mass activity of Pt−Co NF at 0.9 V_{RHE} were 1.09 mA cm^{-2} and 0.55 A mg_{Pt}^{-1}, respectively, which were 5 and 3 times higher than those of commercial Pt/C (Figure 3-5f). Again, the enhanced activity is contributed by the Pt−Co component imparting an optimal binding of oxygenated intermediates to the surface. Possibly due to the strong corrosion of alkali, the Pt−Co NF exhibited partly worse stability in KOH than in $HClO_4$, as confirmed by the shift of ORR polarization curve in Figure 3-5e.[152] Nevertheless, mass activities of 0.37 and 0.31 A mg_{Pt}^{-1} still remained after 2,000 and 6,000 ADT cycles, respectively, which were still significantly higher than the initial values of commercial Pt/C (Figure 3-5f). The specific activities of Pt−Co NF in 1 M KOH after ADT are not available (N/A) due to the expansion of double-layer region in CV curves, making the calculation of the surface area by H_{upd}−, and, thus, the specific activity−inaccurate.

3.5 MOR Electrocatalytic Properties

Furthermore, we evaluated the MOR performances of Pt−Co NF in alkaline electrolyte, where the measurement was conducted in an Ar-saturated 1 M KOH solution with 1 M

methanol. Figure 3-7a plots the MOR CV curves of Pt−Co NF and commercial Pt/C, both of which show characteristic anodic peaks derived from MOR catalyzed by Pt. The specific activity and mass activity of Pt−Co NF determined by the maximum current in the positive scan were 8.56 mA cm^{-2} and 4.28 A mg_{Pt}^{-1}, respectively, which were 5- and 4-fold enhancements, compared with those of commercial Pt/C (Figure 3-7b). It has been reported that a major mechanism for catalyst deactivation in MOR is the poisoning of surface Pt atoms by the carbonaceous intermediates, such as CO.[146] In an attempt to elucidate the origins of the much improved MOR activity of Pt−Co NF, CO-stripping experiments were performed to probe the binding strength of CO to the surface. The CO oxidation peak occurred at 0.682 V_{RHE} for Pt−Co NF, which showed a negative shift of 25 mV, compared with that of commercial Pt/C at 0.707 V_{RHE} (Figure 3-7c). The prominent reduction of peak potential suggests that the incorporation of Co into Pt-based NF can largely facilitate the oxidative removal of CO and other carbonaceous poisons from the surface, which leads to excellent MOR activity.[149]

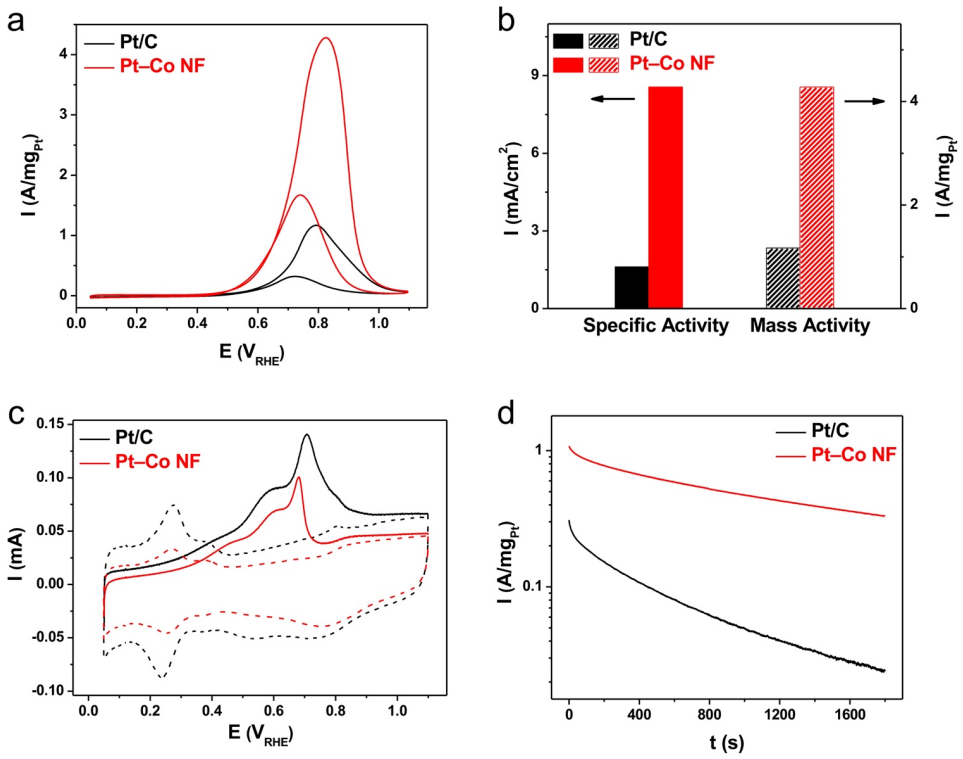

Figure 3-7 MOR performances of Pt−Co NF. (a) CV curves, (b) specific activities and mass activities, (c) CO-stripping curves, and (d) CA curves of Pt−Co NF and commercial Pt/C in 1 M KOH solution. CV curves were measured in Ar-saturated electrolyte containing 1 M methanol with a sweep rate of 50 mV s^{-1}. CO-stripping experiments were performed without the presence of methanol with a sweep rate of 50 mV s^{-1}. CA was conducted in Ar-saturated electrolyte with 1 M methanol at 0.67 V_{RHE}. In CO-stripping curves, the solid line is the first cycle and the dashed line is the second cycle.

Meanwhile, the stability of Pt−Co NF for MOR was evaluated by chronoamperometry (CA). CA responses of Pt−Co NF and commercial Pt/C were measured at 0.67 V_{RHE}, which was close to the onset potential of MOR (Figure 3-7d). Clearly, the activity of commercial Pt/C rapidly decreased from 0.31 A mg_{Pt}^{-1} to 0.02 A mg_{Pt}^{-1} after 1,800 s, which was a loss of almost 94% (Table 3-2). In contrast, the Pt−Co NF showed a milder degradation with a mass activity of 0.33 A mg_{Pt}^{-1} still remained in the end (Table 3-2). These results indicate that the Pt−Co NF are not only active but also durable for MOR in an alkaline environment.

Table 3-2 MOR stability of Pt−Co NF. Mass activities of Pt−Co NF and commercial Pt/C after different time of MOR at 0.67 V_{RHE} in 1 M KOH electrolyte with 1 M methanol.

I (A mg_{Pt}^{-1})	t = 0 s	t = 1,000 s	t = 1,800 s
Pt−Co NF	1.08	0.47	0.33
Pt/C	0.31	0.05	0.02

3.6 Structural Stability

Finally, the structural stability of Pt−Co NF after the electrocatalysis was investigated in terms of morphology, elemental distribution, and crystallinity. The low-magnification TEM images (Figures 3-8a−e) show that no obvious aggregation or agglomeration was observed for Pt−Co NF after various electrochemical measurements. The detailed morphology of Pt−Co NF was outlined by the HAADF-STEM images (Figures 3-8f−j), which demonstrate that the hollow nanoframe configuration was mostly maintained after both ORR and MOR measurements. We noticed that several edges of Pt−Co NF were broken after the alkaline ORR tests (Figures 3-8h,i), probably due to the strong corrosion of alkali with the assistance of O_2.[152] The EDX maps (Figures 3-8f−j) proved that Pt and Co were still uniformly distributed in the NF with no apparent variations of Co surface enrichment. Next, the HRTEM images and FFTs (Figures 3-4c−g) further confirmed that the morphology, crystallinity, and lattice spacing of Pt−Co NF were well kept after different electrolysis. The remarkable structural stability is related to the negligible Co loss during the ORR and MOR electrocatalysis (Table 3-1). The stable $Pt_{82}Co_{18}$ composition achieved by a precorrosion using nitric acid can prevent undesired electrochemical Co dissolution and concomitant surface reconstruction, as supported by our previous studies.[116]

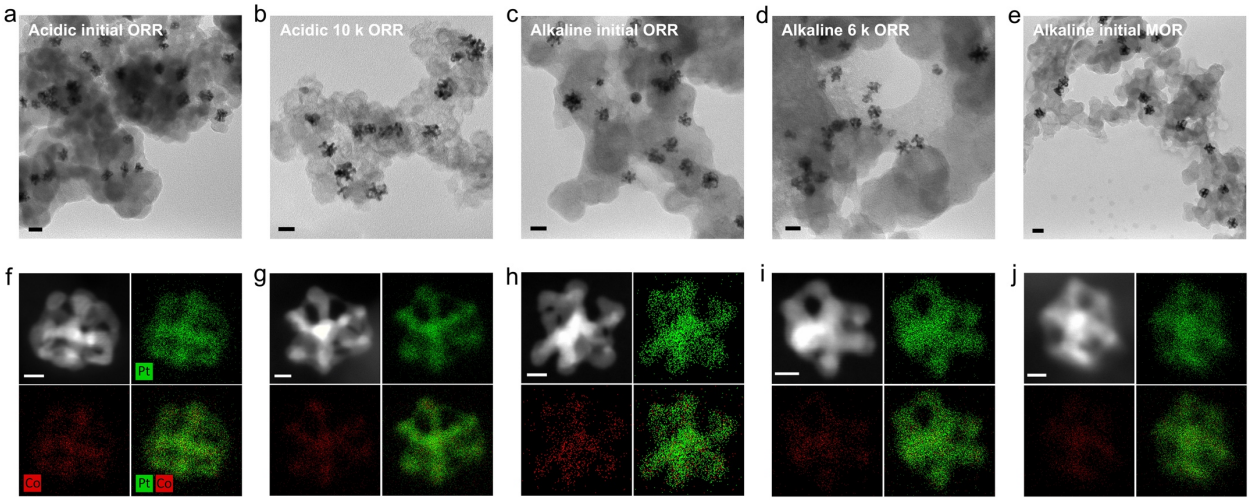

Figure 3-8 Structural stability of Pt−Co NF after the electrocatalysis. (a−e) TEM images and (f−j) HAADF-STEM images and EDX maps of Pt−Co NF after (a, f) initial and (b, g) 10,000 cycles of acidic ORR, (c, h) initial and (d, i) 6,000 cycles of alkaline ORR, and (e, j) initial alkaline MOR. In the EDX maps, green color represents Pt and red color represents Co. Scale bar is 20 nm in TEM images and 5 nm in HAADF-STEM images.

3.7 Conclusions

In conclusion, we first successfully synthesized Pt−Co RD with two segregated phases, the Pt-rich phase mainly concentrated on the edges and the Co-rich phase homogeneously distributed inside the particle. Then we etched away the Co-rich phase by nitric acid corrosion to prepare Pt−Co NF with an open surface and a hollow interior. The obtained Pt−Co NF exhibited remarkable behaviors for both ORR and MOR in acid/alkali, which largely outperformed those of commercial Pt/C, as well as outstanding structural stability after various electrocatalysis. The improved activity was contributed by the optimized binding strength of reaction intermediates, and the excellent stability was attributed to the robust surface with negligible electrochemical Co dissolution. These findings could serve as a guideline on how to rationally design nanocatalysts with the desired combination of morphology and composition to achieve superior properties.

3.8 Methods

Synthesis of Pt−Co RD. In a typical synthesis, 20 mg of $H_2PtCl_6{\cdot}6H_2O$ and 42.1 mg of $(CH_3COO)_2Co{\cdot}4H_2O$ were dissolved in 1.2 mL of oleylamine in a small vial by sonication. 6.8 mL of oleylamine and 2 mL of oleic acid were added into a 25 mL three-necked flask under N_2 purging. The solvent solution was first kept under vacuum at 160 °C for 2 minutes to entirely remove water, and then heated to 240 °C under N_2. The precursor solution was injected into the three-necked flask immediately after reaching 240 °C. The

color of the solution gradually changed from dark cyan to black at 240 °C. The reaction was stopped at 8 minutes after the injection by carefully transferring the flask into a water bath to quench the growth. The products were washed twice with hexane/ethanol mixture and collected by centrifugation at 12,000 rpm.

Catalyst loading. The Pt−Co RD collected by centrifugation were re-dispersed in chloroform and added to carbon black in a ratio which produced a loading of 8−10 wt% Pt. The mixture was shaken in chloroform for 3 minutes to complete the loading process. The loaded sample was washed twice with hexane and collected by centrifugation at 10,000 rpm.

Nitric acid corrosion. The as-loaded Pt−Co RD collected by centrifugation were re-dispersed in 10 mL of nitric acid (2M) aqueous solution by intense sonication. The mixture was heated at 60 °C under vigorous stirring for 1 hour in air to corrode Pt−Co RD into Pt−Co NF. The products were first washed once with pure ethanol and then washed twice with hexane/ethanol mixture. After each wash, the samples were collected by centrifugation at 12,000 rpm.

Preparation for electrochemical measurements. The Pt−Co NF catalyst supported on carbon was dispersed in a mixture of ethanol and Nafion 117 solution (volume ratio of 100:1) with a concentration of 0.5 $mg_{catalyst}$ mL^{-1}. The actual concentration of Pt in the catalyst ink was determined by ICP-OES. The catalyst ink was deposited onto a glassy carbon RDE (Pine Instruments, 0.196 cm^2) in the appropriate volume to achieve about 5.1 μg_{Pt} cm^{-2} loading density. The commercial Pt/C catalyst had a loading density of 8.2 μg_{Pt} cm^{-2}. The electrochemical measurements of ORR and MOR were conducted in a three-compartment glass electrochemical cell with a Pine RDE setup and a Biologic VSP potentiostat at room temperature. All potentials are presented versus the RHE.

Electrochemical measurements for acidic ORR. A saturated Ag/AgCl electrode and a Pt wire were used as reference and counter electrodes, respectively, and 0.1 M $HClO_4$ prepared from 67% $HClO_4$ was used as the electrolyte. The catalyst was activated by potential cycling in Ar-saturated electrolyte between 0.05−1.02 V_{RHE} with a sweep rate of 100 mV s^{-1} and was held at 0.05 V_{RHE} between measurements. The limits of CV were 0.05−1.02 V_{RHE}. H_{upd} measurements were performed by saturating the electrolyte with Ar gas before collecting the CV with a sweep rate of 50 mV s^{-1}. The ORR activity measurements were carried out under O_2 purging conditions and with a sweep rate of 20 mV s^{-1} with an RDE rotation rate of 1,600 rpm. The ADT was conducted by potential cycling in Ar-saturated 0.1 M $HClO_4$ electrolyte between 0.60 and 1.00 V_{RHE} with a sweep rate of 200 mV s^{-1}. The currents for acidic ORR were corrected for ohmic iR drop.

Electrochemical measurements for alkaline ORR and MOR. The catalyst was first activated by CV in Ar-saturated 0.1 M $HClO_4$ between 0.05 and 1.02 V_{RHE} with a sweep rate of 100 mV s^{-1}, and then transferred into the alkaline environment. An alkaline Hg/HgO electrode and a graphite rod were used as reference and counter electrodes, respectively, and 1 M KOH was used as the electrolyte. The limits of CV were 0.05−1.10 V_{RHE}, and the RDE rotation rate was always 2,000 rpm to get rid of bubbles. H_{upd} measurements were also performed by saturating the electrolyte with Ar gas before collecting the CV with a sweep rate of 50 mV s^{-1}. For alkaline ORR, the activity measurements were carried out under O_2 purging with a sweep rate of 20 mV s^{-1}, and the ADT was conducted by potential cycling in Ar-saturated electrolyte between 0.50 and 1.00 V_{RHE} with a sweep rate of 200 mV s^{-1} for different numbers of cycles. The currents for alkaline ORR were corrected for ohmic iR drop as well. For alkaline MOR, 1 M methanol was added into the electrolyte as the reactant, and the CV was collected under Ar purging with a sweep rate of 50 mV s^{-1}. CA was conducted in Ar-saturated electrolyte at 0.67 V_{RHE} for 1,800 seconds. CO-stripping measurements were performed by first purging CO through the electrolyte while holding the potential at 0.05 V_{RHE} without the existence of methanol. Ar was then purged to remove CO gas from the electrolyte, and the CV was collected with a sweep rate of 50 mV s^{-1}.

Chapter. 4 Individually Encapsulated Frame-in-Frame Structure

The contents and figures of this chapter are adapted or reprinted with permission from S. Chen, X.-Y. Liu, J. Jin, M. Gao, C. Chen, Q. Kong, Z. Ji, G. A. Somorjai, O. M. Yaghi, and P. Yang,* "Individually Encapsulated Frame-in-Frame Structure", *ACS Materials Letters* **2020**, *2*, 685–690. DOI: 10.1021/acsmaterialslett.0c00161.

4.1 Preface

Adding a second material is an innovative approach to introducing catalytic functions beyond metal nanoparticles. In Chapter 4, we present the encasement of hollow Pt−Ni nanoframe in another porous metal−organic framework (MOF) to achieve individually encapsulated frame-in-frame structures. Both single core−shell and single yolk−shell structures are synthesized, and the growth mechanism is revealed. The obtained frame-in-frame nanocomposites are promising candidates for tandem or size-selective catalysis.

4.2 Introduction

Hollow or porous nanomaterials featuring open interiors have shown great promise for applications in various fields.[154-156] Among these is the Pt−Ni nanoframe, a highly open framework of particular interest for its excellent catalytic performance.[45] The improved activity arises from both the hollow morphology, which provides 3D accessibility of the reactants to the surface, and the Pt−Ni composition, which is favorable for multiple important chemical reactions.[45,132,157] Until now, a diversity of approaches have been employed to tailor its catalytic behavior, such as controlling the architecture by creating Pt-rich sheets, changing the transition-metal component to Co, and altering the catalyst processing with different corrosion procedures.[116,133,138,158] However, few attempts have been made to combine the Pt−Ni nanoframe with a second material to introduce functions beyond metal nanoparticles.

MOFs, which are known as a class of crystalline nanoporous structures with well-defined pores and designed chemical properties, are one of the most commonly used materials to fabricate metal nanoparticle catalysts by constructing the core−shell structure.[159-161] While the metal nanoparticle core serves as the active center for catalysis, the MOF shell is able to accomplish numerous additional functionalities.[162] For example, multifarious composites of noble-metal particles embedded in MOFs have been shown to effectively increase the size selectivity of hydrogenation−a fundamental reaction to produce fine chemicals.[162,163] The MOF shell only selectively transports the substrates smaller than its

pores to the catalyst surface, thus achieving the molecular sieving effect.[162] Nevertheless, previous studies have mainly focused on solid metal nanoparticles.[164,165] There are only limited reports on capturing another hollow structure as the core in the porous MOF shell, within which the encasement is yet not well-controlled at a one-to-one ratio.[166,167] The one-to-one stoichiometry is especially important because of its high controllability for potential mechanism studies, as well as its ability to prohibit the adverse aggregation of nanoparticles in catalysis.[159] Here, we report the individual encapsulation of Pt−Ni nanoframe in a single-crystalline zeolitic imidazolate framework-8 (ZIF-8), which is a special MOF, to achieve both core−shell and yolk−shell frame-in-frame structures.

4.3 Single Core−Shell Structure

Surface functionalization of metal nanoparticles with specific ligands has been proven to play a critical role in diverse patterns of encapsulation.[168,169] Notably, hexadecyltrimethylammonium bromide (CTAB) is a unique surfactant that enables individual encasement and controlled alignment.[169] In this regard, the amphiphilic CTAB molecules were first introduced onto the surfaces of the as-synthesized hydrophobic Pt−Ni nanoframes (Figure 4-1a) by covering the original oleylamine ligand layer.[170] The obtained surface-functionalized Pt−Ni nanoframes could be well-dispersed in water with almost no aggregates (Figure 4-1b) and were then added into the aqueous growth solution of ZIF-8 to prepare the single core−shell frame-in-frame composite (Figure 4-2a).

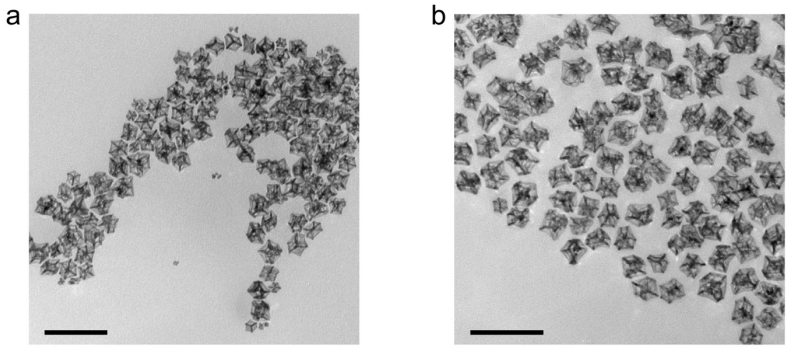

Figure 4-1 Surface functionalization of Pt−Ni nanoframes. TEM images of Pt−Ni nanoframes (a) with only oleylamine dispersed in hexane and (b) with overlaid CTAB dispersed in water. Scale bar is 100 nm in all images.

The TEM images (Figures 4-2b,c) show that only one rhombic dodecahedral nanoframe core is captured in one cubic ZIF-8 shell, being confined to the one-to-one stoichiometry. It has been reported that CTAB is a key bridging layer for this individual encapsulation.[169] On the larger scale, almost every Pt−Ni nanoframe was embedded solely in ZIF-8 with very few free nanocrystals outside, and about half of the ZIF-8 contained an nanoframe

in its interior (Figures 4-2c and 4-3a). The low-magnification TEM image of the Pt−Ni nanoframe encased in ZIF-8 (Figure 4-3a) is very different from that of their physical mixture (Figure 4-3b), certifying the successful encapsulation.

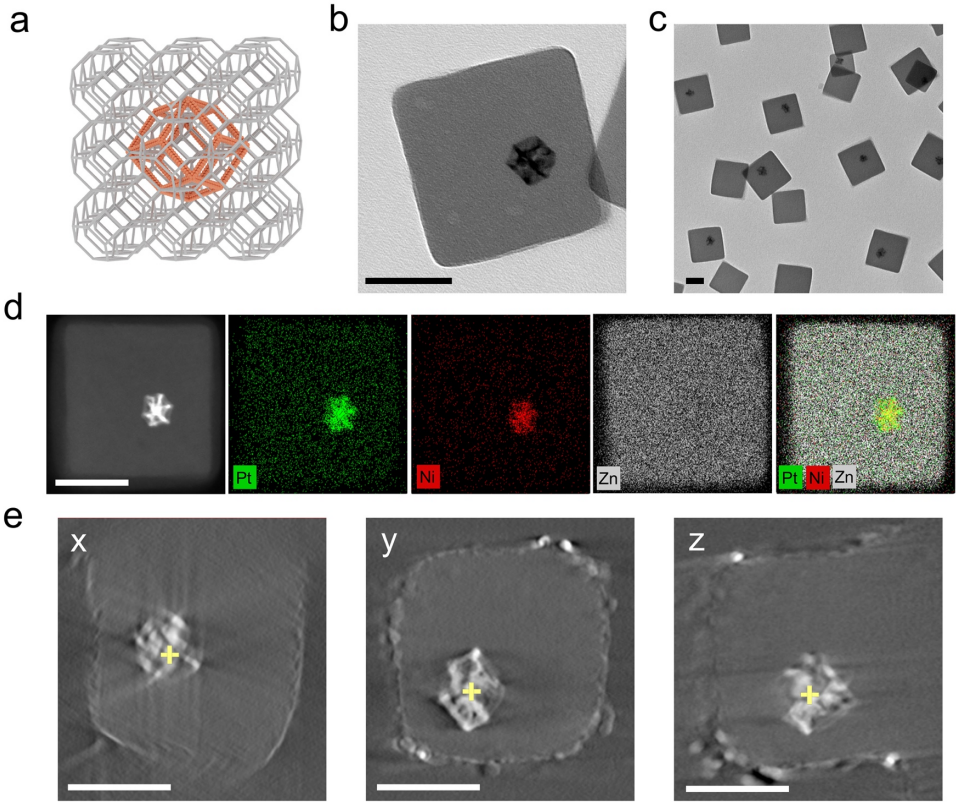

Figure 4-2 Characterizations of single core−shell frame-in-frame structure. (a) Model, (b, c) TEM images, (d) HAADF-STEM image and EDX maps, and (e) tomographic reconstruction images of single core−shell frame-in-frame structure. In the model, orange color represents Pt−Ni nanoframe and gray color represents ZIF-8. In the EDX maps, green color represents Pt, red color represents Ni, and gray color represents Zn. In the tomographic reconstruction images, yellow plus marker shows the same position in all three orthogonal slices. Scale bar is 50 nm in all images.

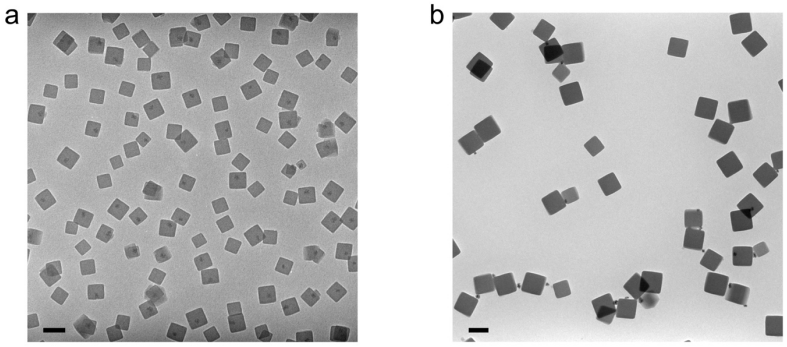

Figure 4-3 Morphology difference. Low-magnification TEM images of (a) Pt−Ni nanoframes encased in ZIF-8 and (b) Pt−Ni nanoframes mixed with ZIF-8. Scale bar is 100 nm in all images.

The XRD patterns also demonstrate the co-existence of these two materials (Figure 4-4). ZIF-8 exhibits signature peaks in the range of 5°−35° and the nanoframe shows (111) reflection of Pt−Ni alloy peak at ~41°. However, because of the limited abundance and small size of the nanoframe, the Pt−Ni alloy peak appears weak and broad (Figure 4-4b).

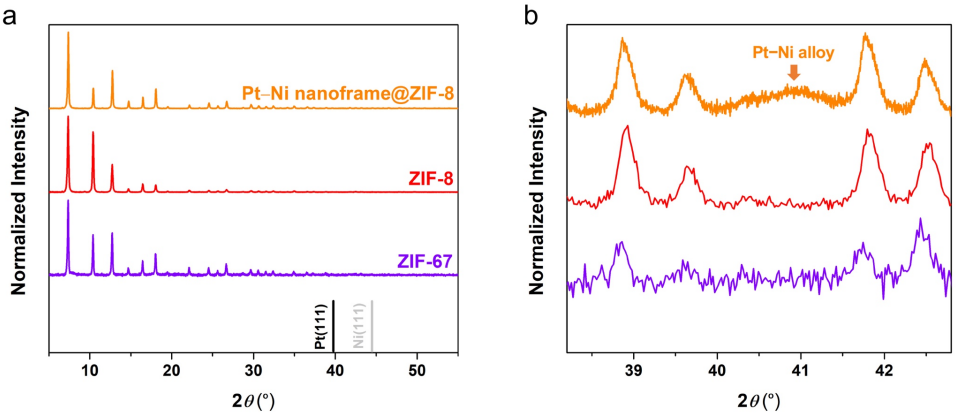

Figure 4-4 XRD patterns of single core−shell frame-in-frame structure. XRD patterns of ZIF-67, ZIF-8, and single core−shell Pt−Ni nanoframe encapsulated in ZIF-8 between (a) 5−55° and (b) 38−43°. Black line, Pt, PDF#03-065-2868; grey line, Ni, PDF#03-065-2865.

The HAADF-STEM image and EDX maps (Figure 4-2d) confirm that Zn spreads over the entire ZIF-8 as its metal node, while Pt and Ni only concentrate on the nanoframe. Note that ZIF-8 not only grew around the exterior of the nanoframe, but also filled in its interior, because no obvious fluctuation of Zn intensity was observed in the EDX line-scan profile (Figure 4-5). Such a complete encapsulation would maximize the surface interactions between Pt−Ni nanoframe and ZIF-8.

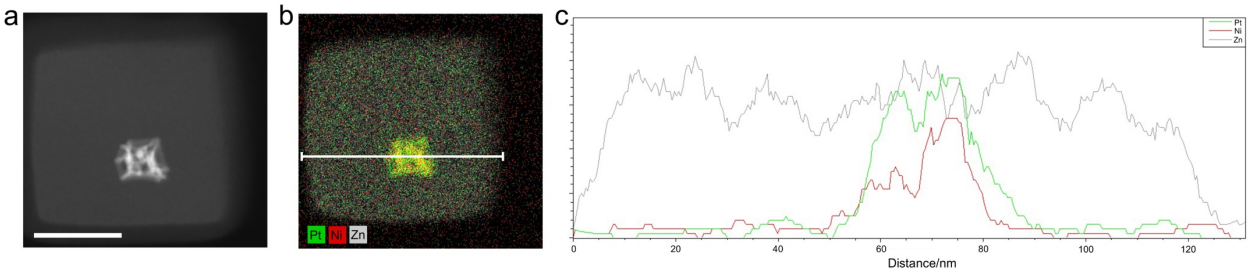

Figure 4-5 Elemental distribution of single core−shell frame-in-frame structure. (a) HAADF-STEM image, (b) EDX map, and (c) line-scan profile of single core−shell frame-in-frame structure. The MOF shell is ZIF-8. Scale bar is 50 nm.

In addition to the 2D characterization tools, tomography was further used to reconstruct the 3D morphology. Figure 4-2e clearly shows that the Pt−Ni nanoframe always remains within the scope of ZIF-8 in all three orthogonal slices, which gives direct evidence that the nanoframe is indeed embedded inside ZIF-8, rather than attached on the surface.

The scanning electron microscopy (SEM) image (Figure 4-6) also provides 3D proof that most of the nanoframes are captured inside ZIF-8.

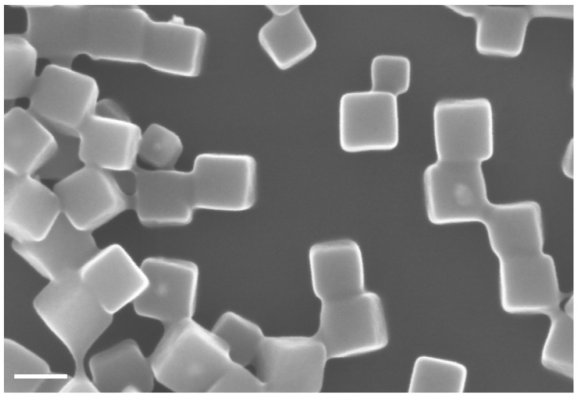

Figure 4-6 SEM image of single core−shell frame-in-frame structure. The MOF shell is ZIF-8. Scale bar is 100 nm.

Statistical analysis of the TEM images illustrated that there was no controlled alignment between the facets of Pt−Ni nanoframes and those of ZIF-8 (Figures 4-7 and 4-8). Various types of lattice alignments, as revealed by the relative orientations between the two frames in Figure 4-7, almost occurred at a similar frequency with no evident precedence. Although CTAB has been reported to direct the alignments between the (100) facets of Pd cubic nanoparticles and the (110) facets of ZIF-8, the random orientation discovered here could possibly be related to the limited abundance of the (100) surfaces on the nanoframes or the existence of the underlying oleylamine layer.[169]

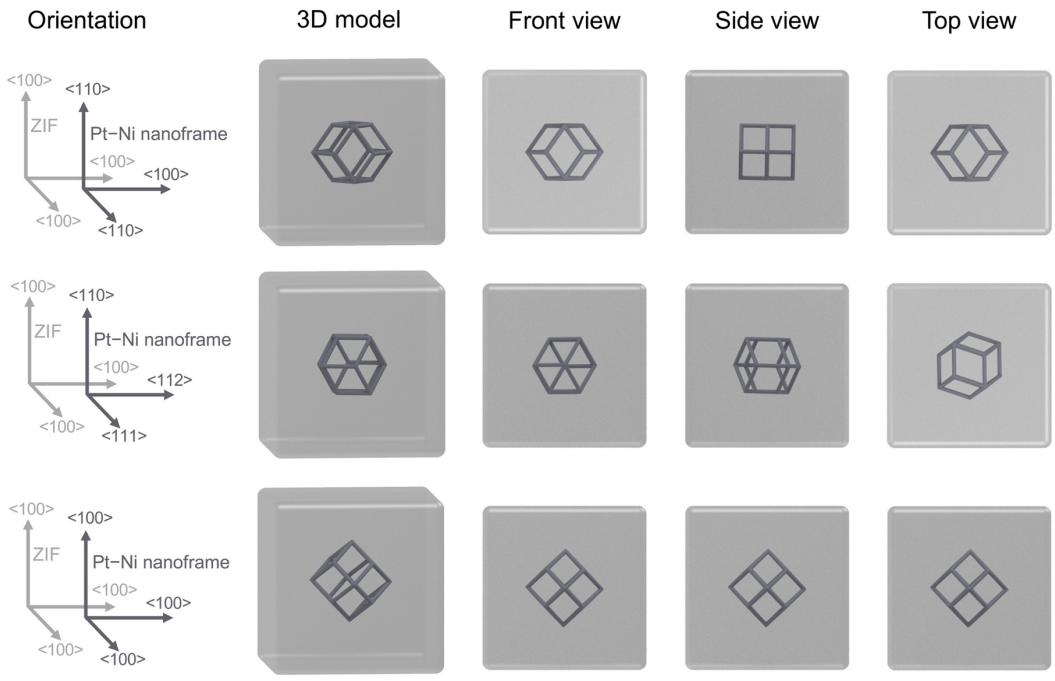

Figure 4-7 Models of alignments. Models of alignments between Pt−Ni nanoframe and ZIF in single core−shell structure.

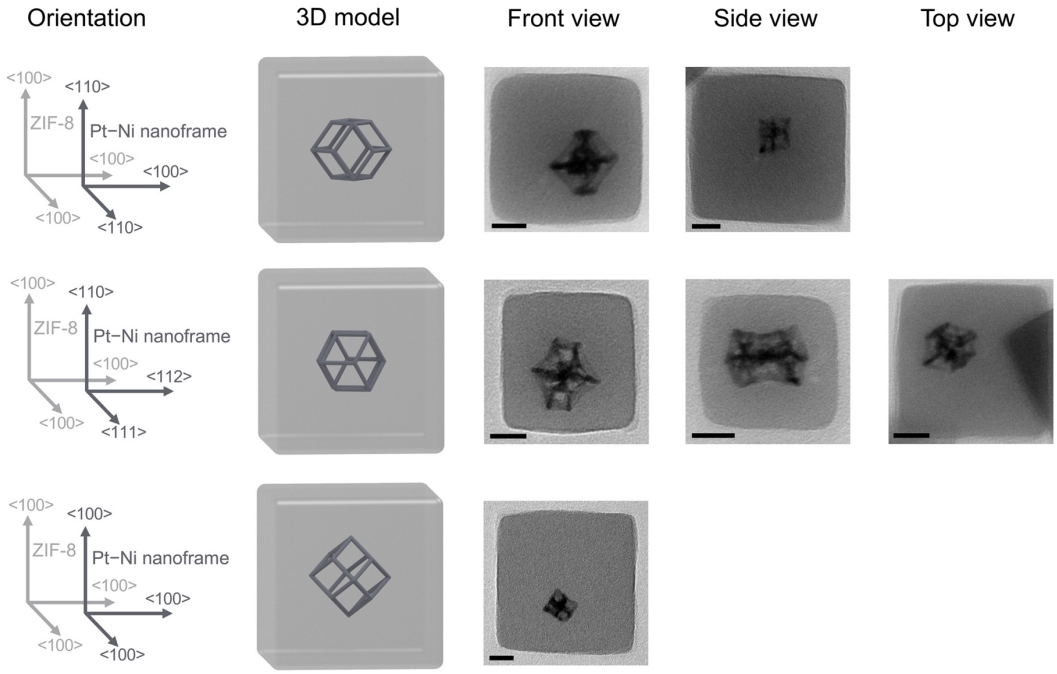

Figure 4-8 TEM images of alignments. TEM images of alignments between Pt−Ni nanoframe and ZIF-8 in single core−shell structure. Scale bar is 20 nm in all images.

4.4 Growth Mechanism

In an attempt to elucidate the unique individual encapsulation, the growth mechanism of the single core−shell frame-in-frame structure was studied by quenching the reaction at different times. The starting time point was when the Pt−Ni nanoframes were added into the growth solution of ZIF-8. The complete trajectory is described in Figure 4-9 and may be divided into four stages. First, ZIF-8 nucleated into small clusters in the solution before the addition of the nanoframes, which were identified as the light black dots in Figure 4-9a. Next, the nucleus randomly attached to the surface of the nanoframe through the CTAB bridging layer (Figure 4-9b). Note that no more than one nanoframe was attached to a single ZIF-8 nucleus, probably because of the size difference and steric hindrance, eventually leading to the one-in-one compound. ZIF-8 then grew exclusively on this nucleus to capture the entire Pt−Ni nanoframe (Figures 4-9c−e). The ZIF-8 shell was initially irregularly shaped at ~50 nm (Figure 4-9c). Nevertheless, it gradually turned into the cubic structure, because of the stabilizing effect of CTAB in water, and reached a size of ~60 nm (Figure 4-9d), which further increased to ~80 nm when the embedding was fully completed (Figure 4-9e).[171] Finally, with even longer growth time, the ZIF-8 shell continued to grow until ~100 nm (Figure 4-9f). This growth process is

similar to the previous report and offers strong support to understanding the mechanism of the individual encapsulation.[169]

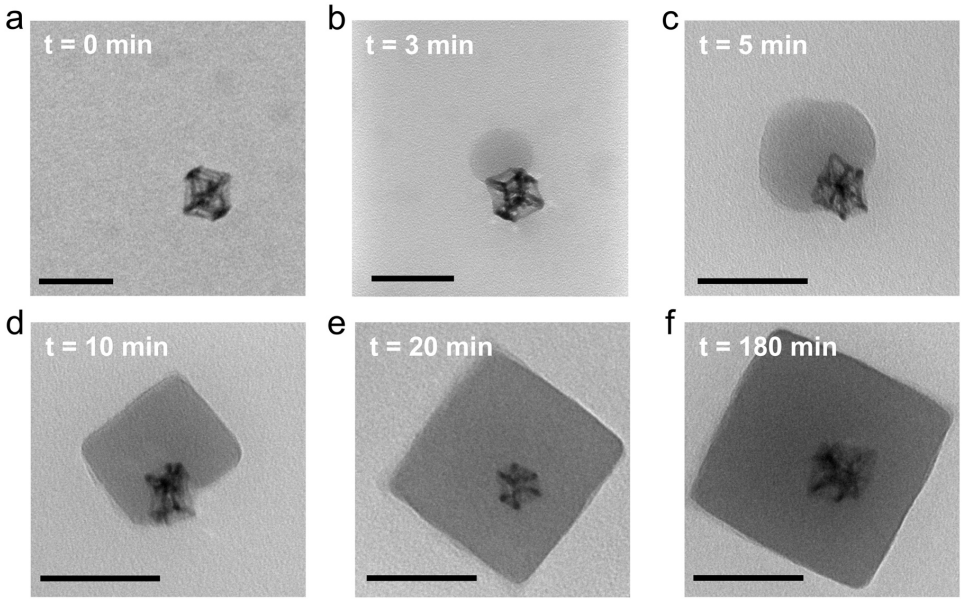

Figure 4-9 Growth trajectory of single core−shell frame-in-frame structure. TEM images of single core−shell frame-in-frame structure with growth time of (a) 0 min, (b) 3 min, (c) 5 min, (d) 10 min, (e) 20 min, and (f) 180 min. The starting time point is when the Pt−Ni nanoframes are added into the growth solution of ZIF-8. Scale bar is 50 nm in all images.

4.5 Single Yolk−Shell Structure

By utilizing the same concept, the Pt−Ni nanoframe was further individually captured in ZIF-8 to synthesize the single yolk−shell frame-in-frame structure, which possessed a cavity between the core and the shell (Figure 4-10).[172] First, the CTAB-covered Pt−Ni nanoframe was singly encapsulated in ZIF-67 to form the core−shell structure (Figures 4-10a,d), using the identical procedure as ZIF-8. ZIF-67 has the same sodalite structure as ZIF-8 (Figure 4-4), only with different metal ion of Co.[173] Hence, the Pt−Ni nanoframe core was also randomly oriented in the ZIF-67 shell (Figure 4-11). Then, ZIF-8 was overgrown in methanol to generate the double-shelled structure (Figures 4-10b,e). Here, the outer ZIF-8 shell featured the morphology of a truncated rhombic dodecahedron instead of a cube, because the capping effect of CTAB did not function in organic solvents.[171,174] Lastly, the composite was slowly dissolved in a mixture of water and methanol for several days to obtain the yolk−shell structure (Figures 4-10c,f). Upon the corrosion of water, ZIF-67 was dissociated to create the inner cavity while ZIF-8 was maintained as the outer shell. During the etching of ZIF-67, the Co ions dissociated and formed sheet-like Co hydroxides, which acted as the support to hold the cavity layers.[175]

Meanwhile, the ZIF-8 shell changed back into the cubic configuration, which again was attributed to the shaping effect of CTAB in aqueous solution. Such a synthetic route was also confirmed by EDX mapping (Figures 4-10g–i). Initially, only Co was detected in the starting core–shell structure as the signature of ZIF-67 (Figure 4-10g). However, an outer layer of Zn was observed to surround the inner Co after the overgrowth, implying the co-existence of ZIF-67 and ZIF-8 to achieve the double-shelled structure (Figure 4-10h). After the dissociation, Zn was still located in its own shells, while Co was distributed along the sheet-like structures, as evidenced by the formation of Co hydroxides, as discussed above (Figure 4-10i). Also note that the Co hydroxides did not fill the pore of the nanoframe, which was supported by the negligible Co intensity at the nanoframe location in the EDX map (Figure 4-10i).

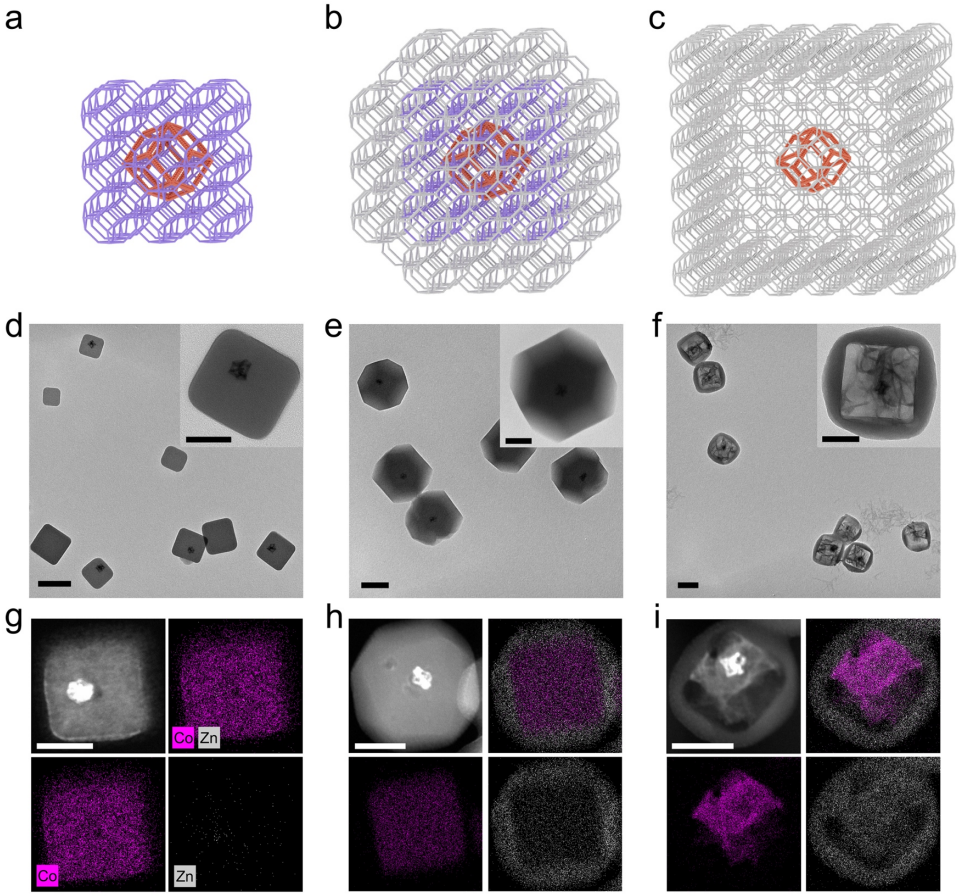

Figure 4-10 Synthetic route of single yolk–shell frame-in-frame structure. (a–c) Models, (d–f) TEM images, and (g–i) HAADF-STEM images and EDX maps of individually encapsulated (a, d, g) core–shell, (b, e, h) double-shelled, and (c, f, i) yolk–shell frame-in-frame structures. In the models, orange color represents Pt–Ni nanoframe, purple color represents ZIF-67, and gray color represents ZIF-8. In the EDX maps, purple color represents Co and gray color represents Zn. Scale bar is 100 nm in low-magnification TEM images and 50 nm in the corresponding insets, and 50 nm in HAADF-STEM images.

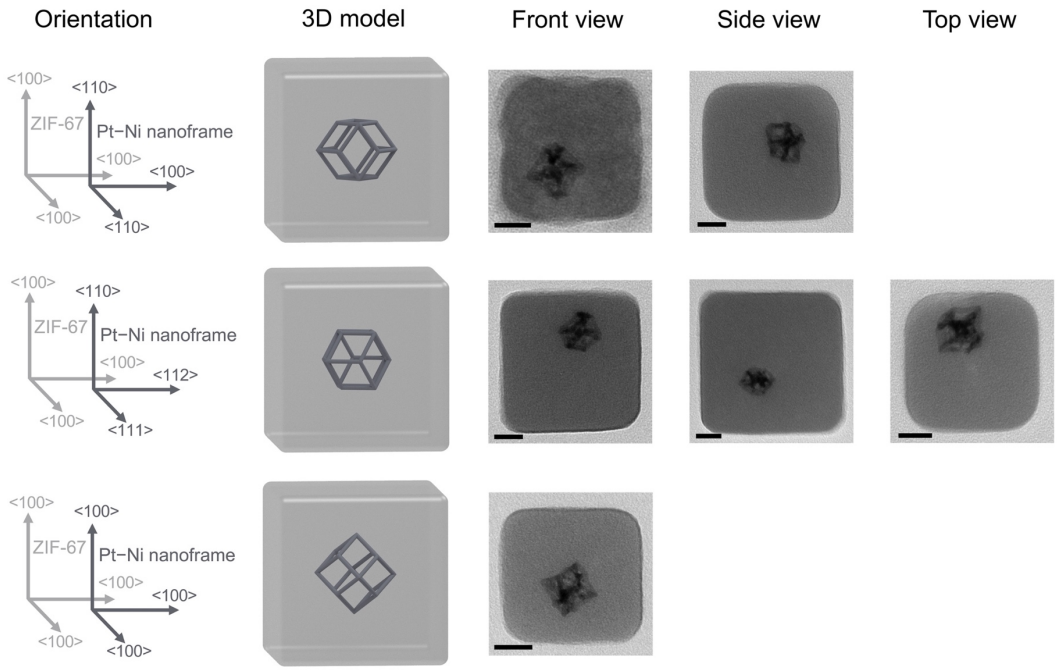

Figure 4-11 TEM images of alignments. TEM images of alignments between Pt−Ni nanoframe and ZIF-67 in single core−shell structure. Scale bar is 20 nm in all images.

4.6 Catalytic Applications

Via combining the catalytic properties of Pt−Ni nanoframe and ZIF-8, these individually encapsulated frame-in-frame structures are promising candidates for size-selective or tandem catalysis to produce fine chemicals for energy or commodity use. First, for size-selective catalysis, the MOF shell can implement the molecular sieving function by only transporting the reactants that are smaller than its pores to the inner catalyst surface for hydrogenation.[159] For example, the Pt/ZIF-8 composite has been reported to selectively catalyze the hydrogenation of small *n*-hexene but not large *cis*-cyclooctene.[168] Second, for tandem catalysis, the MOF shell can act as a second catalytic center in addition to metal particle, thus completing the cascade reaction.[159] For instance, the ZIF-8 can first catalyze the Knoevenagel condensation at the shell, and the Pt-based material could then catalyze the sequential hydrogenation at the core.[176]

4.7 Conclusions

In conclusion, we showed the individual encapsulation of Pt−Ni nanoframe in ZIF-8 to prepare the single core−shell frame-in-frame structure via the surface functionalization with CTAB. The 3D tomography confirmed that the nanoframe was indeed embedded inside ZIF-8 rather than attached on the surface. The growth mechanism of such frame-

in-frame structure was studied, in which the one-nanoframe-to-one-ZIF-8 attachment resulted in the formation of the unique one-in-one composite. Moreover, the Pt−Ni nanoframe was further solely captured in ZIF-8 to construct the single yolk−shell frame-in-frame structure through the sequence of encasement, overgrowth, and dissociation. These frame-in-frame hybrid materials have potential applications for size-selective or tandem catalysis to produce fine chemicals.

4.8 Methods

Synthesis of Pt−Ni nanoframes. In the first step, the Pt−Ni rhombic dodecahedra were prepared as the starting material. To begin with, 20 mg of $H_2PtCl_6{\cdot}6H_2O$ and 14.5 mg of $Ni(NO_3)_2{\cdot}6H_2O$ were pre-dissolved in 0.7 mL of oleylamine by sonication, and 9.3 mL of oleylamine was pre-heated in a 25 mL three-necked flask at 160 °C for 1 h under N_2. Next, the metal precursor solution was injected into the flask and kept under vacuum for 2.5 min. Then, the reaction was heated to 265 °C with a ramping rate of 15 °C min^{-1} in N_2 atmosphere. The reaction was stopped at 4 min after the solution turned black at 265 °C by transferring the flask into a water bath. The products were washed with hexane/ethanol and collected by centrifugation at 12,000 rpm. In the second step, the Pt−Ni nanoframes were gained by chemical corrosion. The Pt−Ni rhombic dodecahedra collected by centrifugation were re-dispersed in 2 mL of toluene and 5 mL of acetic acid by sonication. The mixture was heated at 90 °C under stirring for 2 h in air to allow the evolution from rhombic dodecahedra to nanoframes. The products were washed with hexane/ethanol and collected by centrifugation at 12,000 rpm.

Surface functionalization of Pt−Ni nanoframes with CTAB. The as-prepared Pt−Ni nanoframes collected by centrifugation were re-dispersed in 4 mL of 10 mM CTAB aqueous solution through intense sonication. The mixture was then sonicated at room temperature for about a week until all the Pt−Ni nanoframes became well-dispersed in water. The products were washed with water and collected by centrifugation at 14,000 rpm.

Individual encapsulation of Pt−Ni nanoframe in ZIF-8. The CTAB-covered Pt−Ni nanoframes collected by centrifugation were re-dispersed in 0.5 mL of pure water by sonication. Meanwhile, 1.75 mL of aqueous solution including 0.55 mM CTAB and 790 mM 2-methylimidazole was stirred at 500 rpm for 5 min in a 20 mL vial. Next, 0.25 mL of 97.5 mM $Zn(NO_3)_2{\cdot}6H_2O$ aqueous solution was added into the vial. After stirring for 10 s, the nanoframe solution was added into the mixture and stirred for another 5 min at 500 rpm. Then, the stir bar was taken out and the solution was left undisturbed for 3 h at room temperature. The products were collected by centrifugation at 10,000 rpm.

Individual encapsulation of Pt−Ni nanoframe in ZIF-67. The procedure was the same as that of ZIF-8 except that $Co(NO_3)_2 \cdot 6H_2O$ was used instead of $Zn(NO_3)_2 \cdot 6H_2O$.

Overgrowth of ZIF-8 on ZIF-67 to generate double-shelled structure. The Pt−Ni nanoframe@ZIF-67 core−shell composites collected by centrifugation were first re-dispersed in 1mL of methanol by sonication. Next, 0.2 mL of the mixture was added into 2.5 mL of 30 mM 2-methylimidazole methanol solution in a vial and shaken for 5 s. Then, 2.5 mL of 30 mM $Zn(NO_3)_2 \cdot 6H_2O$ methanol solution was added into the vial and shaken for another 5 s. The solution was left undisturbed for 1 h at room temperature and the products were collected by centrifugation at 6,000 rpm.

Dissolution of ZIF-67 to form yolk−shell structure. The Pt−Ni nanoframe@ZIF-67 @ZIF-8 double-shelled composites collected by centrifugation were re-dispersed in 1 mL of methanol in a vial by sonication, followed by the addition 1 mL of water. The solution was left undisturbed for about 3 days at room temperature to allow the complete dissolution of ZIF-67.

Chapter. 5 Ordering of Cu@Au Core−Shell Nanowires into Thermally Stable Cu_3Au Intermetallic Nanowires

The contents and figures of this chapter are adapted or reprinted with permission from Z. Niu,† S. Chen,† Y. Yu, T. Lei, A. Dehestani, K. Schierle-Arndt, and P. Yang,* "Morphology-Controlled Transformation of Cu@Au Core−Shell Nanowires into Thermally Stable Cu_3Au Intermetallic Nanowires", *Nano Research* **2020**, *13*, 2564–2569. DOI: 10.1007/s12274-020-2900-z. [177]

5.1 Preface

Achieving long-range ordering in nanocrystals holds the promise of enhanced catalytic behaviors. In Chapter 5, we demonstrate the morphology-controlled transformation of Cu@Au core−shell nanowires into Cu_3Au intermetallic nanowires under heat treatment. Thermally-driven atomic diffusion accounts for this transformation and is facilitated by the abundant twin boundaries. The resulting fully ordered Cu_3Au nanowires possess uniform and accurate atomic positioning in the crystal lattice, as well as improved thermal stability in air. These Cu_3Au intermetallic nanowires have potential catalytic applications for ORR and CO_2RR.

5.2 Introduction

Multimetallic nanocrystals have applications in catalysis, plasmonics, electronics, and sensors.[178-180] The atomic positioning of each metal component in the nanocrystals offers an effective way to tune their physical and chemical properties.[45,132,181] The most common solid mixtures include solid solutions, intermetallic compounds, and heterostructures. Among the three, intermetallic compounds are characterized by defined stoichiometry and ordered atomic arrangement. The highly ordered atomic positioning in intermetallic compounds gives rise to geometric and electronic homogeneity. Moreover, intermetallics generally exhibit improved stability against oxidation and etching than the random alloy counterparts with identical composition.[182,183] The enhanced stabilities are attributed to the more negative enthalpy of formation, or the existence of noble metal overlayers.[105,184]

Although the intermetallic compounds are thermodynamically more stable than the solid solutions below the order−disorder transition temperature (T_C), wet-chemical synthesis commonly yields random alloys because of the relatively high kinetic barriers of ordering. Thermal annealing has been proven an effective way to convert preformed nanocrystals

into intermetallics.[185-187] However, during the thermal treatment, the nanocrystals tend to evolve into spherical particles,[188] and grow larger via agglomeration and Ostwald ripening. Protective shells (MgO, SiO_2, and polydopamine) were therefore employed to mitigate the particle sintering.[189-191] Uniform intermetallic nanoparticles with reduced particle sizes (sub-10 nm) have been made using this encapsulation approach.[192,193] Despite the progress in size control, shape control of intermetallic nanocrystals remains a formidable task. The morphologies of the preformed nanocrystals can hardly maintain during the thermal annealing because of the accelerated surface diffusion at elevated temperatures.[188,194] So far, only a few intermetallic nanocrystals have been achieved with well-defined shapes, including Pt−Sn, Pt−Pb, Pt−Bi, Pd−Sn, and Pd−Cu.[42,195-201] Here, we demonstrate a shape-preserving conversion of Cu@Au core−shell nanowires to Cu_3Au intermetallic nanowires.

5.3 Synthesis and Characterizations

The Cu−Au system has been widely used as an ideal system to study the disorder−order phase transformation.[202-204] This is because the Cu−Au system is featured by continuous series of solid solutions, as well as various forms of intermetallic structures. In order to achieve shape preservation during thermal treatment, it is a necessity to achieve disorder −to−order transition at a lower annealing temperature. One strategy that comes to the forefront is to introduce vacancies/defects into the material, which can lower the kinetic barriers of atom diffusion.[205,206] Therefore, raising the vacancy/defect concentration will greatly facilitate the ordering process.[184,207]

In this regard, we chose the defective and highly strained Cu nanowires as the starting material for the synthesis of Cu_3Au intermetallic nanowires. The Cu nanowires were prepared using a free radical approach developed by our group (Figure 5-1a).[208] The five-fold twinned structure of Cu nanowires is well documented.[208-211] Each wire can be considered to consist of five single-crystalline grains separated by five twin planes (i.e., planar defects) aligned along the wire axis. The gaps between the adjacent grains (inset in Figure 5-1b) can give rise to lattice strains and distortions, as reflected in the XRD which presents perceptible peak asymmetry and peak splitting (Figure 5-1b, blue line).[212,213] As a reference, single-crystalline Cu nanocubes exhibited reflections with highly symmetric shapes (Figure 5-1b, red line). We reasoned that the existence of these planar defects in nanowire would help the subsequent disorder−order transition. An appropriate amount of Au was then coated on the as-made Cu nanowires to reach a stoichiometric composition close to Cu_3Au, through epitaxial deposition following the procedure reported previously.[214] It should be noted that the Au deposition was conducted at a temperature (130 °C) lower than the synthetic temperature (165 °C) of

the parent Cu nanowires. Therefore, it is reasonable to assume that the internal lattice defects near the twin planes were kept in the resultant Cu@Au core−shell nanowires. The as-made Cu@Au core−shell nanowires had an average diameter of 22 ± 5 nm (Figures 5-2a,b). Between the shell and the core could be observed clear and even interface (Figures 5-2b,c), where the atomic diffusion would occur.

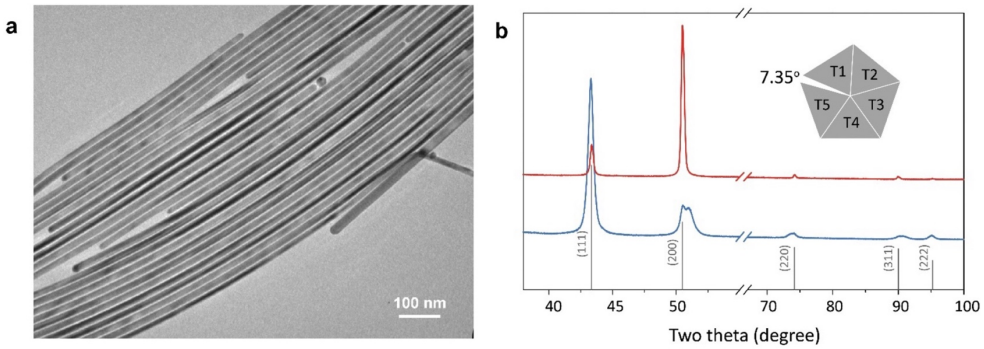

Figure 5-1 Characterizations of Cu nanowires. (a) TEM image of five-fold twinned Cu nanowires which serve as seeds for the growth of Cu@Au core−shell nanowires. (b) XRD patterns of five-fold twinned Cu nanowires (blue line) and single-crystalline Cu nanocubes (red line) acquired with a Cu Kα source. The peak splitting and peak asymmetry for Cu nanowires indicate the prevalence of lattice strain and distortion arising from the twin boundaries. Grey lines represent the reference reflections of Cu (JCPDS#65-9026).

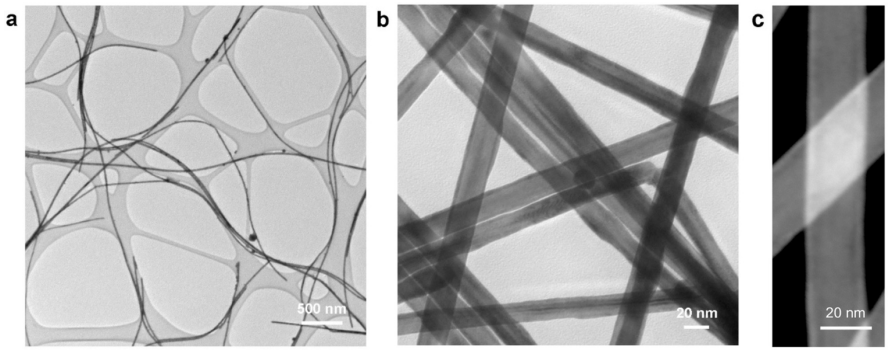

Figure 5-2 Characterizations of Cu@Au core−shell nanowires. (a, b) TEM images and (c) HAADF-STEM image of Cu@Au core−shell nanowires.

To make Cu_3Au intermetallic nanowires, the as-prepared Cu@Au core−shell nanowires were subjected to thermal annealing under the forming gas (10% H_2/Ar). Figure 5-3a presents the evolution of XRD patterns of Cu@Au core−shell nanowires after being annealed at progressively increased temperatures, with a duration of one hour for each. In general, there are three distinct stages that can be recognized from the XRD evolution: below 200 °C, from 200 to 220 °C, and above 220 °C. Specifically, the pristine Cu@Au core−shell nanowires exhibited major peaks similar to fcc Cu. A hump showed up between the Cu(111) and Au(111) diffractions, suggesting partial mixing of Au and Cu in the vicinity of core/shell interface. The hump evolved into a broad peak after annealing

at 140 °C, positioning at a 2θ value of 46°. It can be assigned to the reflection of A1 Cu−Au(111). Further increasing the annealing temperature from 160 to 200 °C, the A1 Cu−Au(111) reflection slightly shifted toward higher 2θ values (Figure 5-3b) and its integral intensity dramatically increased in relative to that of Cu(111) (Figure 5-3c). These observations indicate a higher degree of mixing between Au and Cu upon thermal treatment. Meanwhile, weak superlattice reflections (100 and 110) began to appear when the annealing temperature was above 160 °C. Tetragonal intermetallic CuAu ($L1_0$ phase) mixed with Cu could be identified in the sample after annealing at both 180 and 200 °C (Figure 5-3a). These results suggest that the phase transition temperature was reduced for the five-fold twinned nanowires as compared with the bulk CuAu (ca. 235−310 °C).[215] While the XRD patterns followed a gradual evolution below 200 °C, a drastic change took place when elevating the annealing temperature to 220 °C. A new set of reflections, which could be assigned to cubic intermetallic Cu_3Au ($L1_2$ phase), suddenly showed up in replacement of tetragonal CuAu phase. This transformation was accompanied by the consumption of Cu phase, as reflected by the largely reduced peak intensities of Cu(111) and Cu(200). Thereafter, with the proceeding of atomic diffusion at even higher temperatures (≥240 °C), more and more residual Cu was incorporated into the lattice of $L1_2$ phase of Cu_3Au until a complete transformation finished at 320 °C. The one-dimensional morphology was well preserved in the final products (Figure 5-4).

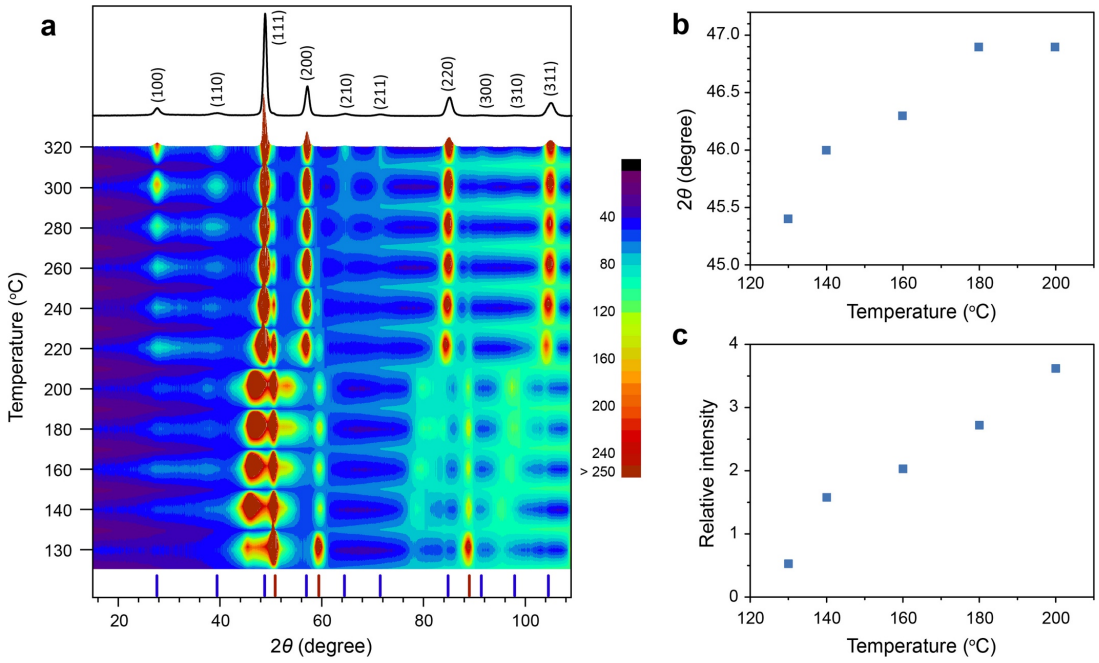

Figure 5-3 Structural transformation. (a) Contour surface of the XRD evolution of Cu@Au core−shell nanowires after annealing at temperatures from 140 to 320 °C. Blue and red lines represent the reference reflections of $L1_2$ Cu_3Au (JCPDS#65-9737) and Cu (JCPDS#65-9026), respectively. (b) The two-theta value of the A1 Cu−Au(111) reflection as a function of the annealing temperature. (c) The temperature-dependence of the integral intensity of A1 Cu−Au(111) reflection in relative to that of Cu(111) reflection.

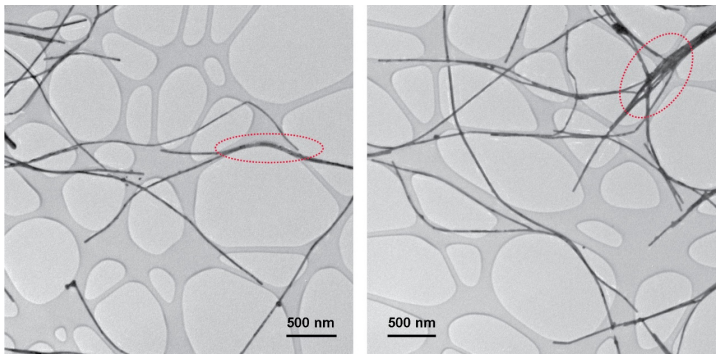

Figure 5-4 Morphology of Cu_3Au intermetallic nanowires in solid-state. TEM images of $L1_2$ Cu_3Au nanowires obtained by annealing at 320 °C under forming gas. Nanowires that were close to each other on the substrate would sinter during the annealing process (red circles).

It is conceivable that a diffusion layer would form at the Cu/Au interface in response to thermal annealing. The diffusion layer can be considered as an interface joint between co-existing phases. It would provide a venue for the mixing and ordering of Cu and Au atoms. This hypothesis is substantiated by elemental mappings using EDX. As depicted in Figure 5-5a, the initial Cu@Au core−shell nanowire had Cu (green) uniformly coated by a conformal shell of Au (red). The compositional line-scan profile across the wire also suggests a core−shell configuration of the two elements. There was appreciable change in the elemental distribution after annealing at 200 °C (Figure 5-5b). Au was no longer enriched on the surface of Cu wire, but spread inward instead. The corresponding line-scan profile shows that the Au peaks were fully in the shade of the Cu signals, indicative of the diffusion and mixing of the two elements from the outer shell. Figure 5-5c shows the elemental mapping of the final $L1_2$ Cu_3Au nanowire, wherein the Cu and Au were homogeneously distributed, very different from the initial core−shell arrangement.

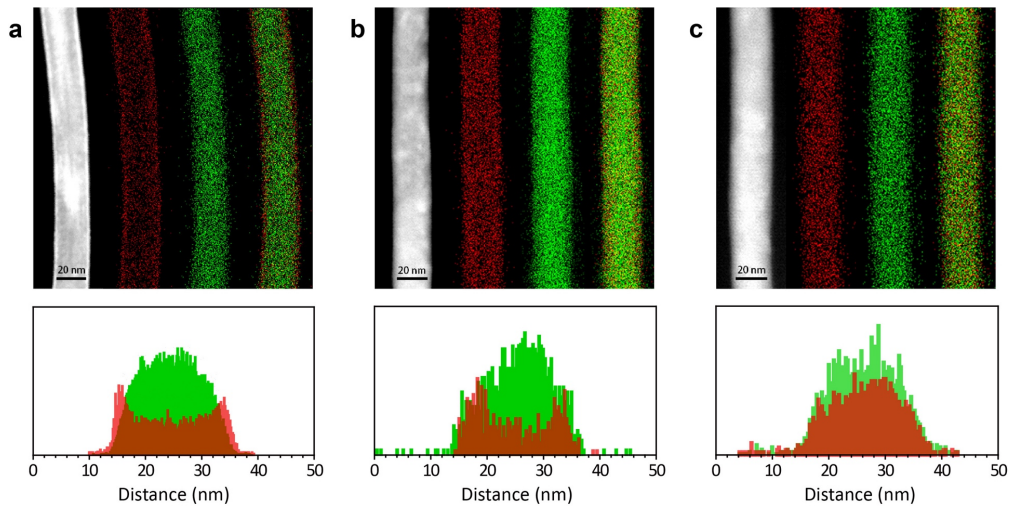

Figure 5-5 Atomic diffusion. HAADF-STEM images, EDX elemental mappings, and line-scan profiles (bottom panels) of (a) a pristine Cu@Au core−shell nanowire, (b) an intermediate gained after annealing

at 200 °C, and (c) a product obtained after annealing at 320 °C. Green and red colors represent Cu and Au, respectively.

The atomic arrangement in the $L1_2$ Cu_3Au nanowire was further investigated using HAADF-STEM. Figure 5-6 shows the atomic-resolution images of the $L1_2$ Cu_3Au viewed along three different orientations, i.e., [-112], [011], and [-111], respectively. Because the contrast in HAADF-STEM image is proportional to the square of atomic number (Z), Au atom columns have higher intensity than Cu in the images. The periodic oscillations of bright (Au) and dark (Cu) columns directly reflect the ordered lattice in the $L1_2$ Cu_3Au nanowire. The intensity profiles measured across the nanowire are given in the insets in Figure 5-6. The projected atomic arrangements along different zone axes (Figures 5-6c,f,i) exhibit oblique, rectangular, and hexagonal lattices, respectively. These results clearly indicate the highly ordered structure of the resultant Cu_3Au nanowire.

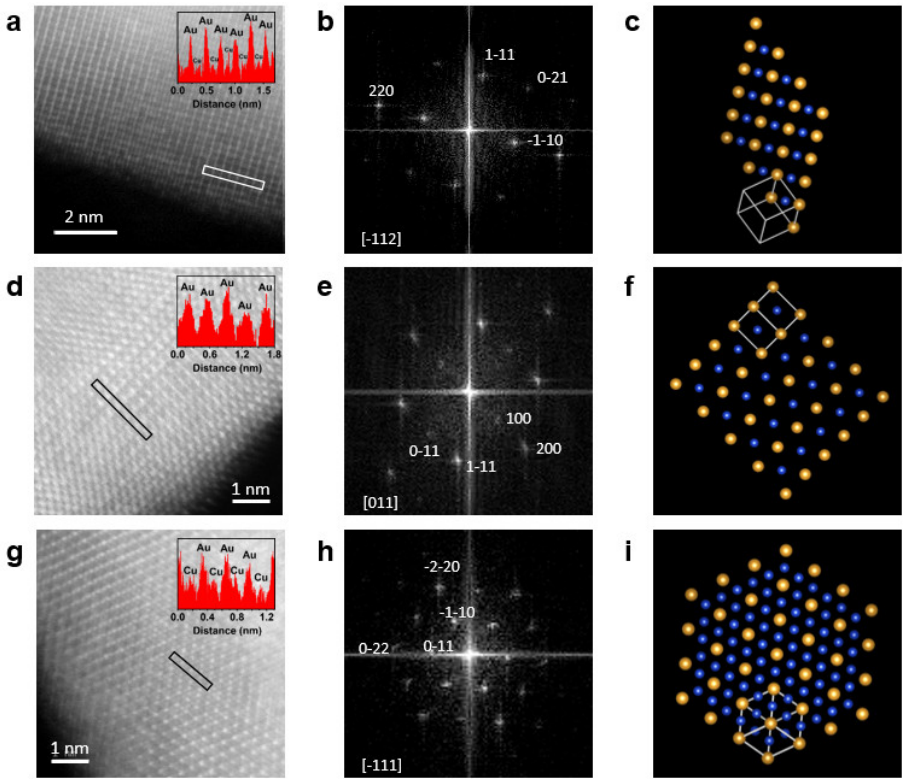

Figure 5-6 Atomic arrangements of Cu_3Au intermetallic nanowire. (a, d, g) Aberration-corrected HAADF-STEM images, (b, e, h) FFTs, and (c, f, i) projected unit cells along the [-112], [011], and [-111] axes of the $L1_2$ Cu_3Au intermetallic nanowires. Blue and yellow spheres represent Cu and Au atoms, respectively.

We noticed that wire sintering was not completely suppressed under the forming gas annealing if the wires were too close to each other on the substrate. As highlighted in Figure 5-4, a bunch of wires melted together after the thermal treatment at 320 °C. More

benign annealing conditions are desired to address this problem. Since $L1_2$ Cu_3Au was already observed at 220 °C (Figure 5-3a), we attempted to convert Cu@Au core−shell nanowires into intermetallics at 220 °C with prolonged annealing treatment. Figure 5-7 shows the time-dependent XRD patterns. In general, extending the duration of thermal treatment did make the $L1_2$ Cu_3Au phase more dominant in the products, although a very weak Cu(111) reflection still remained. This is probably because the diffusion of remaining Cu needs to cross a longer distance.

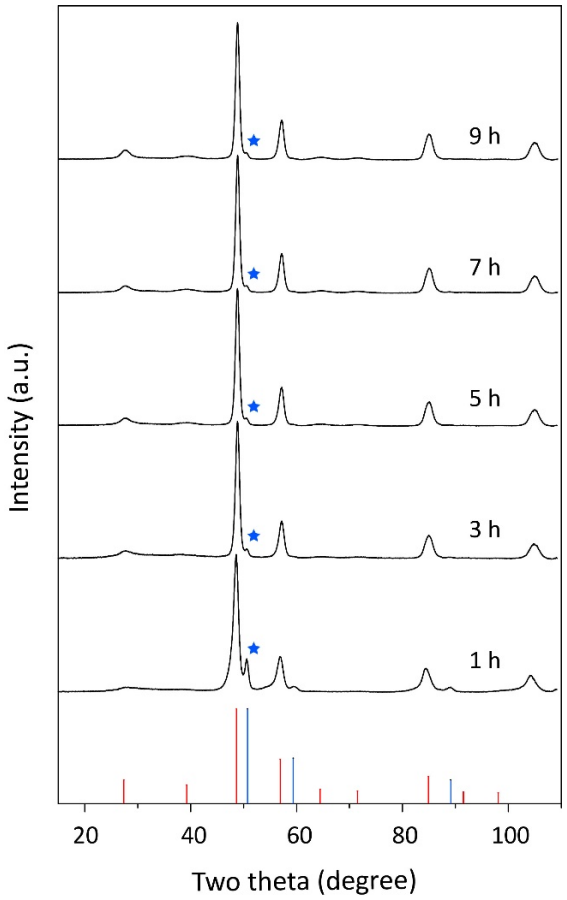

Figure 5-7 Ordering of Cu@Au core−shell nanowires at 220 °C. XRD evolution of Cu@Au core−shell nanowires after annealing at 220 °C with different durations. Blue stars mark the presence of weak Cu(111) reflections. Red and blue lines represent reference $L1_2$ Cu_3Au (JCPDS#65-9737) and Cu (JCPDS#65-9026), respectively. The XRD was acquired with a Co Kα source. The $L1_2$ Cu_3Au phase became more dominant in the product with prolonged annealing time at 220 °C.

Alternatively, we also carried out thermal treatment in high boiling-point solvent (1-octadecene). We expected that a high coverage of capping agents (oleylamine and oleic acid) on the surface of nanowires would keep them from sinter. Indeed, the resultant Cu_3Au intermetallic nanowires were better dispersed than those made by forming gas annealing, but the length of the nanowires became relatively short (Figure 5-8).

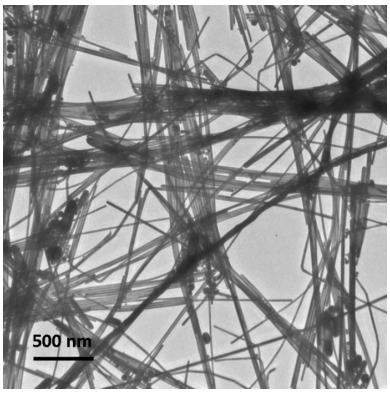

Figure 5-8 Morphology of Cu_3Au intermetallic nanowires in liquid-phase. TEM image of $L1_2$ Cu_3Au nanowires obtained by annealing at 335 °C for one hour in 1-octadecene. The coalescence of nanowires was suppressed.

5.4 Thermal Stability

Cu–Au intermetallic compounds have shown great promise in applications regarding catalysis, coating, and electronic devices.[106,216,217] Previously, we reported that Cu@Au core–shell nanowires were more stable against humidity and air than Cu nanowires.[214] Here, we further compare the stability of Cu, Cu@Au, and $L1_2$ Cu_3Au nanowires under air annealing at temperatures up to 300 °C. No obvious morphological changes were observed in ordered Cu_3Au nanowires until 250 °C, at which the wire surfaces started to become rough (Figure 5-9a). In contrast, similar structural degradations were observed for Cu@Au and Cu nanowires at much lower temperatures. Pieces of low-contrast flakes appeared on Cu@Au core−shell nanowires at 200 °C, while the surfaces of pure Cu nanowires were no longer smooth and intact at 150 °C (Figure 5-9a). The low-contrast surface species were identified to be copper oxides as revealed by elemental EDX mapping (Figure 5-10). The degradation process was then followed using XRD (Figures 5-9b–d). The reflections of copper oxides (Cu_2O and/or CuO) began to appear at 250 and 200 °C for ordered Cu_3Au and Cu@Au, respectively, in line with the morphological changes observed in the TEM. However, Cu nanowires already suffered from partial oxidation even at room temperature (RT), as evidenced by the presence of $Cu_2O(111)$ reflection. The intensity of $Cu_2O(111)$ gradually increased with elevated temperatures. It is worth noting that the cuprous oxides all transformed into cupric oxides above 250 °C. These results indicate that the thermal stability under oxidative atmosphere follows the order of $L1_2$ Cu_3Au intermetallic > Cu@Au core−shell > pure Cu nanowires. The oxidation-resistant property of $L1_2$ Cu_3Au nanowires could be attributed to the enhanced nobility of Cu atoms in the intermetallic lattice,[218] where the accurate atomic positioning leads to homogeneity of electronic structures.

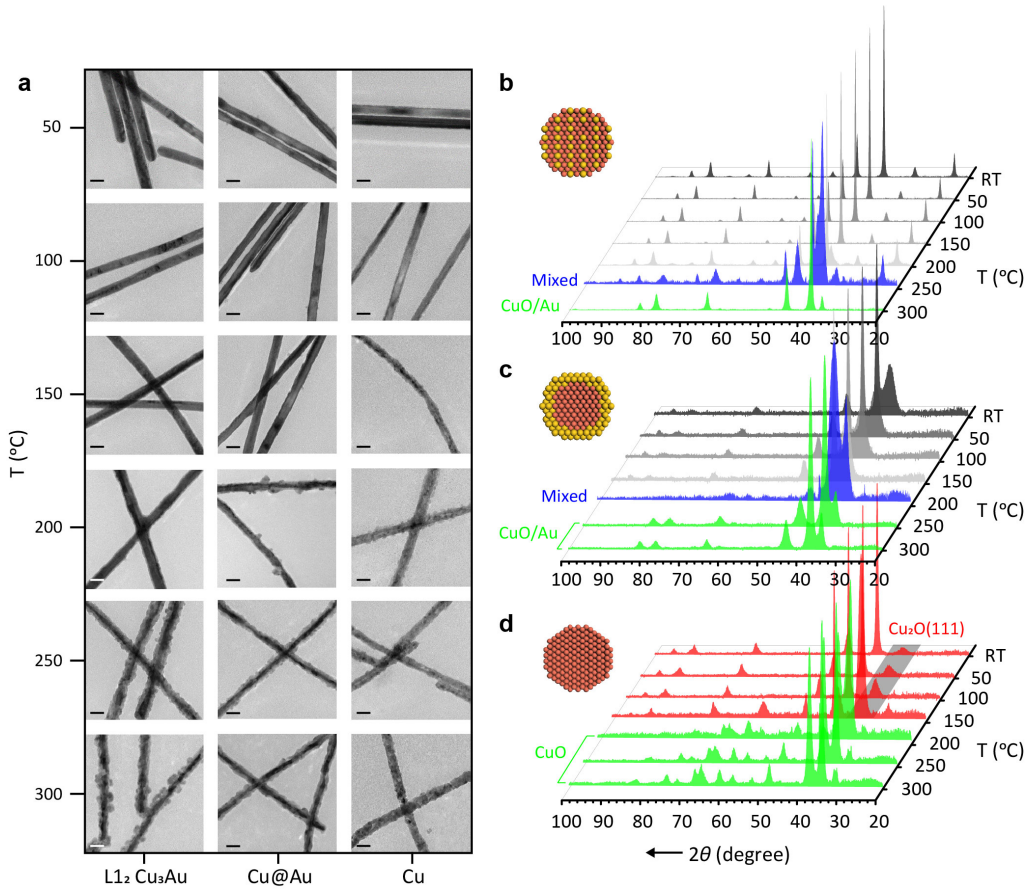

Figure 5-9 Thermal stability of Cu-based nanowires in air at different temperatures. (a) TEM images and (b–d) XRD patterns of (b) $L1_2$ Cu_3Au, (c) Cu@Au core−shell prepared at 140 °C, and (d) Cu nanowires after annealing in air for one hour at elevated temperatures. Scale bar is 20 nm in all images.

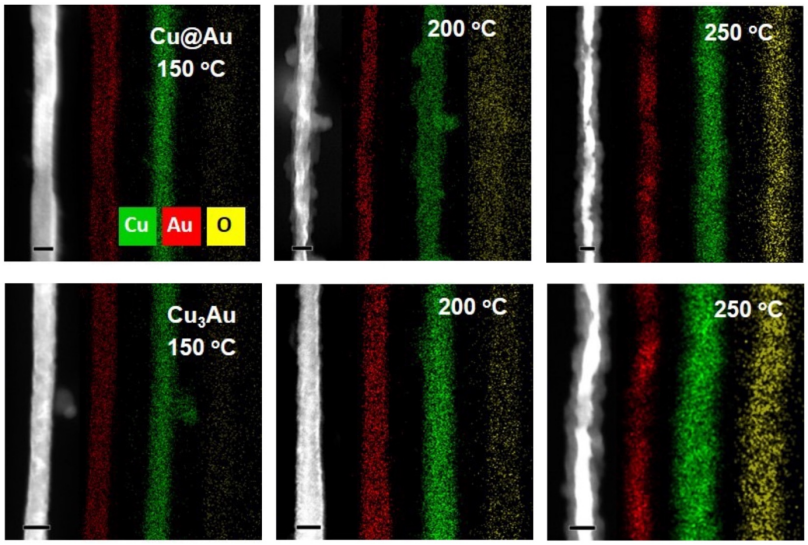

Figure 5-10 Characterizations of Cu-based nanowires after annealing in air. HAADF-STEM images and elemental EDX mappings of Cu@Au core−shell and $L1_2$ Cu_3Au nanowires after annealing in air for one hour at 150, 200, and 250 °C, respectively. Scale bars is 20 nm in all images.

5.5 Catalytic Applications

The resultant ordered $L1_2$ Cu_3Au nanowires have potential electrocatalytic applications for ORR and CO_2RR, according to the previous reports on Cu−Au intermetallics.[106,216,219] First, for ORR, the intermetallic Cu_3Au nanoparticles exhibited superior ORR properties in alkali, in which Cu assisted the O_2 activation and Au benefited the OH^- desorption.[219] And also, the CuAu nanoparticles with better structure-ordering showed better catalytic behavior for ORR than the disordered ones.[216] Second, for CO_2RR, the ordered CuAu particles selectively converted CO_2 to CO, while the disordered alloys were catalytically active for HER.[106]

5.6 Conclusions

In summary, we have shown a shape-controlled transformation of Cu@Au core−shell nanowires into Cu_3Au intermetallic nanowires. The ordering process was initiated at a relatively low temperature (160 °C) probably due to the presence of considerable twin planes in the parent nanowires, which can lower the kinetic barriers for atomic diffusion. During the transformation, $L1_0$ CuAu was identified as an intermediate phase below 200 °C, and a drastic phase transition from $L1_0$ CuAu to $L1_2$ Cu_3Au was observed when increasing the annealing temperature from 200 to 220 °C. The ordered Cu_3Au nanowires have shown enhanced thermal stability in air compared with Cu and Cu@Au core−shell nanowires. These Cu_3Au intermetallic nanowires are appealing candidates for ORR and CO_2RR electrocatalysis.

5.7 Methods

Synthesis of Cu nanowires. In a typical synthesis, 85 mg of $CuCl_2{\cdot}2H_2O$ (0.5 mmol) and 0.5 g of oleylamine were mixed in a Schlenk flask. The copper precursor was dissolved at 70 °C under stirring. The mixture was degassed for 30 min, followed by N_2 purging. Then, 0.5 g of tris(trimethylsily)silane (2 mmol) was added into the flask. The resultant blue solution was slowly heated up to 110 °C in an oil bath. When the color of the solution turned into clear yellow, the temperature of the oil bath was further increased to 165 °C. The reaction was left at this temperature for 16 h for the growth of Cu nanowires.

Synthesis of Cu@Au core−shell nanowires. Right after the growth of Cu nanowires, the reaction flask was placed in an oil bath pre-heated at 130 or 140 °C. The as-prepared Cu nanowires were kept in the growth solution under N_2 protection. $(Ph_3P)AuCl$ (80 mg) dissolved in trioctylphosphine (1 mL) was injected into the flask using syringe. The

reaction was maintained at this temperature for 1 h before cooling down to room temperature. The products were washed with toluene and collected by centrifugation at 8,000 rpm.

Transformation into Cu_3Au intermetallic nanowires (solid-state). The collected Cu@Au core−shell nanowires were re-dispersed in toluene and drop-casted on glass slides. The gained samples were annealed in H_2/Ar mixture (H_2/Ar:10/90) at different temperatures for 1 h. After cooling down, the samples were stored in N_2 box for further characterizations.

Transformation into Cu_3Au intermetallic nanowires (liquid-phase). The collected Cu@Au core−shell nanowires were re-dispersed in 6 mL of 1-octadecene, 0.2 mL of oleylamine, and 0.2 mL of oleic acid in a Schlenk flask. The mixture was degassed at 80 °C for 30 min followed by inert gas purging. Then, the flask was placed into a salt bath pre-heated at 335 °C and kept for 70 min under stirring at 60 rpm. After cooling down to room temperature, the products were washed with toluene and collected by centrifugation at 8,000 rpm.

Thermal annealing in air. The Cu-based nanowires were re-dispersed in toluene and loaded on proper substrates, such as Ni grids for TEM and glass slides for XRD. The muffle furnace was pre-heated at designated temperatures before the samples were put into it. The samples were taken out after one-hour thermal treatment in air, and stored in N_2 box for further characterizations.

Chapter. 6 Ligand Removal of Au_{25} Nanoclusters Using Thermal and Electrochemical Treatments for CO_2 Electroreduction to CO

The contents and figures of this chapter are adapted or reprinted with permission from S. Chen,† M. Li,† S. Yu, S. Louisia, W. Chuang, M. Gao, C. Chen, J. Jin, M. B. Salmeron, and P. Yang,* "Ligand Removal of Au_{25} Nanoclusters by Thermal and Electrochemical Treatments for Selective CO_2 Electroreduction to CO", *The Journal of Chemical Physics* **2021**, *155*, 051101. DOI: 10.1063/5.0059363. Copyright 2021 AIP Publishing.[220]

6.1 Preface

Stripping away the protecting ligands on nanomaterials can effectively expose the active surface sites and greatly enhance the catalytic properties. In Chapter 6, we study the ligand removal of Au_{25} nanoclusters and its influence on CO_2RR. The thiolate ligands can be readily cleaved under either thermal annealing at ≥180 °C or electrochemical biasing at ≤ -0.5 V_{RHE}. The Au_{25} nanoclusters after ligand-removing treatments show improved activity and selectivity for the electroreduction of CO_2 to CO.

6.2 Introduction

Metal nanoclusters with atomically precise structures are promising candidates for a wide range of catalytic reactions, among which CO_2 reduction has attracted growing attention as a sustainable approach to producing value-added fuels and chemicals.[221-224] These sub-2 nm clusters are typically synthesized with metal atoms as the core and thiolate ligands as the shell, which together form a well-defined motif to control the cluster size and crystal structure.[225-227] Due to their ultrasmall size, the nanoclusters develop quantized electronic structures and possess low coordination numbers of metal atoms.[109,110] All these unique features provide the nanoclusters with superior catalytic properties, as compared with the larger nanoparticles.[111] For example, multiple ultrafine clusters have exhibited remarkable catalytic performances for electrochemical CO_2 reduction, in which undercoordinated surface sites have been identified as the true active centers to improve the reactivity.[84,228,229] Therefore, it is critical to preserve and expose the undercoordination of metal nanoclusters as much as possible to further promote CO_2 electrocatalysis.

The stability problem always remains a great challenge for exploring the catalytic behaviors of metal nanoclusters.[230] They tend to agglomerate into larger nanoparticles under the harsh reaction conditions, which considerably destroys the nature of their

undercoordination.[231] To tackle this issue, sulfur-doped graphene (S-G) has been employed to stabilize the nanoclusters through strong catalyst–support interaction, which inhibits significant cluster coalescence within electrocatalytic environments.[232] Although the stability is enhanced, the activity of metal nanoclusters is still limited by the protecting thiolate ligands on the surface.[233] For example, thiols can passivate the surface of Au catalysts because of the strong Au–S bonding.[234,235] Despite the possibility of changing the electronic structure of metal clusters, these capping ligands not only impose steric restriction on the accessibility of molecular reactants but also block the active undercoordinated surface atoms from being available for catalysis.[113,236] Moreover, theoretical calculations have predicted that the ligand-removed sites on metal clusters are responsible for enhanced CO_2 reduction properties.[114] In this regard, here we study the removal process of thiolate ligands from Au_{25} nanoclusters by both thermal annealing and electrochemical biasing. The Au_{25} nanoclusters after ligand-removing treatments exhibit improved activity and selectivity for CO_2 electroreduction to CO.

6.3 Synthesis and Characterizations

Neutrally charged Au_{25} ($Au_{25}(PET)_{18}$, PET = 2-phenylethanethiol) nanoclusters were prepared following a reported solution-phase method and purified by passing through a silica column and a size-exclusion column subsequently (for experimental details, see the Methods section at 6.8).[237] The successful synthesis of the charge-neutral and pure Au_{25} nanoclusters was confirmed by the ultraviolet–visible spectroscopy (UV–vis) and electrospray ionization-mass spectrometry (ESI-MS). The UV–vis spectrum (Figure 6-1a) shows characteristic absorption peaks at 401, 461, 639, and 693 nm, which are consistent with the previously published results for neutral Au_{25} nanoclusters.[237] The ESI-MS spectrum (Figure 6-1b) exhibits signature peaks only at 7393 and 3696 of m/z, which conforms to the molecular weight of $Au_{25}(PET)_{18}$ with atomic accuracy and excludes the existence of other impurities. The crystal structure of Au_{25} nanocluster has been reported in the literature, which contains a Au_{13} icosahedron core surrounded by a shell of six –S–Au–S–Au–S– semiring motifs (Figure 6-2).[238] The TEM image (Figure 6-1c) shows the ultrasmall size and uniform distribution of Au_{25} nanoclusters at 1.3 ± 0.3 nm, which agrees well with the previously reported crystallography measurement.[239] The Au_{25} nanoclusters were then loaded on S-G by stir-mixing in toluene at room temperature for 1 h to obtain Au_{25}/S-G.[232] The TEM image of Au_{25}/S-G (Figure 6-1d) demonstrates that the Au_{25} nanoclusters were evenly distributed on the S-G substrate without noticeable aggregation or sintering, which was attributed to the dopant-anchoring effect of S-G.[232] The aberration-corrected STEM image (inset in Figure 6-1d) also verifies the size of the Au_{25} nanocluster after loading on S-G, in which the bright dots represent the Au atoms.

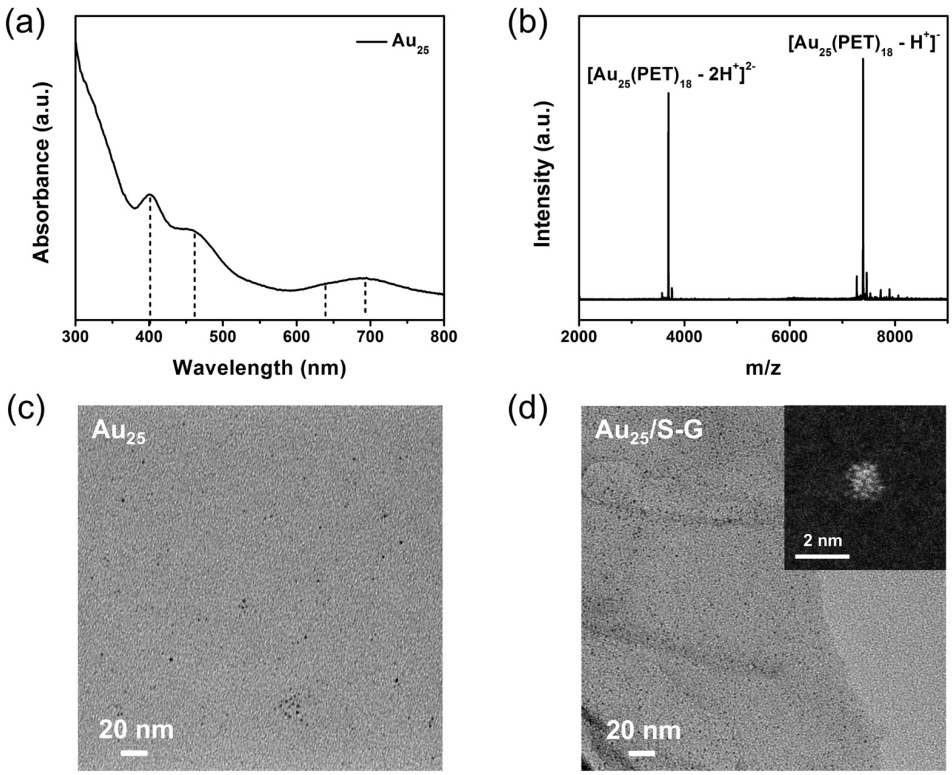

Figure 6-1 Structural characterizations of Au_{25} nanoclusters. (a) UV–vis spectrum, (b) ESI-MS spectrum, and (c) TEM image of Au_{25} nanoclusters. (d) TEM image of Au_{25} nanoclusters loaded on sulfur-doped graphene (Au_{25}/S-G). The inset is the aberration-corrected STEM image of the Au_{25} nanocluster after anchoring on S-G.

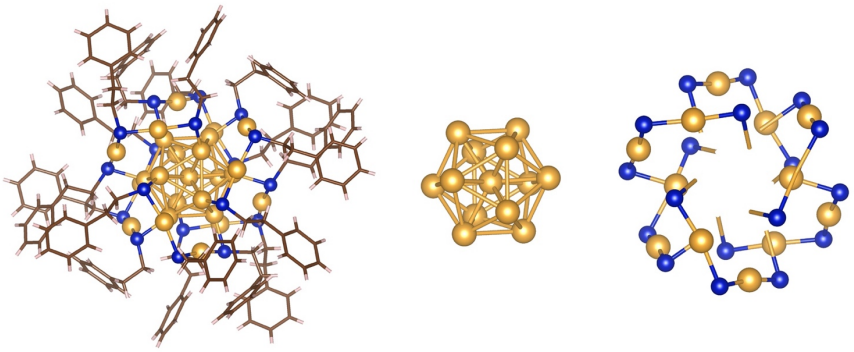

Figure 6-2 Crystal structure of Au_{25} nanocluster. The crystal structure is re-drawn from ref 238.[238] Yellow spheres represent Au atoms, and blue spheres represent S atoms. Brown color represents C atoms, and pink color represents H atoms.

6.4 Thermal Treatment

In order to investigate the ligand removal of Au_{25} nanoclusters, we first applied thermal treatment, which has been a general approach to strip away the ligands.[113,233] The Au_{25}/S-G with 57 μg of Au, as determined by ICP, was annealed in a 10% H_2/Ar atmosphere at different temperatures from 120 to 220 °C. The surface-sensitive Cu underpotential deposition (UPD) measurement was utilized to evaluate the degree of ligand removal by determining the surface area of exposed or ligand-free Au.[82] The electrochemically active surface area was calculated using the charges associated with the anodic stripping peak.[240] Both pristine and 120 °C annealed Au_{25}/S-G showed no peaks in the Cu UPD curves with surface areas close to zero (Figures 6-3a,b), which implied that their Au surfaces were inaccessible as they were fully blocked by the thiolate ligands. A weak stripping peak was clearly observed when the annealing temperature reached 150 °C, corresponding to a surface area of 1 cm^2 (Figure 6-4a). This indicates that the staple ligands of Au_{25} nanoclusters start to be cleaved at 150 °C. The anodic peak became larger at 180 °C, of which the surface area was 6 cm^2, and further grew at 220 °C, of which the surface area was 9 cm^2 (Figures 6-3a,b). This suggests that the capping ligands can be readily removed at elevated temperatures (≥180 °C), leaving a large amount of Au exposed on the surface. The extent of ligand removal was further estimated by the surface-specific X-ray photoelectron spectroscopy (XPS) technique via probing the oxidation state of Au in Au_{25}/S-G. The pristine and 120 °C annealed Au_{25}/S-G exhibited relatively higher binding energies for Au (Figure 6-3c), which were in accord with higher oxidation states. This implies that their surface Au atoms are still covalently bonded to the S atoms of the thiolate ligands. As the temperature increased to 150, 180, and 220 °C, the binding energies of Au in Au_{25}/S-G gradually turned lower (Figures 6-3c and 6-4b), suggesting that the surface Au became progressively more metallic. This indicates that more Au–S bonds are being cleaved, and thus, more thiolate ligands are removed at higher temperatures. Moreover, the ligand removal process was also studied by the extended X-ray absorption fine structure (EXAFS) spectroscopy at the Au L_3-edge, which probed the coordination environments of Au atoms. The pristine Au_{25}/S-G showed a similar spectrum to that reported in the literature (Figure 6-3d), in which the peak at ~1.9 Å corresponded to the Au–S coordination, and the following peaks at around 2.4 and 2.8 Å represented the Au–Au coordination.[233] The high intensity of the Au–S peak for pristine Au_{25}/S-G (Figure 6-3d) indicates that the Au atoms are highly bonded to the S atoms. Then, as the annealing temperature increased to 180 and 220 °C, the scattering amplitude of Au–S coordination gradually decreased (Figure 6-3d), which suggested that a growing number of thiolate ligands were removed from the Au catalysts. All of Cu UPD, XPS, and EXAFS evidenced that thermal annealing could effectively strip away the surface ligands from Au_{25} nanoclusters.

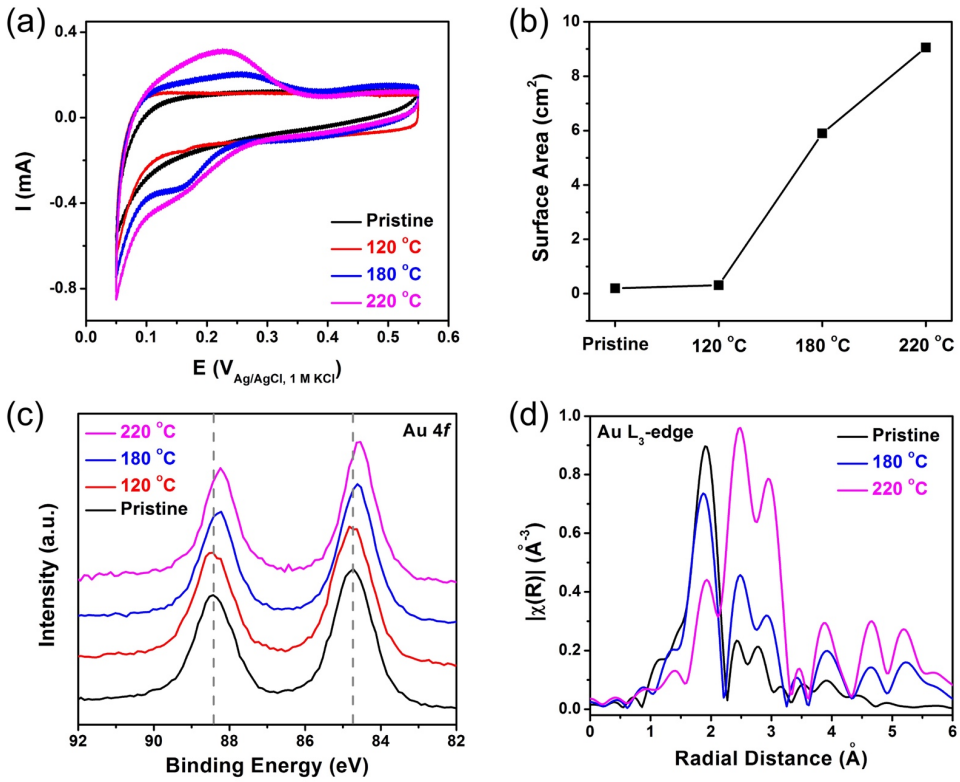

Figure 6-3 Structural characterizations of Au_{25}/S-G after thermal treatments. (a) Cu UPD curves, (b) surface areas, (c) Au 4*f* XPS spectra, and (d) Au L_3-edge EXAFS spectra of Au_{25}/S-G annealed at different temperatures.

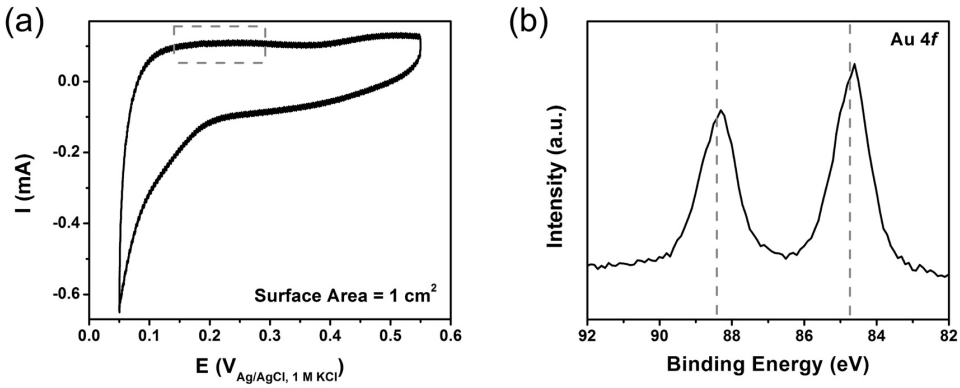

Figure 6-4 Structural characterizations of Au_{25}/S-G annealed at 150 °C. (a) Cu UPD curve and surface area, and (b) Au 4*f* XPS spectrum of Au_{25}/S-G annealed at 150 °C. Gray dashed line in XPS spectrum has the same position as that in Figure 6-3c for comparison.

However, the thermal annealing also triggered the structural evolution simultaneously, as visualized by TEM. The Au_{25}/S-G showed no obvious agglomeration at 120 °C (Figure 6-5a), at which the ligands were not removed at all. Once the ligands began to detach at 150 °C, slight sintering intermittently appeared with the formation of low-density 2–4 nm nanoparticles (Figure 6-5b). A noticeable number of larger nanoparticles, ranging

from 4 to 8 nm, were observed when the ligands were largely removed at 180 °C (Figure 6-5c). In addition, subsequently, more nanoparticles of 4–8 nm were found, while more ligands were being removed at 220 °C (Figure 6-5d). The structural transformation was supported by EXAFS as well. The peak intensity of Au–Au coordination for pristine Au_{25}/S-G was relatively small (Figure 6-3d) owing to their ultrafine size. However, it became progressively larger at higher temperatures (180 and 220 °C), as shown in Figure 6-3d, which correlated with the incremental appearance of larger particles seen in TEM (Figure 6-5). These results suggest that the ligand removal from these nanoclusters without concomitant agglomeration remains to be a challenge.

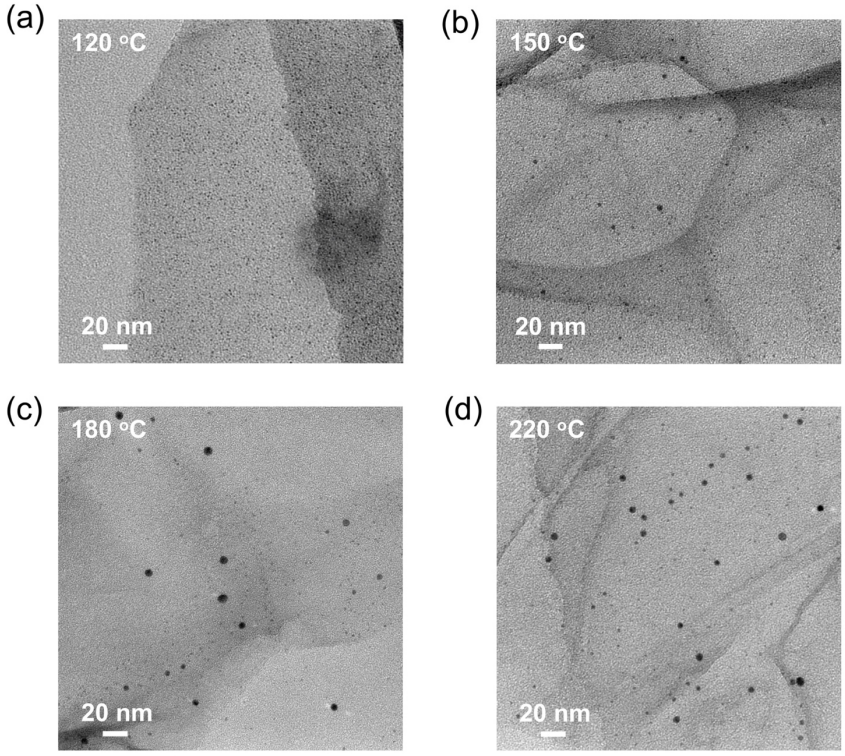

Figure 6-5 Morphology characterizations of Au_{25}/S-G after thermal treatments. TEM images of Au_{25}/S-G annealed at (a) 120, (b) 150, (c) 180, and (d) 220 °C.

6.5 Electrochemical Treatment

In addition to thermal treatment, next we further studied the ligand removal of Au_{25} nanoclusters by electrochemical treatment, which is another commonly used method to remove the capping ligands.[241] The Au_{25}/S-G, which contained 57 μg of Au measured by ICP, was biased in 0.1 M $KHCO_3$ under Ar purging at different potentials from −0.3 to −0.8 V_{RHE}. The extent of ligand removal was also first examined by the Cu UPD test. After biasing at −0.3 V_{RHE}, there was no distinct peak for Au_{25}/S-G in the Cu UPD curve and its surface area was almost zero (Figures 6-6a,b), indicating that this mild condition

was insufficient to strip away the surface ligands. At −0.35 V_{RHE}, a small desorption peak with a surface area of 1 cm^2 showed up (Figure 6-7a). Hence, we propose that −0.35 V_{RHE} could be the critical point for ligand removal during the electrochemistry. Moreover, the Au_{25}/S-G showed a non-negligible peak (surface area = 11 cm^2) at −0.5 V_{RHE} and exhibited an even more remarkable peak (surface area = 25 cm^2) at −0.8 V_{RHE} (Figures 6-6a,b). This implies that the protecting ligands can be removed significantly at negative potentials ≤−0.5 V_{RHE}, exposing abundant Au sites on the surface. It is worth noting that the surface areas under electrochemical biasing are overall larger than those under thermal annealing, which suggests that the electrochemical treatment is a more efficient tool to cleave the ligands from Au_{25} nanoclusters. Besides, the degree of ligand removal was studied by XPS as well. The Au surfaces of pristine and −0.3 V_{RHE} biased Au_{25}/S-G were both in higher oxidation states with higher binding energies (Figure 6-6c), implying that they were still largely covered by the thiolate ligands. Then, from −0.35 to −0.5 and further to −0.8 V_{RHE}, the gradual Au 4*f* XPS peak shift to lower binding energy (Figures 6-6c and 6-7b) suggested that more thiolate ligands got removed under more negative bias and the surface Au atoms became more metallic. Finally, the electrochemical ligand removal on Au_{25} clusters was also investigated by EXAFS. Figure 6-6d illustrates the lower intensity of Au–S coordination at more negative potential (−0.5 and −0.8 V_{RHE}), which proves that more ligands are stripped away resulting from the application of bias.

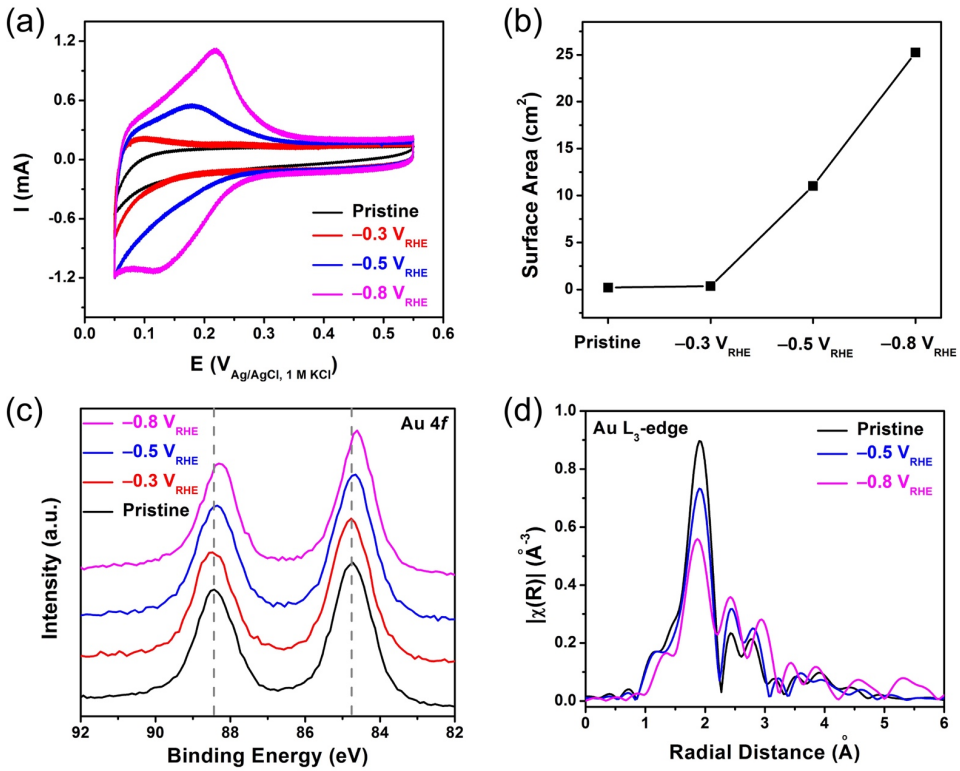

Figure 6-6 Structural characterizations of Au_{25}/S-G after electrochemical treatments. (a) Cu UPD curves, (b) surface areas, (c) Au 4*f* XPS spectra, and (d) Au L_3-edge EXAFS spectra of Au_{25}/S-G biased at different potentials.

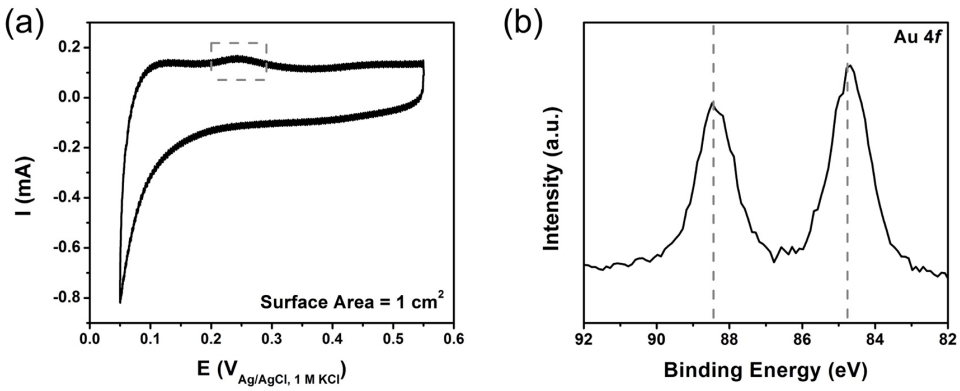

Figure 6-7 Structural characterizations of Au_{25}/S-G biased at –0.35 V_{RHE}. (a) Cu UPD curve and surface area, and (b) Au 4*f* XPS spectrum of Au_{25}/S-G biased at –0.35 V_{RHE}. Gray dashed line in XPS spectrum has the same position as that in Figure 6-6c for comparison.

Although electrochemical treatment is a promising approach for the ligand removal of Au_{25} nanoclusters, similar to thermal treatment, it also induced a concurrent structural change. Cluster sintering was barely seen when the ligands still remained at -0.3 V_{RHE} (Figure 6-8a). At the starting point of ligand removal (-0.35 V_{RHE}), the Au_{25}/S-G exhibited a little agglomeration and formed a few nanoparticles of 2–4 nm (Figure 6-8b). When the ligands were more dominantly stripped away at -0.5 and -0.8 V_{RHE}, more 2–4 nm nanoparticles were observed (Figures 6-8c,d), which were apparently smaller than those found in thermal treatment (Figures 6-5c,d). EXAFS was employed to confirm the structural evolution as well. As the applied potential reduced to -0.5 and -0.8 V_{RHE}, the slight ramping amplitude of Au–Au coordination (Figure 6-6d) suggested more cluster sintering, which was yet obviously smaller than that in thermal annealing (Figure 6-3d). These data collectively imply that the electrochemical treatment could more specifically cleave the Au–S bonds by applying reductive potentials, while the thermal treatment not only breaks the Au–S bonds but also increases the mobility of the entire cluster, leading to significant coalescence. Therefore, the electrochemical biasing is a more desirable way to remove the staple ligands without causing significant aggregation.

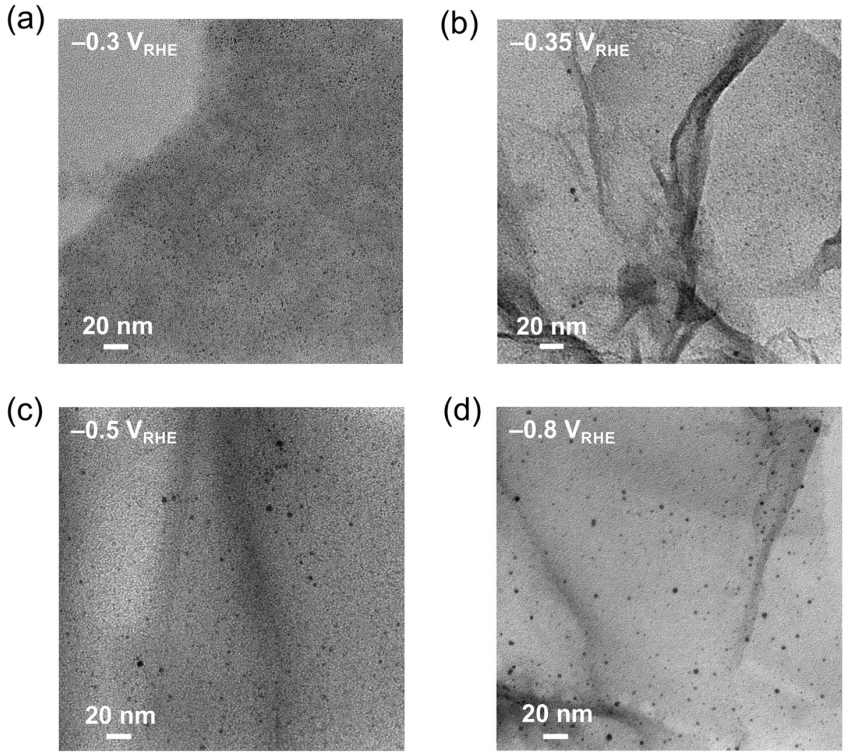

Figure 6-8 Morphology characterizations of Au_{25}/S-G after electrochemical treatments. TEM images of Au_{25}/S-G biased at (a) –0.3, (b) –0.35, (c) –0.5, and (d) –0.8 V_{RHE}.

6.6 CO_2RR Electrocatalytic Properties

Finally, we evaluated the impact of ligand removal on the catalytic properties of Au_{25} nanoclusters for CO_2 electroreduction to CO. The Au_{25}/S-G annealed at 150 °C and that biased at -0.8 V_{RHE} were utilized as thermally and electrochemically treated samples, respectively. The electrochemical CO_2 reduction measurement was conducted in 0.1 M $KHCO_3$ solution under CO_2 flow at a relatively low overpotential between -0.50 and -0.59 V_{RHE}. For all the tests, CO and H_2 were the only gas products detected by GC, and a negligible amount of liquid product was found by ^{1}H NMR spectroscopy (Figure 6-9). Figure 6-10 shows that the Au_{25}/S-G after thermal and electrochemical treatments demonstrated both higher faradaic efficiencies and larger partial current densities (normalized by Au mass loadings) for CO than the pristine catalyst. The CO faradaic efficiencies of thermally and electrochemically treated Au_{25}/S-G at -0.59 V_{RHE} were as high as 64% and 82%; however, it was only 49% for the pristine sample (Figure 6-10a). Meantime, the thermally and electrochemically treated Au_{25}/S-G exhibited 2 and 7 times larger CO partial current densities than their pristine counterpart at -0.59 V_{RHE} (Figure 6-10b). These results jointly suggest that the Au_{25}/S-G after ligand removal showed both improved activity and enhanced selectivity for the electroreduction of CO_2 to CO.

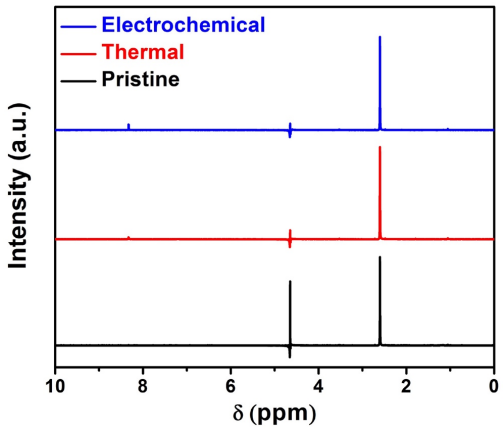

Figure 6-9 CO_2RR liquid products. ^{1}H NMR spectra of liquid products for pristine, thermally treated, and electrochemically treated Au_{25}/S-G after CO_2RR. The peak at 2.60 ppm is DMSO internal standard, and the peak at 4.65 ppm represents water suppression. The small peak at 8.33 ppm is $HCOO^-$, and the tiny peak at 1.06 ppm is C_2H_5OH. The faradaic efficiencies for all liquid products are <3%.

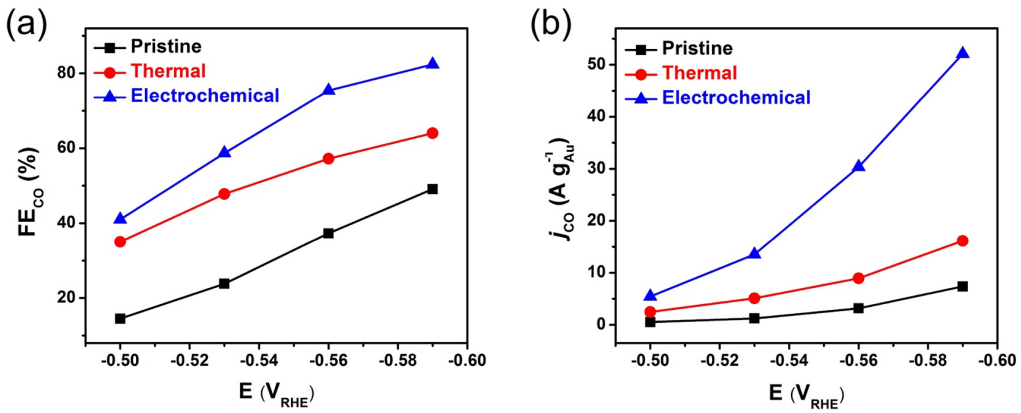

Figure 6-10 CO_2RR electrocatalytic properties of Au_{25}/S-G after different treatments. (a) Faradaic efficiencies (FE) and (b) partial current densities (*j*, normalized by Au mass loadings) for CO of pristine, thermally treated, and electrochemically treated Au_{25}/S-G.

The post-measurement characterizations reveal that although the Au_{25} nanoclusters did further evolve slightly after CO_2 electrocatalysis (Figure 6-11), the surface areas still followed the order of electrochemically treated Au_{25}/S-G > thermally treated Au_{25}/S-G > pristine Au_{25}/S-G (Figure 6-12), which was the same as the pre-reaction trend. Hence, we can conclude that the catalytic improvements of Au_{25}/S-G after thermal and electrochemical treatments can be attributed to the exposure of undercoordinated Au sites on the surface after ligand removal, which favor the production of CO over H_2. It is worth noting that the electrochemical biasing offered a better performance for CO_2-to-CO electro-conversion than the thermal annealing (Figure 6-10), which was again due to the higher surface area of exposed Au sites upon surface ligand removal (Figure 6-12). Aside from active surface area, other properties, including coordination environment and

electronic structure, may also affect the catalytic behavior of Au clusters, which needs further exploration.[111,233] Finally, the Au_{25}/S-G after different treatments also exhibited good stability over the course of long-term CO_2 electrocatalysis (Figure 6-13).

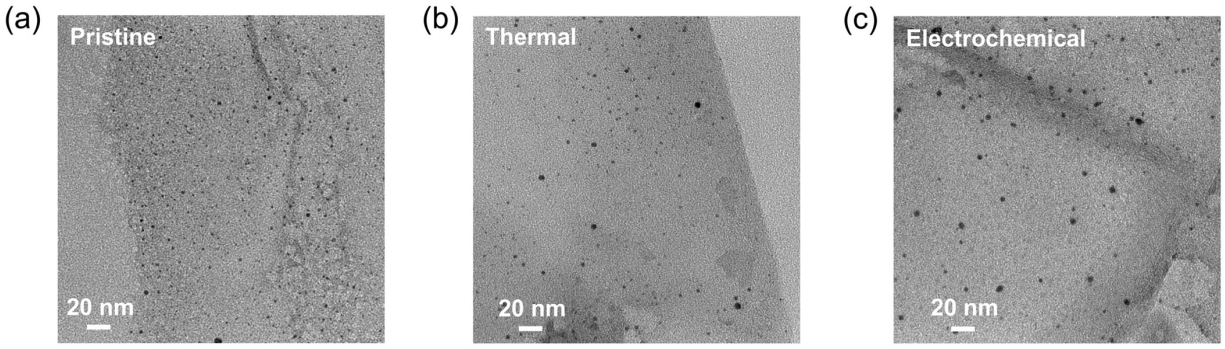

Figure 6-11 Morphology characterizations of different Au_{25}/S-G after CO_2RR. TEM images of (a) pristine, (b) thermally treated, and (c) electrochemically treated Au_{25}/S-G after CO_2RR.

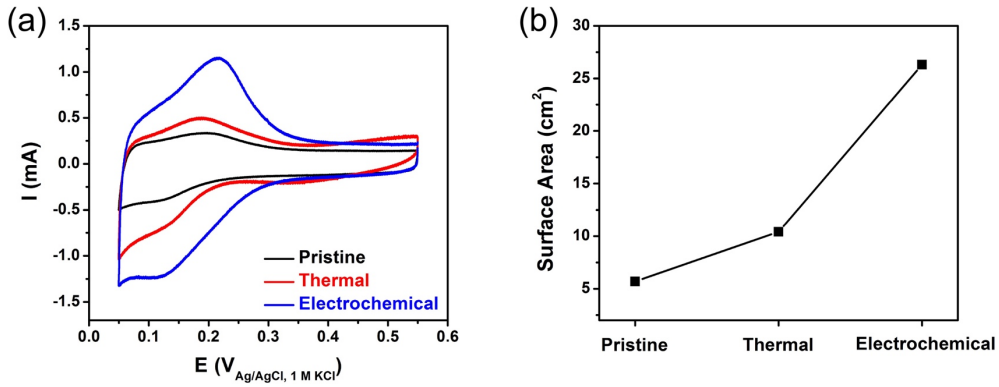

Figure 6-12 Surface characterizations of different Au_{25}/S-G after CO_2RR. (a) Cu UPD curves and (b) surface areas of pristine, thermally treated, and electrochemically treated Au_{25}/S-G after CO_2RR.

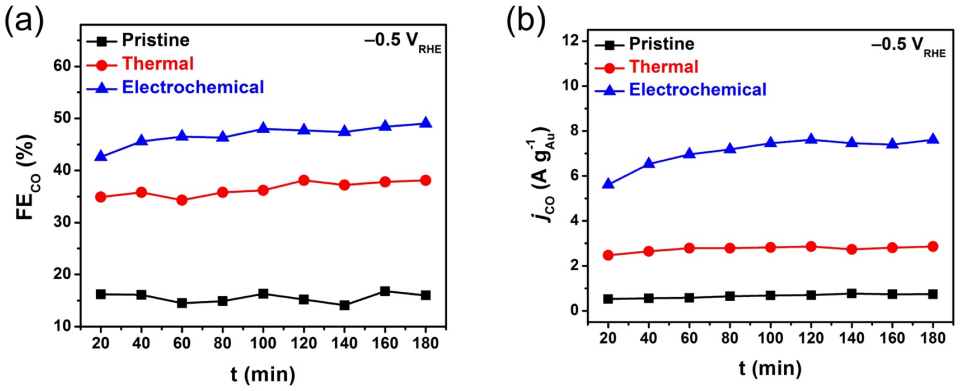

Figure 6-13 Stability of different Au_{25}/S-G under long-term CO_2RR. (a) Faradaic efficiencies (FE) and (b) partial current densities (*j*, normalized by Au mass loadings) for CO of pristine, thermally treated, and electrochemically treated Au_{25}/S-G at –0.5 V_{RHE} for 3 h.

6.7 Conclusions

In conclusion, we have successfully synthesized pure $Au_{25}(PET)_{18}$ nanoclusters and anchored them on sulfur-doped graphene. The capping ligands could be significantly stripped away by both thermal annealing (≥180 °C) and electrochemical biasing (≤ −0.5 V_{RHE}). The degree of ligand removal was investigated by a combination of techniques including Cu UPD, XPS, and EXAFS. However, it was also noted that the aggressive thermal and electrochemical conditions inevitably induced the structural transformation of Au_{25} nanoclusters at the same time. The Au_{25} nanoclusters after ligand-removing treatments were both more active and more selective for CO_2 electroreduction to CO than the pristine counterpart, which was contributed by the increased exposure of catalytically active surface Au sites associated with the removal of thiolate ligands. These findings could serve as a guideline on how to effectively remove the protecting ligands from undercoordinated metal nanoclusters to obtain superior catalytic properties.

6.8 Methods

Synthesis and purification of neutral Au_{25} nanoclusters. Pure and charge-neutral $Au_{25}(PET)_{18}$ nanoclusters were prepared via a modified method from the literature.[237] 197 mg of $HAuCl_4 \cdot 3H_2O$ and 328 mg of tetraoctylammonium bromide (TOAB) were dissolved in 50 mL of tetrahydrofuran (THF). The mixture was stirred at 500 rpm for 15 min to form a dark red solution before the addition of 345 mg of PET. When the solution became transparent after 30 min, 189 mg of $NaBH_4$ dissolved in 10 mL of ice-cold water was added. The reaction was kept at room temperature under stirring (500 rpm) for 24 h. The crude sample was washed with ice-cold water and methanol to remove the unreacted precursors and free TOAB. The as-obtained products were passed through a silica column and a size-exclusion column subsequently to yield pure and neutrally charged $Au_{25}(PET)_{18}$ nanoclusters (abbreviated as Au_{25} nanoclusters).

Loading of Au_{25} nanoclusters on S-G. The Au_{25} nanoclusters with 57 μg of Au, as determined by ICP, were dispersed in 1 mL of toluene and added to 1 mg of S-G. The mixture was stirred at 500 rpm for 1 h at room temperature to complete the loading process. The dispersion was blow-dried by N_2 to obtain Au_{25}/S-G. The Au_{25}/S-G used for all the treatments and measurements in this work had 57 μg of Au and 1 mg of S-G.

Thermal treatment of Au_{25}/S-G. The Au_{25}/S-G powder was annealed in a 10% H_2/Ar gas atmosphere at different temperatures for 30 min. The sample was heated up with a ramping rate of 3 °C min^{-1} and cooled down naturally.

Working electrode preparation of Au_{25}/S-G for electrochemical characterizations. The Au_{25}/S-G was dispersed in 0.6 mL of ethanol and 30 μL of Nafion 117 solution. The sample was drop-casted onto either a glassy carbon with a diameter of 1.25 cm for electrochemical treatment and Cu UPD measurement, or a carbon paper with a geometric area of 1 cm^2 for electrochemical CO_2 reduction measurement. The electrodes were dried under vacuum before use.

Electrochemical treatment of Au_{25}/S-G. Ag/AgCl, 1 M KCl and carbon paper were used as the reference and counter electrodes, respectively, and 0.1 M $KHCO_3$ prepared from K_2CO_3 saturated with CO_2 was used as the electrolyte. The potentials were presented versus the RHE and corrected for ohmic iR drop. CA at different potentials were applied under Ar purging for 30 min.

Cu UPD measurement. The reference electrode was Ag/AgCl, 1 M KCl and the counter electrode was carbon paper. The electrolyte was 0.1 M $CuSO_4$ and 0.5 M H_2SO_4. CV was conducted from 0.55 to 0.05 V versus Ag/AgCl, 1 M KCl under Ar purging at a sweep rate of 50 mV s^{-1}. The electrochemical surface area was calculated by integrating the anodic stripping peak associated with the desorption using a conversion factor of 92.4 μC cm^{-2}.[240]

Electrochemical measurement for CO_2 reduction. Electrochemical measurements were carried out in our customized H-cell setup, which had two compartments separated by an anion-exchange membrane (Selemion AMV). Ag/AgCl, 3 M KCl was used as the reference electrode, and Pt wire was employed as the counter electrode. 0.1 M $KHCO_3$ prepared from K_2CO_3 saturated with CO_2 (pH = 6.8) was used as the electrolyte. The working and counter electrode compartments each held 15 mL of electrolyte. During the electrocatalysis, CO_2 flowed through the working compartment at a rate of 20 sccm. For the electrochemical testing, CA at different potentials were applied. Electrode potentials were converted to the RHE scale using E (versus RHE) = E (versus Ag/AgCl, 3 M KCl) + 0.210 V + 0.0591 × pH. 84% of ohmic loss was compensated by Biologic potentiostat during the measurement while the remaining 16% was manually post-corrected. The gas products were measured by a GC (SRI) equipped with a flame ionization detector and a thermal conductivity detector, and the liquid products were quantified by ^1H NMR spectroscopy with water suppression, using dimethyl sulfoxide (DMSO) as an internal standard. Faradaic efficiencies (FE) were calculated by dividing the amount of charge consumed for each product by the total charge passed, followed by normalization.

Chapter. 7 Summary and Outlook

As a summary, this dissertation describes the utilization of various strategies, including catalyst processing, controlled synthesis, adding a second material, achieving long-range ordering, and ligand removal, to enhance the catalytic properties of different materials, containing Pt-based nanoframes, Cu−Au nanowires, and Au_{25} nanoclusters, for multiple energy-related reactions, such as ORR and CO_2RR. All of these works could serve as a general guideline on how to achieve desired catalytic performance for renewable energy conversion through rational design.

In Chapter 2, we report the effect of catalyst processing on the ORR properties of Pt−Ni nanoframes. The corrosion procedure not only defined the starting Ni content (and, thus, the initial activity) but also decided the magnitude of electrochemical Ni dissolution (and, thus, the stability). As a consequence, electrochemical corrosion led to the highest initial specific activity by retaining more Ni in the catalysts, while nitric acid corrosion achieved the best durability by imparting a less-defective surface.

In Chapter 3, we demonstrate the controlled synthesis of Pt−Co nanoframes with both open morphology and active composition for fuel-cell electrocatalysis. The as-prepared Pt–Co nanoframes exhibited remarkable activity and stability for both ORR and MOR in either acidic or alkaline electrolyte. The improved activity was because of the optimized binding energies of reaction intermediates, and the enhanced stability was owing to the negligible electrochemical dissolution of Co.

In Chapter 4, we present the addition of a second material (ZIF-8) to Pt−Ni nanoframe to synthesize the individually encapsulated frame-in-frame structure. Using the surface functionalization, both the single core−shell and the single yolk−shell structures were prepared. The growth trajectory was tracked, in which the one-nanoframe-to-one-ZIF-8 attachment resulted in the one-in-one hybrid formation. The obtained frame-in-frame composites are promising candidates for size-selective or tandem catalysis to produce fine chemicals.

In Chapter 5, we exhibit the shape-preserved ordering of Cu@Au core−shell nanowires into Cu_3Au intermetallic nanowires. Thermally-driven atomic diffusion accounted for the transformation process and was facilitated by the abundant twin planar defects. These fully ordered Cu_3Au nanowires had uniform and precise atomic positioning in the crystal lattice, as well as enhanced thermal stability in air. The resultant Cu_3Au intermetallic nanowires have potential electrocatalytic applications for ORR and CO_2RR.

In Chapter 6, we investigate the ligand removal of Au_{25} nanoclusters and its impact on CO_2RR. The thiolate ligands could be significantly stripped away under either thermal annealing at $\geq$180 °C or electrochemical biasing at ≤ -0.5 V_{RHE}. The Au_{25} clusters after ligand-removing treatments were more active and selective for the CO_2 electroreduction to CO than the pristine counterpart, which was contributed by the increased exposure of catalytically active Au sites on the surface after ligand removal.

Two major directions should be taken into consideration for future nanocatalyst design. The first one is controlled synthesis, in which the metal precursors, reaction temperature, solvent, ligand, etc. could be tuned. The second one is post-synthesis treatment, in which the corrosion, thermal treatment, electrochemical treatment, adding other materials, etc. could be applied. The ultimate goal is to prepare the nanocatalysts with desired shape, surface configuration, composition, elemental distribution, crystalline structure, etc. to promote the chemical reactions of interest.

To accomplish the rational design of nanocatalysts, in situ or operando characterizations are important techniques. It is essential to probe the catalyst structure, such as oxidation state, coordination environment, morphology, atomic arrangement, etc., under real-time reaction conditions and correlate it with the catalytic property. Such structure−property relationship can largely advance the development of next-generation nanocatalysts and needs to be carefully investigated.

References

1. Dresselhaus, M. S.; Thomas, I. L., Alternative Energy Technologies. *Nature* **2001,** *414* (6861), 332−337.
2. Lewis, N. S.; Nocera, D. G., Powering the Planet: Chemical Challenges in Solar Energy Utilization. *Proc. Natl. Acad. Sci. U. S. A.* **2006,** *103* (43), 15729−15735.
3. Chu, S.; Cui, Y.; Liu, N., The Path towards Sustainable Energy. *Nat. Mater.* **2016,** *16* (1), 16−22.
4. Our World in Data. ourworldindata.org. Accessed 2021.
5. Keeling, C. D.; Whorf, T. P.; Wahlen, M.; Vanderplicht, J., Interannual Extremes in the Rate of Rise of Atmospheric Carbon-Dioxide since 1980. *Nature* **1995,** *375* (6533), 666−670.
6. Cox, P. M.; Betts, R. A.; Jones, C. D.; Spall, S. A.; Totterdell, I. J., Acceleration of Global Warming due to Carbon-Cycle Feedbacks in a Coupled Climate Model. *Nature* **2000,** *408* (6809), 184−187.
7. Pattyn, F.; Ritz, C.; Hanna, E.; Asay-Davis, X.; DeConto, R.; Durand, G.; Favier, L.; Fettweis, X.; Goelzer, H.; Golledge, N. R.; Kuipers Munneke, P.; Lenaerts, J. T. M.; Nowicki, S.; Payne, A. J.; Robinson, A.; Seroussi, H.; Trusel, L. D.; van den Broeke, M., The Greenland and Antarctic Ice Sheets under 1.5 °C Global Warming. *Nat. Clim. Chang.* **2018,** *8* (12), 1053−1061.
8. Goddard, P. B.; Yin, J.; Griffies, S. M.; Zhang, S., An Extreme Event of Sea-Level Rise along the Northeast Coast of North America in 2009−2010. *Nat. Commun.* **2015,** *6*, 6346.
9. Hoegh-Guldberg, O.; Mumby, P. J.; Hooten, A. J.; Steneck, R. S.; Greenfield, P.; Gomez, E.; Harvell, C. D.; Sale, P. F.; Edwards, A. J.; Caldeira, K.; Knowlton, N.; Eakin, C. M.; Iglesias-Prieto, R.; Muthiga, N.; Bradbury, R. H.; Dubi, A.; Hatziolos, M. E., Coral Reefs under Rapid Climate Change and Ocean Acidification. *Science* **2007,** *318* (5857), 1737−1742.
10. Kroeker, K. J.; Kordas, R. L.; Crim, R.; Hendriks, I. E.; Ramajo, L.; Singh, G. S.; Duarte, C. M.; Gattuso, J. P., Impacts of Ocean Acidification on Marine Organisms: Quantifying Sensitivities and Interaction with Warming. *Glob. Chang. Biol.* **2013,** *19* (6), 1884−1896.
11. Parmesan, C.; Yohe, G., A Globally Coherent Fingerprint of Climate Change Impacts across Natural Systems. *Nature* **2003,** *421* (6918), 37−42.
12. Parmesan, C., Ecological and Evolutionary Responses to Recent Climate Change. *Annu. Rev. Ecol. Evol. Syst.* **2006,** *37* (1), 637−669.
13. Diaz, D.; Moore, F., Quantifying the Economic Risks of Climate Change. *Nat. Clim. Chang.* **2017,** *7* (11), 774−782.

14. Berner, R. A., The Long-Term Carbon Cycle, Fossil Fuels and Atmospheric Composition. *Nature* **2003,** *426* (6964), 323−326.
15. Le Quéré, C.; Raupach, M. R.; Canadell, J. G.; Marland, G.; Bopp, L.; Ciais, P.; Conway, T. J.; Doney, S. C.; Feely, R. A.; Foster, P.; Friedlingstein, P.; Gurney, K.; Houghton, R. A.; House, J. I.; Huntingford, C.; Levy, P. E.; Lomas, M. R.; Majkut, J.; Metzl, N.; Ometto, J. P.; Peters, G. P.; Prentice, I. C.; Randerson, J. T.; Running, S. W.; Sarmiento, J. L.; Schuster, U.; Sitch, S.; Takahashi, T.; Viovy, N.; van der Werf, G. R.; Woodward, F. I., Trends in the Sources and Sinks of Carbon Dioxide. *Nat. Geosci.* **2009,** *2* (12), 831−836.
16. Jiao, K.; Xuan, J.; Du, Q.; Bao, Z.; Xie, B.; Wang, B.; Zhao, Y.; Fan, L.; Wang, H.; Hou, Z.; Huo, S.; Brandon, N. P.; Yin, Y.; Guiver, M. D., Designing the Next Generation of Proton-Exchange Membrane Fuel Cells. *Nature* **2021,** *595* (7867), 361−369.
17. Electrocatalysis for the Generation and Consumption of Fuels. *Nat. Rev. Chem.* **2018,** *2* (4), 1−3.
18. Xie, C. L.; Niu, Z. Q.; Kim, D.; Li, M. F.; Yang, P. D., Surface and Interface Control in Nanoparticle Catalysis. *Chem. Rev.* **2020,** *120* (2), 1184−1249.
19. Stamenkovic, V. R.; Strmcnik, D.; Lopes, P. P.; Markovic, N. M., Energy and Fuels from Electrochemical Interfaces. *Nat. Mater.* **2017,** *16* (1), 57−69.
20. Seh, Z. W.; Kibsgaard, J.; Dickens, C. F.; Chorkendorff, I. B.; Norskov, J. K.; Jaramillo, T. F., Combining Theory and Experiment in Electrocatalysis: Insights into Materials Design. *Science* **2017,** *355* (6321), eaad4998.
21. Debe, M. K., Electrocatalyst Approaches and Challenges for Automotive Fuel Cells. *Nature* **2012,** *486* (7401), 43−51.
22. Steele, B. C. H.; Heinzel, A., Materials for Fuel-Cell Technologies. *Nature* **2001,** *414* (6861), 345−352.
23. Gasteiger, H. A.; Markovic, N. M., Just a Dream-or Future Reality? *Science* **2009,** *324* (5923), 48−49.
24. Rossmeisl, J.; Karlberg, G. S.; Jaramillo, T.; Norskov, J. K., Steady State Oxygen Reduction and Cyclic Voltammetry. *Faraday Discuss.* **2008,** *140*, 337−346.
25. Li, J. R.; Sharma, S.; Liu, X. M.; Pan, Y. T.; Spendelow, J. S.; Chi, M. F.; Jia, Y. K.; Zhang, P.; Cullen, D. A.; Xi, Z.; Lin, H. H.; Yin, Z. Y.; Shen, B.; Muzzio, M.; Yu, C.; Kim, Y. S.; Peterson, A. A.; More, K. L.; Zhu, H. Y.; Sun, S. H., Hard-Magnet L1(0)-CoPt Nanoparticles Advance Fuel Cell Catalysis. *Joule* **2019,** *3* (1), 124−135.
26. Greeley, J., Theoretical Heterogeneous Catalysis: Scaling Relationships and Computational Catalyst Design. *Annu. Rev. Chem. Biomol. Eng.* **2016,** *7*, 605−635.
27. Viswanathan, V.; Hansen, H. A.; Rossmeisl, J.; Norskov, J. K., Universality in Oxygen Reduction Electrocatalysis on Metal Surfaces. *ACS Catal.* **2012,** *2* (8), 1654−1660.

28. Norskov, J. K.; Rossmeisl, J.; Logadottir, A.; Lindqvist, L.; Kitchin, J. R.; Bligaard, T.; Jonsson, H., Origin of the Overpotential for Oxygen Reduction at a Fuel-Cell Cathode. *J. Phys. Chem. B* **2004,** *108* (46), 17886−17892.
29. Gasteiger, H. A.; Kocha, S. S.; Sompalli, B.; Wagner, F. T., Activity Benchmarks and Requirements for Pt, Pt-alloy, and Non-Pt Oxygen Reduction Catalysts for PEMFCs. *Appl. Catal. B* **2005,** *56* (1−2), 9−35.
30. Stamenkovic, V. R.; Mun, B. S.; Arenz, M.; Mayrhofer, K. J. J.; Lucas, C. A.; Wang, G. F.; Ross, P. N.; Markovic, N. M., Trends in Electrocatalysis on Extended and Nanoscale Pt-Bimetallic Alloy Surfaces. *Nat. Mater.* **2007,** *6* (3), 241−247.
31. Greeley, J.; Stephens, I. E. L.; Bondarenko, A. S.; Johansson, T. P.; Hansen, H. A.; Jaramillo, T. F.; Rossmeisl, J.; Chorkendorff, I.; Norskov, J. K., Alloys of Platinum and Early Transition Metals as Oxygen Reduction Electrocatalysts. *Nat. Chem.* **2009,** *1* (7), 552−556.
32. Hammer, B.; Norskov, J. K., Theoretical Surface Science and Catalysis−Calculations and Concepts. *Adv. Catal.* **2000,** *45*, 71−129.
33. Kitchin, J. R.; Norskov, J. K.; Barteau, M. A.; Chen, J. G., Modification of the Surface Electronic and Chemical Properties of Pt(111) by Subsurface 3d Transition Metals. *J. Chem. Phys.* **2004,** *120* (21), 10240−10246.
34. Hammer, B.; Norskov, J. K., Why Gold Is the Noblest of All the Metals. *Nature* **1995,** *376* (6537), 238−240.
35. Tian, X. L.; Zhao, X.; Su, Y. Q.; Wang, L. J.; Wang, H. M.; Dang, D.; Chi, B.; Liu, H. F.; Hensen, E. J. M.; Lou, X. W.; Xia, B. Y., Engineering Bunched Pt−Ni Alloy Nanocages for Efficient Oxygen Reduction in Practical Fuel Cells. *Science* **2019,** *366* (6467), 850−856.
36. Gan, L.; Heggen, M.; Rudi, S.; Strasser, P., Core−Shell Compositional Fine Structures of Dealloyed PtxNi1-x Nanoparticles and Their Impact on Oxygen Reduction Catalysis. *Nano Lett.* **2012,** *12* (10), 5423−5430.
37. Wang, H. T.; Xu, S. C.; Tsai, C.; Li, Y. Z.; Liu, C.; Zhao, J.; Liu, Y. Y.; Yuan, H. Y.; Abild-Pedersen, F.; Prinz, F. B.; Norskov, J. K.; Cui, Y., Direct and Continuous Strain Control of Catalysts with Tunable Battery Electrode Materials. *Science* **2016,** *354* (6315), 1031−1036.
38. Strasser, P.; Koh, S.; Anniyev, T.; Greeley, J.; More, K.; Yu, C. F.; Liu, Z. C.; Kaya, S.; Nordlund, D.; Ogasawara, H.; Toney, M. F.; Nilsson, A., Lattice-Strain Control of the Activity in Dealloyed Core−Shell Fuel Cell Catalysts. *Nat. Chem.* **2010,** *2* (6), 454−460.
39. Gan, L.; Rudi, S.; Cui, C.; Heggen, M.; Strasser, P., Size-Controlled Synthesis of Sub-10 nm PtNi3 Alloy Nanoparticles and Their Unusual Volcano-Shaped Size Effect on ORR Electrocatalysis. *Small* **2016,** *12* (23), 3189−3196.

40. Shao, M.; Peles, A.; Shoemaker, K., Electrocatalysis on Platinum Nanoparticles: Particle Size Effect on Oxygen Reduction Reaction Activity. *Nano Lett.* **2011,** *11* (9), 3714−3719.
41. Jiang, K. Z.; Zhao, D. D.; Guo, S. J.; Zhang, X.; Zhu, X.; Guo, J.; Lu, G.; Huang, X. Q., Efficient Oxygen Reduction Catalysis by Subnanometer Pt Alloy Nanowires. *Sci. Adv.* **2017,** *3* (2), e1601705.
42. Bu, L. Z.; Zhang, N.; Guo, S. J.; Zhang, X.; Li, J.; Yao, J. L.; Wu, T.; Lu, G.; Ma, J. Y.; Su, D.; Huang, X. Q., Biaxially Strained PtPb/Pt Core/Shell Nanoplate Boosts Oxygen Reduction Catalysis. *Science* **2016,** *354* (6318), 1410−1414.
43. Cui, C. H.; Gan, L.; Heggen, M.; Rudi, S.; Strasser, P., Compositional Segregation in Shaped Pt Alloy Nanoparticles and Their Structural Behaviour during Electrocatalysis. *Nat. Mater.* **2013,** *12* (8), 765−771.
44. Zhang, L.; Roling, L. T.; Wang, X.; Vara, M.; Chi, M. F.; Liu, J. Y.; Choi, S. I.; Park, J.; Herron, J. A.; Xie, Z. X.; Mavrikakis, M.; Xia, Y. N., Platinum-Based Nanocages with Subnanometer-Thick Walls and Well-Defined, Controllable Facets. *Science* **2015,** *349* (6246), 412−416.
45. Chen, C.; Kang, Y. J.; Huo, Z. Y.; Zhu, Z. W.; Huang, W. Y.; Xin, H. L. L.; Snyder, J. D.; Li, D. G.; Herron, J. A.; Mavrikakis, M.; Chi, M. F.; More, K. L.; Li, Y. D.; Markovic, N. M.; Somorjai, G. A.; Yang, P. D.; Stamenkovic, V. R., Highly Crystalline Multimetallic Nanoframes with Three-Dimensional Electrocatalytic Surfaces. *Science* **2014,** *343* (6177), 1339−1343.
46. Wang, C.; Chi, M. F.; Li, D. G.; van der Vliet, D.; Wang, G. F.; Lin, Q. Y.; Mitchell, J. F.; More, K. L.; Markovic, N. M.; Stamenkovic, V. R., Synthesis of Homogeneous Pt-Bimetallic Nanoparticles as Highly Efficient Electrocatalysts. *ACS Catal.* **2011,** *1* (10), 1355−1359.
47. Wang, C.; Chi, M. F.; Wang, G. F.; van der Vliet, D.; Li, D. G.; More, K.; Wang, H. H.; Schlueter, J. A.; Markovic, N. M.; Stamenkovic, V. R., Correlation Between Surface Chemistry and Electrocatalytic Properties of Monodisperse PtxNi1-x Nanoparticles. *Adv. Funct. Mater.* **2011,** *21* (1), 147−152.
48. Meier, J. C.; Galeano, C.; Katsounaros, I.; Witte, J.; Bongard, H. J.; Topalov, A. A.; Baldizzone, C.; Mezzavilla, S.; Schuth, F.; Mayrhofer, K. J. J., Design Criteria for Stable Pt/C Fuel Cell Catalysts. *Beilstein J. Nanotechnol.* **2014,** *5*, 44−67.
49. Li, Y. W.; Hart, J. L.; Taheri, M. L.; Snyder, J. D., Morphological Instability in Topologically Complex, Three-Dimensional Electrocatalytic Nanostructures. *ACS Catal.* **2017,** *7* (11), 7995−8005.
50. Nagasawa, K.; Takao, S.; Higashi, K.; Nagamatsu, S.; Samjeske, G.; Imaizumi, Y.; Sekizawa, O.; Yamamoto, T.; Uruga, T.; Iwasawa, Y., Performance and Durability of Pt/C Cathode Catalysts with Different Kinds of Carbons for Polymer Electrolyte Fuel Cells

Characterized by Electrochemical and in Situ XAFS Techniques. *Phys. Chem. Chem. Phys.* **2014,** *16* (21), 10075−10087.
51. Shinozaki, K.; Zack, J. W.; Richards, R. M.; Pivovar, B. S.; Kocha, S. S., Oxygen Reduction Reaction Measurements on Platinum Electrocatalysts Utilizing Rotating Disk Electrode Technique I. Impact of Impurities, Measurement Protocols and Applied Corrections. *J. Electrochem. Soc.* **2015,** *162* (10), F1144−F1158.
52. Shinozaki, K.; Zack, J. W.; Pylypenko, S.; Pivovar, B. S.; Kocha, S. S., Oxygen Reduction Reaction Measurements on Platinum Electrocatalysts Utilizing Rotating Disk Electrode Technique II. Influence of Ink Formulation, Catalyst Layer Uniformity and Thickness. *J. Electrochem. Soc.* **2015,** *162* (12), F1384−F1396.
53. Garsany, Y.; Ge, J. J.; St-Pierre, J.; Rocheleau, R.; Swider-Lyons, K. E., Analytical Procedure for Accurate Comparison of Rotating Disk Electrode Results for the Oxygen Reduction Activity of Pt/C. *J. Electrochem. Soc.* **2014,** *161* (5), F628−F640.
54. Markovic, N. M.; Adzic, R. R.; Cahan, B. D.; Yeager, E. B., Structural Effects in Electrocatalysis: Oxygen Reduction on Platinum Low Index Single-Crystal Surfaces in Perchloric Acid Solutions. *J. Electroanal. Chem.* **1994,** *377* (1−2), 249−259.
55. Markovic, N. M.; Gasteiger, H. A.; Ross, P. N., Oxygen Reduction on Platinum Low-Index Single-Crystal Surfaces in Sulfuric Acid Solution: Rotating Ring−Pt(hkl) Disk Studies. *J. Phys. Chem.* **1995,** *99* (11), 3411−3415.
56. Markovic, N. M.; Gasteiger, H. A.; Philip, N., Oxygen Reduction on Platinum Low-Index Single-Crystal Surfaces in Alkaline Solution: Rotating Ring Disk Pt(hkl) Studies. *J. Phys. Chem.* **1996,** *100* (16), 6715−6721.
57. Garsany, Y.; Baturina, O. A.; Swider-Lyons, K. E.; Kocha, S. S., Experimental Methods for Quantifying the Activity of Platinum Electrocatalysts for the Oxygen Reduction Reaction. *Anal. Chem.* **2010,** *82* (15), 6321−6328.
58. Mayrhofer, K. J. J.; Strmcnik, D.; Blizanac, B. B.; Stamenkovic, V.; Arenz, M.; Markovic, N. M., Measurement of Oxygen Reduction Activities via the Rotating Disc Electrode Method: From Pt Model Surfaces to Carbon-Supported High Surface Area Catalysts. *Electrochim. Acta* **2008,** *53* (7), 3181−3188.
59. Nitopi, S.; Bertheussen, E.; Scott, S. B.; Liu, X. Y.; Engstfeld, A. K.; Horch, S.; Seger, B.; Stephens, I. E. L.; Chan, K.; Hahn, C.; Norskov, J. K.; Jaramillo, T. F.; Chorkendorff, I., Progress and Perspectives of Electrochemical CO2 Reduction on Copper in Aqueous Electrolyte. *Chem. Rev.* **2019,** *119* (12), 7610−7672.
60. Hori, Y.; Wakebe, H.; Tsukamoto, T.; Koga, O., Electrocatalytic Process of CO Selectivity in Electrochemical Reduction of CO2 at Metal Electrodes in Aqueous Media. *Electrochim. Acta* **1994,** *39* (11−12), 1833−1839.
61. Kortlever, R.; Shen, J.; Schouten, K. J.; Calle-Vallejo, F.; Koper, M. T., Catalysts and Reaction Pathways for the Electrochemical Reduction of Carbon Dioxide. *J. Phys. Chem. Lett.* **2015,** *6* (20), 4073−4082.

62. Feaster, J. T.; Shi, C.; Cave, E. R.; Hatsukade, T.; Abram, D. N.; Kuhl, K. P.; Hahn, C.; Nørskov, J. K.; Jaramillo, T. F., Understanding Selectivity for the Electrochemical Reduction of Carbon Dioxide to Formic Acid and Carbon Monoxide on Metal Electrodes. *ACS Catal.* **2017,** *7* (7), 4822−4827.
63. Yoo, J. S.; Christensen, R.; Vegge, T.; Norskov, J. K.; Studt, F., Theoretical Insight into the Trends That Guide the Electrochemical Reduction of Carbon Dioxide to Formic Acid. *ChemSusChem* **2016,** *9* (4), 358−363.
64. Wang, L.; Nitopi, S. A.; Bertheussen, E.; Orazov, M.; Morales-Guio, C. G.; Liu, X.; Higgins, D. C.; Chan, K.; Nørskov, J. K.; Hahn, C.; Jaramillo, T. F., Electrochemical Carbon Monoxide Reduction on Polycrystalline Copper: Effects of Potential, Pressure, and pH on Selectivity toward Multicarbon and Oxygenated Products. *ACS Catal.* **2018,** *8* (8), 7445−7454.
65. Nie, X.; Esopi, M. R.; Janik, M. J.; Asthagiri, A., Selectivity of CO2 Reduction on Copper Electrodes: The Role of the Kinetics of Elementary Steps. *Angew. Chem., Int. Ed.* **2013,** *52* (9), 2459−2462.
66. Peterson, A. A.; Abild-Pedersen, F.; Studt, F.; Rossmeisl, J.; Nørskov, J. K., How Copper Catalyzes the Electroreduction of Carbon Dioxide into Hydrocarbon Fuels. *Energy Environ. Sci.* **2010,** *3* (9), 1311−1315.
67. Montoya, J. H.; Shi, C.; Chan, K.; Norskov, J. K., Theoretical Insights into a CO Dimerization Mechanism in CO2 Electroreduction. *J. Phys. Chem. Lett.* **2015,** *6* (11), 2032−2037.
68. Goodpaster, J. D.; Bell, A. T.; Head-Gordon, M., Identification of Possible Pathways for C−C Bond Formation during Electrochemical Reduction of CO2: New Theoretical Insights from an Improved Electrochemical Model. *J. Phys. Chem. Lett.* **2016,** *7* (8), 1471−1477.
69. Hori, Y.; Takahashi, R.; Yoshinami, Y.; Murata, A., Electrochemical Reduction of CO at a Copper Electrode. *J. Phys. Chem. B* **1997,** *101* (36), 7075−7081.
70. Ma, S.; Sadakiyo, M.; Luo, R.; Heima, M.; Yamauchi, M.; Kenis, P. J. A., One-Step Electrosynthesis of Ethylene and Ethanol from CO2 in an Alkaline Electrolyzer. *J. Power Sources* **2016,** *301*, 219−228.
71. Handoko, A. D.; Chan, K. W.; Yeo, B. S., –CH3 Mediated Pathway for the Electroreduction of CO2 to Ethane and Ethanol on Thick Oxide-Derived Copper Catalysts at Low Overpotentials. *ACS Energy Lett.* **2017,** *2* (9), 2103−2109.
72. Kibria Nabil, S.; McCoy, S.; Kibria, M. G., Comparative Life Cycle Assessment of Electrochemical Upgrading of CO2 to Fuels and Feedstocks. *Green Chem.* **2021,** *23* (2), 867−880.
73. Xu, H. P.; Rebollar, D.; He, H. Y.; Chong, L. N.; Liu, Y. Z.; Liu, C.; Sun, C. J.; Li, T.; Muntean, J. V.; Winans, R. E.; Liu, D. J.; Xu, T., Highly Selective Electrocatalytic CO2

Reduction to Ethanol by Metallic Clusters Dynamically Formed from Atomically Dispersed Copper. *Nat. Energy* **2020,** *5* (8), 623−632.
74. Wang, X.; Wang, Z. Y.; de Arquer, F. P. G.; Dinh, C. T.; Ozden, A.; Li, Y. G. C.; Nam, D. H.; Li, J.; Liu, Y. S.; Wicks, J.; Chen, Z. T.; Chi, M. F.; Chen, B.; Wang, Y.; Tam, J.; Howe, J. Y.; Proppe, A.; Todorovic, P.; Li, F. W.; Zhuang, T. T.; Gabardo, C. M.; Kirmani, A. R.; McCallum, C.; Hung, S. F.; Lum, Y. W.; Luo, M. C.; Min, Y. M.; Xu, A. N.; O'Brien, C. P.; Stephen, B.; Sun, B.; Ip, A. H.; Richter, L. J.; Kelley, S. O.; Sinton, D.; Sargent, E. H., Efficient Electrically Powered CO2-to-Ethanol via Suppression of Deoxygenation. *Nat. Energy* **2020,** *5* (6), 478−486.
75. Huang, J. F.; Hormann, N.; Oveisi, E.; Loiudice, A.; De Gregorio, G. L.; Andreussi, O.; Marzari, N.; Buonsanti, R., Potential-Induced Nanoclustering of Metallic Catalysts during Electrochemical CO2 Reduction. *Nat. Commun.* **2018,** *9*, 3117.
76. Li, Y. F.; Cui, F.; Ross, M. B.; Kim, D.; Sun, Y.; Yang, P. D., Structure-Sensitive CO2 Electroreduction to Hydrocarbons on Ultrathin 5-fold Twinned Copper Nanowires. *Nano Lett.* **2017,** *17* (2), 1312−1317.
77. Bagger, A.; Ju, W.; Varela, A. S.; Strasser, P.; Rossmeisl, J., Electrochemical CO2 Reduction: A Classification Problem. *ChemPhysChem* **2017,** *18* (22), 3266−3273.
78. Zhu, W. L.; Michalsky, R.; Metin, O.; Lv, H. F.; Guo, S. J.; Wright, C. J.; Sun, X. L.; Peterson, A. A.; Sun, S. H., Monodisperse Au Nanoparticles for Selective Electrocatalytic Reduction of CO2 to CO. *J. Am. Chem. Soc.* **2013,** *135* (45), 16833−16836.
79. Salehi-Khojin, A.; Jhong, H.-R. M.; Rosen, B. A.; Zhu, W.; Ma, S.; Kenis, P. J. A.; Masel, R. I., Nanoparticle Silver Catalysts That Show Enhanced Activity for Carbon Dioxide Electrolysis. *J. Phys. Chem. C* **2013,** *117* (4), 1627−1632.
80. Lee, H. E.; Yang, K. D.; Yoon, S. M.; Ahn, H. Y.; Lee, Y. Y.; Chang, H. J.; Jeong, D. H.; Lee, Y. S.; Kim, M. Y.; Nam, K. T., Concave Rhombic Dodecahedral Au Nanocatalyst with Multiple High-Index Facets for CO2 Reduction. *ACS Nano* **2015,** *9* (8), 8384−8393.
81. Liu, S.; Tao, H.; Zeng, L.; Liu, Q.; Xu, Z.; Liu, Q.; Luo, J. L., Shape-Dependent Electrocatalytic Reduction of CO2 to CO on Triangular Silver Nanoplates. *J. Am. Chem. Soc.* **2017,** *139* (6), 2160−2163.
82. Kim, D.; Yu, S.; Zheng, F.; Roh, I.; Li, Y. F.; Louisia, S.; Qi, Z. Y.; Somorjai, G. A.; Frei, H.; Wang, L. W.; Yang, P. D., Selective CO2 Electrocatalysis at the Pseudocapacitive Nanoparticle/Ordered-Ligand Interlayer. *Nat. Energy* **2020,** *5* (12), 1032−1042.
83. Kim, D.; Kley, C. S.; Li, Y. F.; Yang, P. D., Copper Nanoparticle Ensembles for Selective Electroreduction of CO2 to C2-C3 Products. *Proc. Natl. Acad. Sci. U. S. A.* **2017,** *114* (40), 10560−10565.
84. Li, Y. F.; Kim, D.; Louisia, S.; Xie, C. L.; Kong, Q.; Yu, S.; Lin, T.; Aloni, S.; Fakra, S. C.; Yang, P. D., Electrochemically Scrambled Nanocrystals Are Catalytically Active for CO2-to-Multicarbons. *Proc. Natl. Acad. Sci. U. S. A.* **2020,** *117* (17), 9194−9201.

85. Pang, Y. J.; Li, J.; Wang, Z. Y.; Tang, C. S.; Hsieh, P. L.; Zhuang, T. T.; Liang, Z. Q.; Zou, C. Q.; Wang, X.; De Luna, P.; Edwards, J. P.; Xu, Y.; Li, F. W.; Dinh, C. T.; Zhong, M.; Lou, Y. H.; Wu, D.; Chen, L. J.; Sargent, E. H.; Sinton, D., Efficient Electrocatalytic Conversion of Carbon Monoxide to Propanol Using Fragmented Copper. *Nat. Catal.* **2019,** *2* (3), 251−258.
86. Zhuang, T. T.; Pang, Y. J.; Liang, Z. Q.; Wang, Z. Y.; Li, Y.; Tan, C. S.; Li, J.; Dinh, C. T.; De Luna, P.; Hsieh, P. L.; Burdyny, T.; Li, H. H.; Liu, M. X.; Wang, Y. H.; Li, F. W.; Proppe, A.; Johnston, A.; Nam, D. H.; Wu, Z. Y.; Zheng, Y. R.; Ip, A. H.; Tan, H. R.; Chen, L. J.; Yu, S. H.; Kelley, S. O.; Sinton, D.; Sargent, E. H., Copper Nanocavities Confine Intermediates for Efficient Electrosynthesis of C3 Alcohol Fuels from Carbon Monoxide. *Nat. Catal.* **2018,** *1* (12), 946−951.
87. Wang, H. X.; Tzeng, Y. K.; Ji, Y. F.; Li, Y. B.; Li, J.; Zheng, X. L.; Yang, A. K.; Liu, Y. Y.; Gong, Y. J.; Cai, L. L.; Li, Y. Z.; Zhang, X. K.; Chen, W.; Liu, B. F.; Lu, H. Y.; Melosh, N. A.; Shen, Z. X.; Chan, K. R.; Tan, T. W.; Chu, S.; Cui, Y., Synergistic Enhancement of Electrocatalytic CO2 Reduction to C2 Oxygenates at Nitrogen-Doped Nanodiamonds/Cu Interface. *Nat. Nanotechnol.* **2020,** *15* (2), 131−137.
88. Wang, L.; Nitopi, S.; Wong, A. B.; Snider, J. L.; Nielander, A. C.; Morales-Guio, C. G.; Orazov, M.; Higgins, D. C.; Hahn, C.; Jaramillo, T. F., Electrochemically Converting Carbon Monoxide to Liquid Fuels by Directing Selectivity with Electrode Surface Area. *Nat. Catal.* **2019,** *2* (8), 702−708.
89. Choi, C.; Kwon, S.; Cheng, T.; Xu, M. J.; Tieu, P.; Lee, C.; Cai, J.; Lee, H. M.; Pan, X. Q.; Duan, X. F.; Goddard, W. A.; Huang, Y., Highly Active and Stable Stepped Cu Surface for Enhanced Electrochemical CO2 Reduction to C2H4. *Nat. Catal.* **2020,** *3* (10), 804−812.
90. Luc, W.; Fu, X. B.; Shi, J. J.; Lv, J. J.; Jouny, M.; Ko, B. H.; Xu, Y. B.; Tu, Q.; Hu, X. B.; Wu, J. S.; Yue, Q.; Liu, Y. Y.; Jiao, F.; Kang, Y. J., Two-Dimensional Copper Nanosheets for Electrochemical Reduction of Carbon Monoxide to Acetate. *Nat. Catal.* **2019,** *2* (5), 423−430.
91. Kim, D.; Resasco, J.; Yu, Y.; Asiri, A. M.; Yang, P. D., Synergistic Geometric and Electronic Effects for Electrochemical Reduction of Carbon Dioxide Using Gold−Copper Bimetallic Nanoparticles. *Nat. Commun.* **2014,** *5*, 4948.
92. Zhong, M.; Tran, K.; Min, Y. M.; Wang, C. H.; Wang, Z. Y.; Dinh, C. T.; De Luna, P.; Yu, Z. Q.; Rasouli, A. S.; Brodersen, P.; Sun, S.; Voznyy, O.; Tan, C. S.; Askerka, M.; Che, F. L.; Liu, M.; Seifitokaldani, A.; Pang, Y. J.; Lo, S. C.; Ip, A.; Ulissi, Z.; Sargent, E. H., Accelerated Discovery of CO2 Electrocatalysts Using Active Machine Learning. *Nature* **2020,** *581* (7807), 178−183.
93. Wang, L.; Higgins, D. C.; Ji, Y. F.; Morales-Guio, C. G.; Chan, K.; Hahn, C.; Jaramillo, T. F., Selective Reduction of CO to Acetaldehyde with CuAg Electrocatalysts. *Proc. Natl. Acad. Sci. U. S. A.* **2020,** *117* (23), 12572−12575.

94. Chen, C. B.; Li, Y. F.; Yu, S.; Louisia, S.; Jin, J. B.; Li, M. F.; Ross, M. B.; Yang, P. D., Cu−Ag Tandem Catalysts for High-Rate CO2 Electrolysis toward Multicarbons. *Joule* **2020,** *4* (8), 1688−1699.
95. Morales-Guio, C. G.; Cave, E. R.; Nitopi, S. A.; Feaster, J. T.; Wang, L.; Kuhl, K. P.; Jackson, A.; Johnson, N. C.; Abram, D. N.; Hatsukade, T.; Hahn, C.; Jaramillo, T. F., Improved CO2 Reduction Activity towards C2+ Alcohols on a Tandem Gold on Copper Electrocatalyst. *Nat. Catal.* **2018,** *1* (10), 764−771.
96. Higgins, D.; Hahn, C.; Xiang, C.; Jaramillo, T. F.; Weber, A. Z., Gas-Diffusion Electrodes for Carbon Dioxide Reduction: A New Paradigm. *ACS Energy Lett.* **2018,** *4* (1), 317−324.
97. Dinh, C. T.; Burdyny, T.; Kibria, M. G.; Seifitokaldani, A.; Gabardo, C. M.; de Arquer, F. P. G.; Kiani, A.; Edwards, J. P.; De Luna, P.; Bushuyev, O. S.; Zou, C. Q.; Quintero-Bermudez, R.; Pang, Y. J.; Sinton, D.; Sargent, E. H., CO2 Electroreduction to Ethylene via Hydroxide-Mediated Copper Catalysis at an Abrupt Interface. *Science* **2018,** *360* (6390), 783−787.
98. Van Hove, M. A., From Surface Science to Nanotechnology. *Catal. Today* **2006,** *113* (3−4), 133−140.
99. Stamenkovic, V. R.; Fowler, B.; Mun, B. S.; Wang, G. F.; Ross, P. N.; Lucas, C. A.; Markovic, N. M., Improved Oxygen Reduction Activity on Pt3Ni(111) via Increased Surface Site Availability. *Science* **2007,** *315* (5811), 493−497.
100. Huang, X. Q.; Zhao, Z. P.; Cao, L.; Chen, Y.; Zhu, E. B.; Lin, Z. Y.; Li, M. F.; Yan, A. M.; Zettl, A.; Wang, Y. M.; Duan, X. F.; Mueller, T.; Huang, Y., High-Performance Transition Metal-Doped Pt3Ni Octahedra for Oxygen Reduction Reaction. *Science* **2015,** *348* (6240), 1230−1234.
101. Zhang, J.; Yang, H.; Fang, J.; Zou, S., Synthesis and Oxygen Reduction Activity of Shape-Controlled Pt3Ni Nanopolyhedra. *Nano Lett.* **2010,** *10* (2), 638−644.
102. Li, M. F.; Zhao, Z. P.; Cheng, T.; Fortunelli, A.; Chen, C. Y.; Yu, R.; Zhang, Q. H.; Gu, L.; Merinov, B. V.; Lin, Z. Y.; Zhu, E. B.; Yu, T.; Jia, Q. Y.; Guo, J. H.; Zhang, L.; Goddard, W. A.; Huang, Y.; Duan, X. F., Ultrafine Jagged Platinum Nanowires Enable Ultrahigh Mass Activity for the Oxygen Reduction Reaction. *Science* **2016,** *354* (6318), 1414−1419.
103. Beermann, V.; Gocyla, M.; Kuhl, S.; Padgett, E.; Schmies, H.; Goerlin, M.; Erini, N.; Shviro, M.; Heggen, M.; Dunin-Borkowski, R. E.; Muller, D. A.; Strasser, P., Tuning the Electrocatalytic Oxygen Reduction Reaction Activity and Stability of Shape-Controlled Pt−Ni Nanoparticles by Thermal Annealing: Elucidating the Surface Atomic Structural and Compositional Changes. *J. Am. Chem. Soc.* **2017,** *139* (46), 16536−16547.
104. Chi, M. F.; Wang, C.; Lei, Y. K.; Wang, G. F.; Li, D. G.; More, K. L.; Lupini, A.; Allard, L. F.; Markovic, N. M.; Stamenkovic, V. R., Surface Faceting and Elemental

Diffusion Behaviour at Atomic Scale for Alloy Nanoparticles during in Situ Annealing. *Nat. Commun.* **2015,** *6*, 8925.
105. Wang, D. L.; Xin, H. L. L.; Hovden, R.; Wang, H. S.; Yu, Y. C.; Muller, D. A.; DiSalvo, F. J.; Abruna, H. D., Structurally Ordered Intermetallic Platinum−Cobalt Core−Shell Nanoparticles with Enhanced Activity and Stability as Oxygen Reduction Electrocatalysts. *Nat. Mater.* **2013,** *12* (1), 81−87.
106. Kim, D.; Xie, C. L.; Becknell, N.; Yu, Y.; Karamad, M.; Chan, K.; Crumlin, E. J.; Norskov, J. K.; Yang, P. D., Electrochemical Activation of CO2 through Atomic Ordering Transformations of AuCu Nanoparticles. *J. Am. Chem. Soc.* **2017,** *139* (24), 8329−8336.
107. Janssens, T. V. W.; Clausen, B. S.; Hvolbaek, B.; Falsig, H.; Christensen, C. H.; Bligaard, T.; Norskov, J. K., Insights into the Reactivity of Supported Au Nanoparticles: Combining Theory and Experiments. *Top. Catal.* **2007,** *44* (1−2), 15−26.
108. Calle-Vallejo, F.; Tymoczko, J.; Colic, V.; Vu, Q. H.; Pohl, M. D.; Morgenstern, K.; Loffreda, D.; Sautet, P.; Schuhmann, W.; Bandarenka, A. S., Finding Optimal Surface Sites on Heterogeneous Catalysts by Counting Nearest Neighbors. *Science* **2015,** *350* (6257), 185−189.
109. Jin, R. C., Quantum Sized, Thiolate-Protected Gold Nanoclusters. *Nanoscale* **2010,** *2* (3), 343−362.
110. Yamazoe, S.; Takano, S.; Kurashige, W.; Yokoyama, T.; Nitta, K.; Negishi, Y.; Tsukuda, T., Hierarchy of Bond Stiffnesses within Icosahedral-Based Gold Clusters Protected by Thiolates. *Nat. Commun.* **2016,** *7*, 10414.
111. Kauffman, D. R.; Alfonso, D.; Matranga, C.; Qian, H. F.; Jin, R. C., Experimental and Computational Investigation of Au25 Clusters and CO2: A Unique Interaction and Enhanced Electrocatalytic Activity. *J. Am. Chem. Soc.* **2012,** *134* (24), 10237−10243.
112. Li, D. G.; Wang, C.; Tripkovic, D.; Sun, S. H.; Markovic, N. M.; Stamenkovic, V. R., Surfactant Removal for Colloidal Nanoparticles from Solution Synthesis: The Effect on Catalytic Performance. *ACS Catal.* **2012,** *2* (7), 1358−1362.
113. Yoskamtorn, T.; Yamazoe, S.; Takahata, R.; Nishigaki, J.; Thivasasith, A.; Limtrakul, J.; Tsukuda, T., Thiolate-Mediated Selectivity Control in Aerobic Alcohol Oxidation by Porous Carbon-Supported Au25 Clusters. *ACS Catal.* **2014,** *4* (10), 3696−3700.
114. Austin, N.; Zhao, S.; McKone, J. R.; Jin, R. C.; Mpourmpakis, G., Elucidating the Active Sites for CO2 Electroreduction on Ligand-Protected Au25 Nanoclusters. *Catal. Sci. Technol.* **2018,** *8* (15), 3795−3805.
115. Li, F. W.; Thevenon, A.; Rosas-Hernandez, A.; Wang, Z. Y.; Li, Y. L.; Gabardo, C. M.; Ozden, A.; Dinh, C. T.; Li, J.; Wang, Y. H.; Edwards, J. P.; Xu, Y.; McCallum, C.; Tao, L. Z.; Liang, Z. Q.; Luo, M. C.; Wang, X.; Li, H. H.; O'Brien, C. P.; Tan, C. S.; Nam, D. H.; Quintero-Bermudez, R.; Zhuang, T. T.; Li, Y. G. C.; Han, Z. J.; Britt, R. D.; Sinton,

D.; Agapie, T.; Peters, J. C.; Sargent, E. H., Molecular Tuning of CO2-to-Ethylene Conversion. *Nature* **2020,** *577* (7791), 509−513.
116. Chen, S. P.; Niu, Z. Q.; Xie, C. L.; Gao, M. Y.; Lai, M. L.; Li, M. F.; Yang, P. D., Effects of Catalyst Processing on the Activity and Stability of Pt−Ni Nanoframe Electrocatalysts. *ACS Nano* **2018,** *12* (8), 8697−8705.
117. Stamenkovic, V.; Mun, B. S.; Mayrhofer, K. J. J.; Ross, P. N.; Markovic, N. M.; Rossmeisl, J.; Greeley, J.; Norskov, J. K., Changing the Activity of Electrocatalysts for Oxygen Reduction by Tuning the Surface Electronic Structure. *Angew. Chem., Int. Ed.* **2006,** *45* (18), 2897−2901.
118. Stamenkovic, V. R.; Mun, B. S.; Mayrhofer, K. J. J.; Ross, P. N.; Markovic, N. M., Effect of Surface Composition on Electronic Structure, Stability, and Electrocatalytic Properties of Pt−Transition Metal Alloys: Pt-Skin versus Pt-Skeleton Surfaces. *J. Am. Chem. Soc.* **2006,** *128* (27), 8813−8819.
119. Shao, M. H.; Chang, Q. W.; Dodelet, J. P.; Chenitz, R., Recent Advances in Electrocatalysts for Oxygen Reduction Reaction. *Chem. Rev.* **2016,** *116* (6), 3594−3657.
120. Wang, Y. J.; Zhao, N. N.; Fang, B. Z.; Li, H.; Bi, X. T. T.; Wang, H. J., Carbon-Supported Pt-Based Alloy Electrocatalysts for the Oxygen Reduction Reaction in Polymer Electrolyte Membrane Fuel Cells: Particle Size, Shape, and Composition Manipulation and Their Impact to Activity. *Chem. Rev.* **2015,** *115* (9), 3433−3467.
121. Cui, C. H.; Gan, L.; Li, H. H.; Yu, S. H.; Heggen, M.; Strasser, P., Octahedral PtNi Nanoparticle Catalysts: Exceptional Oxygen Reduction Activity by Tuning the Alloy Particle Surface Composition. *Nano Lett.* **2012,** *12* (11), 5885−5889.
122. Choi, S. I.; Xie, S. F.; Shao, M. H.; Odell, J. H.; Lu, N.; Peng, H. C.; Protsailo, L.; Guerrero, S.; Park, J. H.; Xia, X. H.; Wang, J. G.; Kim, M. J.; Xia, Y. N., Synthesis and Characterization of 9 nm Pt−Ni Octahedra with a Record High Activity of 3.3 A/mg(Pt) for the Oxygen Reduction Reaction. *Nano Lett.* **2013,** *13* (7), 3420−3425.
123. Bezerra, C. W. B.; Zhang, L.; Liu, H. S.; Lee, K. C.; Marques, A. L. B.; Marques, E. P.; Wang, H. J.; Zhang, J. J., A Review of Heat-Treatment Effects on Activity and Stability of PEM Fuel Cell Catalysts for Oxygen Reduction Reaction. *J. Power Sources* **2007,** *173* (2), 891−908.
124. Cui, C.; Ahmadi, M.; Behafarid, F.; Gan, L.; Neumann, M.; Heggen, M.; Roldan Cuenya, B.; Strasser, P., Shape-Selected Bimetallic Nanoparticle Electrocatalysts: Evolution of Their Atomic-Scale Structure, Chemical Composition, and Electrochemical Reactivity under Various Chemical Environments. *Faraday Discuss.* **2013,** *162*, 91−112.
125. Durst, J.; Lopez-Haro, M.; Dubau, L.; Chatenet, M.; Soldo-Olivier, Y.; Guetaz, L.; Bayle-Guillemaud, P.; Maillard, F., Reversibility of Pt-Skin and Pt-Skeleton Nanostructures in Acidic Media. *J. Phys. Chem. Lett.* **2014,** *5* (3), 434−439.
126. Gan, L.; Heggen, M.; Cui, C. H.; Strasser, P., Thermal Facet Healing of Concave Octahedral Pt−Ni Nanoparticles Imaged in Situ at the Atomic Scale: Implications for the

Rational Synthesis of Durable High-Performance ORR Electrocatalysts. *ACS Catal.* **2016,** *6* (2), 692−695.
127. Dai, S.; You, Y.; Zhang, S. Y.; Cai, W.; Xu, M. J.; Xie, L.; Wu, R. Q.; Graham, G. W.; Pan, X. Q., In Situ Atomic-Scale Observation of Oxygen-Driven Core−Shell Formation in Pt3Co Nanoparticles. *Nat. Commun.* **2017,** *8*, 204.
128. van der Vliet, D. F.; Wang, C.; Li, D. G.; Paulikas, A. P.; Greeley, J.; Rankin, R. B.; Strmcnik, D.; Tripkovic, D.; Markovic, N. M.; Stamenkovic, V. R., Unique Electrochemical Adsorption Properties of Pt-Skin Surfaces. *Angew. Chem., Int. Ed.* **2012,** *51* (13), 3139−3142.
129. Han, B. H.; Carlton, C. E.; Kongkanand, A.; Kukreja, R. S.; Theobald, B. R.; Gan, L.; O'Malley, R.; Strasser, P.; Wagner, F. T.; Shao-Horn, Y., Record Activity and Stability of Dealloyed Bimetallic Catalysts for Proton Exchange Membrane Fuel Cells. *Energy Environ. Sci.* **2015,** *8* (1), 258−266.
130. Aran-Ais, R. M.; Solla-Gullon, J.; Gocyla, M.; Heggen, M.; Dunin-Borkowski, R. E.; Strasser, P.; Herrero, E.; Feliu, J. M., The Effect of Interfacial pH on the Surface Atomic Elemental Distribution and on the Catalytic Reactivity of Shape-Selected Bimetallic Nanoparticles towards Oxygen Reduction. *Nano Energy* **2016,** *27*, 390−401.
131. Strasser, P.; Kuhl, S., Dealloyed Pt-Based Core−Shell Oxygen Reduction Electrocatalysts. *Nano Energy* **2016,** *29*, 166−177.
132. Niu, Z. Q.; Becknell, N.; Yu, Y.; Kim, D.; Chen, C.; Kornienko, N.; Somorjai, G. A.; Yang, P. D., Anisotropic Phase Segregation and Migration of Pt in Nanocrystals en Route to Nanoframe Catalysts. *Nat. Mater.* **2016,** *15* (11), 1188−1194.
133. Becknell, N.; Son, Y.; Kim, D.; Li, D. G.; Yu, Y.; Niu, Z. Q.; Lei, T.; Sneed, B. T.; More, K. L.; Markovic, N. M.; Stamenkovic, V. R.; Yang, P. D., Control of Architecture in Rhombic Dodecahedral Pt−Ni Nanoframe Electrocatalysts. *J. Am. Chem. Soc.* **2017,** *139* (34), 11678−11681.
134. Becknell, N.; Kang, Y. J.; Chen, C.; Resasco, J.; Kornienko, N.; Guo, J. H.; Markovic, N. M.; Somorjai, G. A.; Stamenkovic, V. R.; Yang, P. D., Atomic Structure of Pt3Ni Nanoframe Electrocatalysts by in Situ X-ray Absorption Spectroscopy. *J. Am. Chem. Soc.* **2015,** *137* (50), 15817−15824.
135. Toda, T.; Igarashi, H.; Uchida, H.; Watanabe, M., Enhancement of the Electroreduction of Oxygen on Pt Alloys with Fe, Ni, and Co. *J. Electrochem. Soc.* **1999,** *146* (10), 3750−3756.
136. Wan, L. J.; Moriyama, T.; Ito, M.; Uchida, H.; Watanabe, M., In Situ STM Imaging of Surface Dissolution and Rearrangement of a Pt−Fe Alloy Electrocatalyst in Electrolyte Solution. *Chem. Commun.* **2002,** (1), 58−59.
137. Stephens, I. E. L.; Bondarenko, A. S.; Gronbjerg, U.; Rossmeisl, J.; Chorkendorff, I., Understanding the Electrocatalysis of Oxygen Reduction on Platinum and Its Alloys. *Energy Environ. Sci.* **2012,** *5* (5), 6744−6762.

138. Chen, S. P.; Li, M. F.; Gao, M. Y.; Jin, J. B.; van Spronsen, M. A.; Salmeron, M. B.; Yang, P. D., High-Performance Pt−Co Nanoframes for Fuel-Cell Electrocatalysis. *Nano Lett.* **2020,** *20* (3), 1974−1979.
139. Kamarudin, S. K.; Achmad, F.; Daud, W. R. W., Overview on the Application of Direct Methanol Fuel Cell (DMFC) for Portable Electronic Devices. *Int. J. Hydrog. Energy* **2009,** *34* (16), 6902−6916.
140. Porter, N. S.; Wu, H.; Quan, Z. W.; Fang, J. Y., Shape-Control and Electrocatalytic Activity-Enhancement of Pt-Based Bimetallic Nanocrystals. *Acc. Chem. Res.* **2013,** *46* (8), 1867−1877.
141. Ren, F. F.; Wang, C. Q.; Zhai, C. Y.; Jiang, F. X.; Yue, R. R.; Du, Y. K.; Yang, P.; Xu, J. K., One-Pot Synthesis of a RGO-Supported Ultrafine Ternary PtAuRu Catalyst with High Electrocatalytic Activity towards Methanol Oxidation in Alkaline Medium. *J. Mater. Chem. A* **2013,** *1* (24), 7255−7261.
142. Rudi, S.; Teschner, D.; Beermann, V.; Hetaba, W.; Gan, L.; Cui, C. H.; Gliech, M.; Schlogl, R.; Strasser, P., pH-Induced versus Oxygen-Induced Surface Enrichment and Segregation Effects in Pt−Ni Alloy Nanoparticle Fuel Cell Catalysts. *ACS Catal.* **2017,** *7* (9), 6376−6384.
143. Fang, Y.; Yang, X. D.; Wang, L.; Liu, Y. N., An Alkaline Direct Methanol Fuel Cell with a Polymer Fiber Membrane and MnO2-Catalyzed Cathode. *Electrochim. Acta* **2013,** *90*, 421−425.
144. Antolini, E.; Gonzalez, E. R., Alkaline Direct Alcohol Fuel Cells. *J. Power Sources* **2010,** *195* (11), 3431−3450.
145. Aran-Ais, R. M.; Dionigi, F.; Merzdorf, T.; Gocyla, M.; Heggen, M.; Dunin-Borkowski, R. E.; Gliech, M.; Solla-Gullon, J.; Herrero, E.; Feliu, J. M.; Strasser, P., Elemental Anisotropic Growth and Atomic-Scale Structure of Shape-Controlled Octahedral Pt−Ni−Co Alloy Nanocatalysts. *Nano Lett.* **2015,** *15* (11), 7473−7480.
146. Li, M. F.; Duanmu, K. N.; Wan, C. Z.; Cheng, T.; Zhang, L.; Dai, S.; Chen, W. X.; Zhao, Z. P.; Li, P.; Fei, H. L.; Zhu, Y. M.; Yu, R.; Luo, J.; Zang, K. T.; Lin, Z. Y.; Ding, M. N.; Huang, J.; Sun, H. T.; Guo, J. H.; Pan, X. Q.; Goddard, W. A.; Sautet, P.; Huang, Y.; Duan, X. F., Single-Atom Tailoring of Platinum Nanocatalysts for High-Performance Multifunctional Electrocatalysis. *Nat. Catal.* **2019,** *2* (6), 495−503.
147. Feng, Y. Y.; Bi, L. X.; Liu, Z. H.; Kong, D. S.; Yu, Z. Y., Significantly Enhanced Electrocatalytic Activity for Methanol Electro-Oxidation on Ag Oxide-Promoted PtAg/C Catalysts in Alkaline Electrolyte. *J. Catal.* **2012,** *290*, 18−25.
148. Gan, L.; Cui, C. H.; Heggen, M.; Dionigi, F.; Rudi, S.; Strasser, P., Element-Specific Anisotropic Growth of Shaped Platinum Alloy Nanocrystals. *Science* **2014,** *346* (6216), 1502−1506.
149. Huang, W. J.; Wang, H. T.; Zhou, J. G.; Wang, J.; Duchesne, P. N.; Muir, D.; Zhang, P.; Han, N.; Zhao, F. P.; Zeng, M.; Zhong, J.; Jin, C. H.; Li, Y. G.; Lee, S. T.; Dai, H. J.,

Highly Active and Durable Methanol Oxidation Electrocatalyst Based on the Synergy of Platinum−Nickel Hydroxide−Graphene. *Nat. Commun.* **2015,** *6*, 10035.
150. Chong, L.; Wen, J. G.; Kubal, J.; Sen, F. G.; Zou, J. X.; Greeley, J.; Chan, M.; Barkholtz, H.; Ding, W. J.; Liu, D. J., Ultralow-Loading Platinum−Cobalt Fuel Cell Catalysts Derived from Imidazolate Frameworks. *Science* **2018,** *362* (6420), 1276−1281.
151. Bu, L. Z.; Guo, S. J.; Zhang, X.; Shen, X.; Su, D.; Lu, G.; Zhu, X.; Yao, J. L.; Guo, J.; Huang, X. Q., Surface Engineering of Hierarchical Platinum−Cobalt Nanowires for Efficient Electrocatalysis. *Nat. Commun.* **2016,** *7*, 11850.
152. Zadick, A.; Dubau, L.; Sergent, N.; Berthome, G.; Chatenet, M., Huge Instability of Pt/C Catalysts in Alkaline Medium. *ACS Catal.* **2015,** *5* (8), 4819−4824.
153. Chen, S. P.; Liu, X. Y.; Jin, J. B.; Gao, M. Y.; Chen, C. B.; Kong, Q.; Ji, Z.; Somorjai, G. A.; Yaghi, O. M.; Yang, P. D., Individually Encapsulated Frame-in-Frame Structure. *ACS Materials Lett.* **2020,** *2* (7), 685−690.
154. Skrabalak, S. E.; Chen, J. Y.; Sun, Y. G.; Lu, X. M.; Au, L.; Cobley, C. M.; Xia, Y. N., Gold Nanocages: Synthesis, Properties, and Applications. *Acc. Chem. Res.* **2008,** *41* (12), 1587−1595.
155. Horike, S.; Nagarkar, S. S.; Ogawa, T.; Kitagawa, S., A New Dimension for Coordination Polymers and Metal−Organic Frameworks: Towards Functional Glasses and Liquids. *Angew. Chem., Int. Ed.* **2020,** *59* (17), 6652−6664.
156. Yaghi, O. M.; Kalmutzki, M. J.; Diercks, C. S., *Introduction to Reticular Chemistry: Metal−Organic Frameworks and Covalent Organic Frameworks*. Wiley-VCH: 2019.
157. Wu, Y. E.; Cai, S. F.; Wang, D. S.; He, W.; Li, Y. D., Syntheses of Water-Soluble Octahedral, Truncated Octahedral, and Cubic Pt−Ni Nanocrystals and Their Structure−Activity Study in Model Hydrogenation Reactions. *J. Am. Chem. Soc.* **2012,** *134* (21), 8975−8981.
158. Becknell, N.; Zheng, C. D.; Chen, C.; Yu, Y.; Yang, P. D., Synthesis of PtCo3 Polyhedral Nanoparticles and Evolution to Pt3Co Nanoframes. *Surf. Sci.* **2016,** *648*, 328−332.
159. Hu, P.; Morabito, J. V.; Tsung, C. K., Core−Shell Catalysts of Metal Nanoparticle Core and Metal−Organic Framework Shell. *ACS Catal.* **2014,** *4* (12), 4409−4419.
160. Rungtaweevoranit, B.; Zhao, Y. B.; Choi, K. M.; Yaghi, O. M., Cooperative Effects at the Interface of Nanocrystalline Metal−Organic Frameworks. *Nano Res.* **2016,** *9* (1), 47−58.
161. Zhao, M. T.; Yuan, K.; Wang, Y.; Li, G. D.; Guo, J.; Gu, L.; Hu, W. P.; Zhao, H. J.; Tang, Z. Y., Metal−organic Frameworks as Selectivity Regulators for Hydrogenation Reactions. *Nature* **2016,** *539* (7627), 76−80.
162. Yang, Q. H.; Xu, Q.; Jiang, H. L., Metal−Organic Frameworks Meet Metal Nanoparticles: Synergistic Effect for Enhanced Catalysis. *Chem. Soc. Rev.* **2017,** *46* (15), 4774−4808.

163. Stephenson, C. J.; Hupp, J. T.; Farha, O. K., Postassembly Transformation of a Catalytically Active Composite Material, Pt@ZIF-8, via Solvent-Assisted Linker Exchange. *Inorg. Chem.* **2016,** *55* (4), 1361−1363.
164. He, L. C.; Liu, Y.; Liu, J. Z.; Xiong, Y. S.; Zheng, J. Z.; Liu, Y. L.; Tang, Z. Y., Core−Shell Noble-Metal@Metal−Organic Framework Nanoparticles with Highly Selective Sensing Property. *Angew. Chem., Int. Ed.* **2013,** *52* (13), 3741−3745.
165. Na, K.; Choi, K. M.; Yaghi, O. M.; Somorjai, G. A., Metal Nanocrystals Embedded in Single Nanocrystals of MOFs Give Unusual Selectivity as Heterogeneous Catalysts. *Nano Lett.* **2014,** *14* (10), 5979−5983.
166. Li, Z.; Yu, R.; Huang, J. L.; Shi, Y. S.; Zhang, D. Y.; Zhong, X. Y.; Wang, D. S.; Wu, Y. E.; Li, Y. D., Platinum−Nickel Frame within Metal−Organic Framework Fabricated in Situ for Hydrogen Enrichment and Molecular Sieving. *Nat. Commun.* **2015,** *6*, 8248.
167. Zhang, N.; Shao, Q.; Wang, P. T.; Zhu, X.; Huang, X. Q., Porous Pt−Ni Nanowires within in Situ Generated Metal−Organic Frameworks for Highly Chemoselective Cinnamaldehyde Hydrogenation. *Small* **2018,** *14* (19), 1704318.
168. Lu, G.; Li, S. Z.; Guo, Z.; Farha, O. K.; Hauser, B. G.; Qi, X. Y.; Wang, Y.; Wang, X.; Han, S. Y.; Liu, X. G.; DuChene, J. S.; Zhang, H.; Zhang, Q. C.; Chen, X. D.; Ma, J.; Loo, S. C. J.; Wei, W. D.; Yang, Y. H.; Hupp, J. T.; Huo, F. W., Imparting Functionality to a Metal−Organic Framework Material by Controlled Nanoparticle Encapsulation. *Nat. Chem.* **2012,** *4* (4), 310−316.
169. Hu, P.; Zhuang, J.; Chou, L. Y.; Lee, H. K.; Ling, X. Y.; Chuang, Y. C.; Tsung, C. K., Surfactant-Directed Atomic to Mesoscale Alignment: Metal Nanocrystals Encased Individually in Single-Crystalline Porous Nanostructures. *J. Am. Chem. Soc.* **2014,** *136* (30), 10561−10564.
170. Wu, L. Z.; Yu, J. Q.; Chen, L.; Yang, D.; Zhang, S. M.; Han, L.; Ban, M. Y.; He, L.; Xu, Y.; Zhang, Q., A General and Facile Approach to Disperse Hydrophobic Nanocrystals in Water with Enhanced Long-Term Stability. *J. Mater. Chem. C* **2017,** *5* (12), 3065−3071.
171. Pan, Y. C.; Heryadi, D.; Zhou, F.; Zhao, L.; Lestari, G.; Su, H. B.; Lai, Z. P., Tuning the Crystal Morphology and Size of Zeolitic Imidazolate Framework-8 in Aqueous Solution by Surfactants. *CrystEngComm* **2011,** *13* (23), 6937−6940.
172. Kuo, C. H.; Tang, Y.; Chou, L. Y.; Sneed, B. T.; Brodsky, C. N.; Zhao, Z. P.; Tsung, C. K., Yolk−Shell Nanocrystal@ZIF-8 Nanostructures for Gas-Phase Heterogeneous Catalysis with Selectivity Control. *J. Am. Chem. Soc.* **2012,** *134* (35), 14345−14348.
173. Saliba, D.; Ammar, M.; Rammal, M.; Al-Ghoul, M.; Hmadeh, M., Crystal Growth of ZIF-8, ZIF-67, and Their Mixed-Metal Derivatives. *J. Am. Chem. Soc.* **2018,** *140* (5), 1812−1823.

174. Liu, X. Y.; Lo, W. S.; Wu, C. H.; Williams, B. P.; Luo, L. S.; Li, Y.; Chou, L. Y.; Lee, Y.; Tsung, C. K., Tuning Metal−Organic Framework Nanocrystal Shape through Facet-Dependent Coordination. *Nano Lett.* **2020,** *20* (3), 1774−1780.
175. Liu, X. Y.; Zhang, F. R.; Goh, T. W.; Li, Y.; Shao, Y. C.; Luo, L. S.; Huang, W. Y.; Long, Y. T.; Chou, L. Y.; Tsung, C. K., Using a Multi-Shelled Hollow Metal−Organic Framework as a Host to Switch the Guest-to-Host and Guest-to-Guest Interactions. *Angew. Chem., Int. Ed.* **2018,** *57* (8), 2110−2114.
176. Schejn, A.; Balan, L.; Falk, V.; Aranda, L.; Medjahdi, G.; Schneider, R., Controlling ZIF-8 Nano- and Microcrystal Formation and Reactivity through Zinc Salt Variations. *CrystEngComm* **2014,** *16* (21), 4493−4500.
177. Niu, Z. Q.; Chen, S. P.; Yu, Y.; Lei, T.; Dehestani, A.; Schierle-Arndt, K.; Yang, P. D., Morphology-Controlled Transformation of Cu@Au Core−Shell Nanowires into Thermally Stable Cu3Au Intermetallic Nanowires. *Nano Res.* **2020,** *13* (9), 2564−2569.
178. Chen, P. C.; Liu, X. L.; Hedrick, J. L.; Xie, Z.; Wang, S. Z.; Lin, Q. Y.; Hersam, M. C.; Dravid, V. P.; Mirkin, C. A., Polyelemental Nanoparticle Libraries. *Science* **2016,** *352* (6293), 1565−1569.
179. Yao, Y. G.; Huang, Z. N.; Xie, P. F.; Lacey, S. D.; Jacob, R. J.; Xie, H.; Chen, F. J.; Nie, A. M.; Pu, T. C.; Rehwoldt, M.; Yu, D. W.; Zachariah, M. R.; Wang, C.; Shahbazian-Yassar, R.; Li, J.; Hu, L. B., Carbothermal Shock Synthesis of High-Entropy-Alloy Nanoparticles. *Science* **2018,** *359* (6383), 1489−1494.
180. Cortie, M. B.; McDonagh, A. M., Synthesis and Optical Properties of Hybrid and Alloy Plasmonic Nanoparticles. *Chem. Rev.* **2011,** *111* (6), 3713−3735.
181. Casado-Rivera, E.; Volpe, D. J.; Alden, L.; Lind, C.; Downie, C.; Vazquez-Alvarez, T.; Angelo, A. C. D.; DiSalvo, F. J.; Abruna, H. D., Electrocatalytic Activity of Ordered Intermetallic Phases for Fuel Cell Applications. *J. Am. Chem. Soc.* **2004,** *126* (12), 4043−4049.
182. Rossner, L.; Armbruster, M., Electrochemical Energy Conversion on Intermetallic Compounds: A Review. *ACS Catal.* **2019,** *9* (3), 2018−2062.
183. Escudero-Escribano, M.; Verdaguer-Casadevall, A.; Malacrida, P.; Gronbjerg, U.; Knudsen, B. P.; Jepsen, A. K.; Rossmeisl, J.; Stephens, I. E. L.; Chorkendorff, I., Pt5Gd as a Highly Active and Stable Catalyst for Oxygen Electroreduction. *J. Am. Chem. Soc.* **2012,** *134* (40), 16476−16479.
184. Yan, Y. C.; Du, J. S. S.; Gilroy, K. D.; Yang, D. R.; Xia, Y. N.; Zhang, H., Intermetallic Nanocrystals: Syntheses and Catalytic Applications. *Adv. Mater.* **2017,** *29* (14), 1605997.
185. Xiong, Y.; Yang, Y.; DiSalvo, F. J.; Abruna, H. D., Pt-Decorated Composition-Tunable Pd−Fe@Pd/C Core−Shell Nanoparticles with Enhanced Electrocatalytic Activity toward the Oxygen Reduction Reaction. *J. Am. Chem. Soc.* **2018,** *140* (23), 7248−7255.

186. Bauer, J. C.; Chen, X.; Liu, Q. S.; Phan, T. H.; Schaak, R. E., Converting Nanocrystalline Metals into Alloys and Intermetallic Compounds for Applications in Catalysis. *J. Mater. Chem.* **2008,** *18* (3), 275−282.
187. Wang, C. Y.; Chen, D. P.; Sang, X. H.; Unocic, R. R.; Skrabalak, S. E., Size-Dependent Disorder−Order Transformation in the Synthesis of Monodisperse Intermetallic PdCu Nanocatalysts. *ACS Nano* **2016,** *10* (6), 6345−6353.
188. Lu, N.; Wang, J. G.; Xie, S. F.; Xia, Y. N.; Kim, M. J., Enhanced Shape Stability of Pd−Rh Core−Frame Nanocubes at Elevated Temperature: In Situ Heating Transmission Electron Microscopy. *Chem. Commun.* **2013,** *49* (100), 11806−11808.
189. Li, J. R.; Xi, Z.; Pan, Y. T.; Spendelow, J. S.; Duchesne, P. N.; Su, D.; Li, Q.; Yu, C.; Yin, Z. Y.; Shen, B.; Kim, Y. S.; Zhang, P.; Sun, S. H., Fe Stabilization by Intermetallic L1(0)-FePt and Pt Catalysis Enhancement in L1(0)-FePt/Pt Nanoparticles for Efficient Oxygen Reduction Reaction in Fuel Cells. *J. Am. Chem. Soc.* **2018,** *140* (8), 2926−2932.
190. Maligal-Ganesh, R. V.; Xiao, C. X.; Goh, T. W.; Wang, L. L.; Gustafson, J.; Pei, Y. C.; Qi, Z. Y.; Johnson, D. D.; Zhang, S. R.; Tao, F.; Huang, W. Y., A Ship-in-a-Bottle Strategy To Synthesize Encapsulated Intermetallic Nanoparticle Catalysts: Exemplified for Furfural Hydrogenation. *ACS Catal.* **2016,** *6* (3), 1754−1763.
191. Chung, D. Y.; Jun, S. W.; Yoon, G.; Kwon, S. G.; Shin, D. Y.; Seo, P.; Yoo, J. M.; Shin, H.; Chung, Y. H.; Kim, H.; Mun, B. S.; Lee, K. S.; Lee, N. S.; Yoo, S. J.; Lim, D. H.; Kang, K.; Sung, Y. E.; Hyeon, T., Highly Durable and Active PtFe Nanocatalyst for Electrochemical Oxygen Reduction Reaction. *J. Am. Chem. Soc.* **2015,** *137* (49), 15478−15485.
192. Liang, J. S.; Li, N.; Zhao, Z. L.; Ma, L.; Wang, X. M.; Li, S. Z.; Liu, X.; Wang, T. Y.; Du, Y. P.; Lu, G.; Han, J. T.; Huang, Y. H.; Su, D.; Li, Q., Tungsten-Doped L1(0)-PtCo Ultrasmall Nanoparticles as a High-Performance Fuel Cell Cathode. *Angew. Chem., Int. Ed.* **2019,** *58* (43), 15471−15477.
193. Wang, T. Y.; Liang, J. S.; Zhao, Z. L.; Li, S. Z.; Lu, G.; Xia, Z. C.; Wang, C.; Luo, J. H.; Han, J. T.; Ma, C.; Huang, Y. H.; Li, Q., Sub-6 nm Fully Ordered L1(0)-Pt−Ni−Co Nanoparticles Enhance Oxygen Reduction via Co Doping Induced Ferromagnetism Enhancement and Optimized Surface Strain. *Adv. Energy Mater.* **2019,** *9* (17), 1803771.
194. Wang, C.; Hou, Y. L.; Kim, J. M.; Sun, S. H., A General Strategy for Synthesizing FePt Nanowires and Nanorods. *Angew. Chem., Int. Ed.* **2007,** *46* (33), 6333−6335.
195. Chen, Q. L.; Zhang, J. W.; Jia, Y. Y.; Jiang, Z. Y.; Xie, Z. X.; Zheng, L. S., Wet Chemical Synthesis of Intermetallic Pt3Zn Nanocrystals via Weak Reduction Reaction Together with UPD Process and Their Excellent Electrocatalytic Performances. *Nanoscale* **2014,** *6* (12), 7019−7024.
196. Chou, N. H.; Schaak, R. E., Shape-Controlled Conversion of β-Sn Nanocrystals into Intermetallic M−Sn (M = Fe, Co, Ni, Pd) Nanocrystals. *J. Am. Chem. Soc.* **2007,** *129* (23), 7339−7345.

197. Gao, Q.; Ju, Y. M.; An, D.; Gao, M. R.; Cui, C. H.; Liu, J. W.; Cong, H. P.; Yu, S. H., Shape-Controlled Synthesis of Monodisperse PdCu Nanocubes and Their Electrocatalytic Properties. *ChemSusChem* **2013,** *6* (10), 1878−1882.
198. Liao, H. B.; Zhu, J. H.; Hou, Y. L., Synthesis and Electrocatalytic Properties of PtBi Nanoplatelets and PdBi Nanowires. *Nanoscale* **2014,** *6* (2), 1049−1055.
199. Luo, Z. S.; Lu, J. M.; Flox, C.; Nafria, R.; Genc, A.; Arbiol, J.; Llorca, J.; Ibanez, M.; Morante, J. R.; Cabot, A., Pd2Sn [010] Nanorods as a Highly Active and Stable Ethanol Oxidation Catalyst. *J. Mater. Chem. A* **2016,** *4* (42), 16706−16713.
200. Maksimuk, S.; Yang, S. C.; Peng, Z. M.; Yang, H., Synthesis and Characterization of Ordered Intermetallic PtPb Nanorods. *J. Am. Chem. Soc.* **2007,** *129* (28), 8684−8685.
201. Rong, H. P.; Mao, J. J.; Xin, P. Y.; He, D. S.; Chen, Y. J.; Wang, D. S.; Niu, Z. Q.; Wu, Y.; Li, Y. D., Kinetically Controlling Surface Structure to Construct Defect-Rich Intermetallic Nanocrystals: Effective and Stable Catalysts. *Adv. Mater.* **2016,** *28* (13), 2540−2546.
202. Liu, S. J.; Sun, Z. H.; Liu, Q. H.; Wu, L. H.; Huang, Y. Y.; Yao, T.; Zhang, J.; Hu, T. D.; Ge, M. R.; Hu, F. C.; Xie, Z.; Pan, G. Q.; Wei, S. Q., Unidirectional Thermal Diffusion in Bimetallic Cu@Au Nanoparticles. *ACS Nano* **2014,** *8* (2), 1886−1892.
203. Sra, A. K.; Ewers, T. D.; Schaak, R. E., Direct Solution Synthesis of Intermetallic AuCu and AuCu3 Nanocrystals and Nanowire Networks. *Chem. Mater.* **2005,** *17* (4), 758−766.
204. Yang, J. H.; Chng, L. L.; Yang, X. F.; Chen, X. J.; Ying, J. Y., Multiply-Twinned Intermetallic AuCu Pentagonal Nanorods. *Chem. Commun.* **2014,** *50* (9), 1141−1143.
205. Barth, S.; Boland, J. J.; Holmes, J. D., Defect Transfer from Nanoparticles to Nanowires. *Nano Lett.* **2011,** *11* (4), 1550−1555.
206. Li, Q.; Wu, L. H.; Wu, G.; Su, D.; Lv, H. F.; Zhang, S.; Zhu, W. L.; Casimir, A.; Zhu, H. Y.; Mendoza-Garcia, A.; Sun, S. H., New Approach to Fully Ordered fct-FePt Nanoparticles for Much Enhanced Electrocatalysis in Acid. *Nano Lett.* **2015,** *15* (4), 2468−2473.
207. Li, J. R.; Sun, S., Intermetallic Nanoparticles: Synthetic Control and Their Enhanced Electrocatalysis. *Acc. Chem. Res.* **2019,** *52* (7), 2015−2025.
208. Cui, F.; Yu, Y.; Dou, L. T.; Sun, J. W.; Yang, Q.; Schildknecht, C.; Schierle-Arndt, K.; Yang, P. D., Synthesis of Ultrathin Copper Nanowires Using Tris(trimethylsilyl)silane for High-Performance and Low-Haze Transparent Conductors. *Nano Lett.* **2015,** *15* (11), 7610−7615.
209. Jin, M. S.; He, G. N.; Zhang, H.; Zeng, J.; Xie, Z. X.; Xia, Y. N., Shape-Controlled Synthesis of Copper Nanocrystals in an Aqueous Solution with Glucose as a Reducing Agent and Hexadecylamine as a Capping Agent. *Angew. Chem., Int. Ed.* **2011,** *50* (45), 10560−10564.

210. Yang, H. J.; He, S. Y.; Tuan, H. Y., Self-Seeded Growth of Five-Fold Twinned Copper Nanowires: Mechanistic Study, Characterization and SERS Applications. *Langmuir* **2014,** *30* (2), 602−610.
211. Cui, F.; Dou, L. T.; Yang, Q.; Yu, Y.; Niu, Z. Q.; Sun, Y. C.; Liu, H.; Dehestani, A.; Schierle-Arndt, K.; Yang, P. D., Benzoin Radicals as Reducing Agent for Synthesizing Ultrathin Copper Nanowires. *J. Am. Chem. Soc.* **2017,** *139* (8), 3027−3032.
212. Niu, Z. Q.; Cui, F.; Kuttner, E.; Xie, C. L.; Chen, H.; Sun, Y. C.; Dehestani, A.; Schierle-Arndt, K.; Yang, P. D., Synthesis of Silver Nanowires with Reduced Diameters Using Benzoin-Derived Radicals to Make Transparent Conductors with High Transparency and Low Haze. *Nano Lett.* **2018,** *18* (8), 5329−5334.
213. Sun, Y. G.; Ren, Y.; Liu, Y. Z.; Wen, J. G.; Okasinski, J. S.; Miller, D. J., Ambient-Stable Tetragonal Phase in Silver Nanostructures. *Nat. Commun.* **2012,** *3*, 971.
214. Niu, Z. Q.; Cui, F.; Yu, Y.; Becknell, N.; Sun, Y. C.; Khanarian, G.; Kim, D.; Dou, L.; Dehestani, A.; Schierle-Arndt, K.; Yang, P. D., Ultrathin Epitaxial Cu@Au Core−Shell Nanowires for Stable Transparent Conductors. *J. Am. Chem. Soc.* **2017,** *139* (21), 7348−7354.
215. Bonneaux, J.; Guymont, M., Study of the Order−Disorder Transition Series in AuCu by in-Situ Temperature Electron Microscopy. *Intermetallics* **1999,** *7* (7), 797−805.
216. Chen, H. Q.; Nishijima, M.; Wang, G. J.; Khene, S.; Zhu, M. Q.; Deng, X.; Zhang, X. M.; Wen, W.; Luo, Y.; He, Q. G., The Ordered and Disordered Nano-Intermetallic AuCu/C Catalysts for the Oxygen Reduction Reaction: The Differences of the Electrochemical Performance. *J. Electrochem. Soc.* **2017,** *164* (14), F1654−F1661.
217. Tee, S. Y.; Ye, E. Y.; Pan, P. H.; Lee, C. J. J.; Hui, H. K.; Zhang, S. Y.; Koh, L. D.; Dong, Z. L.; Han, M. Y., Fabrication of Bimetallic Cu/Au Nanotubes and Their Sensitive, Selective, Reproducible and Reusable Electrochemical Sensing of Glucose. *Nanoscale* **2015,** *7* (25), 11190−11198.
218. Parks, B. W.; Fritz, J. D.; Pickering, H. W., The Difference in the Electrochemical-Behavior of the Ordered and Disordered Phases of Cu3Au. *Scr. Metall.* **1989,** *23* (6), 951−956.
219. Zhang, N. L.; Chen, X.; Lu, Y. J.; An, L.; Li, X.; Xia, D. G.; Zhang, Z.; Li, J. X., Nano-Intermetallic AuCu3 Catalyst for Oxygen Reduction Reaction: Performance and Mechanism. *Small* **2014,** *10* (13), 2662−2669.
220. Chen, S. P.; Li, M. F.; Yu, S. M.; Louisia, S.; Chuang, W. L.; Gao, M. Y.; Chen, C. B.; Jin, J. B.; Salmeron, M. B.; Yang, P. D., Ligand Removal of Au25 Nanoclusters by Thermal and Electrochemical Treatments for Selective CO2 Electroreduction to CO. *J. Chem. Phys.* **2021,** *155* (5), 051101.
221. Zhang, H.; Liu, H.; Tian, Z. Q.; Lu, D.; Yu, Y.; Cestellos-Blanco, S.; Sakimoto, K. K.; Yang, P. D., Bacteria Photosensitized by Intracellular Gold Nanoclusters for Solar Fuel Production. *Nat. Nanotechnol.* **2018,** *13* (10), 900−905.

222. Tang, Q.; Lee, Y. J.; Li, D. Y.; Choi, W.; Liu, C. W.; Lee, D.; Jiang, D. E., Lattice-Hydride Mechanism in Electrocatalytic CO2 Reduction by Structurally Precise Copper-Hydride Nanoclusters. *J. Am. Chem. Soc.* **2017,** *139* (28), 9728−9736.
223. Zhu, Y.; Qian, H. F.; Drake, B. A.; Jin, R. C., Atomically Precise Au25(SR)18 Nanoparticles as Catalysts for the Selective Hydrogenation of α,β-Unsaturated Ketones and Aldehydes. *Angew. Chem., Int. Ed.* **2010,** *49* (7), 1295−1298.
224. Ross, M. B.; De Luna, P.; Li, Y. F.; Dinh, C. T.; Kim, D.; Yang, P.; Sargent, E. H., Designing Materials for Electrochemical Carbon Dioxide Recycling. *Nat. Catal.* **2019,** *2* (8), 648−658.
225. Ohta, T.; Shibuta, M.; Tsunoyama, H.; Negishi, Y.; Eguchi, T.; Nakajima, A., Size and Structure Dependence of Electronic States in Thiolate-Protected Gold Nanoclusters of Au25(SR)18, Au38(SR)24, and Au144(SR)60. *J. Phys. Chem. C* **2013,** *117* (7), 3674−3679.
226. Gao, X. H.; He, S. J.; Zhang, C. M.; Du, C.; Chen, X.; Xing, W.; Chen, S. L.; Clayborne, A.; Chen, W., Single Crystal Sub-Nanometer Sized Cu6(SR)6 Clusters: Structure, Photophysical Properties, and Electrochemical Sensing. *Adv. Sci.* **2016,** *3* (12), 1600126.
227. Dolamic, I.; Knoppe, S.; Dass, A.; Burgi, T., First Enantioseparation and Circular Dichroism Spectra of Au38 Clusters Protected by Achiral Ligands. *Nat. Commun.* **2012,** *3*, 798.
228. Narouz, M. R.; Osten, K. M.; Unsworth, P. J.; Man, R. W. Y.; Salorinne, K.; Takano, S.; Tomihara, R.; Kaappa, S.; Malola, S.; Dinh, C. T.; Padmos, J. D.; Ayoo, K.; Garrett, P. J.; Nambo, M.; Horton, J. H.; Sargent, E. H.; Hakkinen, H.; Tsukuda, T.; Crudden, C. M., N-Heterocyclic Carbene-Functionalized Magic-Number Gold Nanoclusters. *Nat. Chem.* **2019,** *11* (5), 419−425.
229. Kim, B.; Seong, H.; Song, J. T.; Kwak, K.; Song, H.; Tan, Y. C.; Park, G.; Lee, D.; Oh, J., Over a 15.9% Solar-to-CO Conversion from Dilute CO2 Streams Catalyzed by Gold Nanoclusters Exhibiting a High CO2 Binding Affinity. *ACS Energy Lett.* **2020,** *5* (3), 749−757.
230. Zhang, B.; Chen, C. B.; Chuang, W.; Chen, S. P.; Yang, P. D., Size Transformation of the Au22(SG)18 Nanocluster and Its Surface-Sensitive Kinetics. *J. Am. Chem. Soc.* **2020,** *142* (26), 11514−11520.
231. Kauffman, D. R.; Thakkar, J.; Siva, R.; Matranga, C.; Ohodnicki, P. R.; Zeng, C. J.; Jin, R. C., Efficient Electrochemical CO2 Conversion Powered by Renewable Energy. *ACS Appl. Mater. Interfaces* **2015,** *7* (28), 15626−15632.
232. Li, M.; Zhang, B.; Cheng, T.; Yu, S.; Louisia, S.; Chen, C.; Chen, S.; Cestellos-Blanco, S.; Goddard, W. A.; Yang, P., Sulfur-Doped Graphene Anchoring of Ultrafine Au25 Nanoclusters for Electrocatalysis. *Nano Res.* **2021,** *14* (10), 3509−3513.

233. Shivhare, A.; Chevrier, D. M.; Purves, R. W.; Scott, R. W. J., Following the Thermal Activation of Au25(SR)18 Clusters for Catalysis by X-ray Absorption Spectroscopy. *J. Phys. Chem. C* **2013,** *117* (39), 20007−20016.
234. Hakkinen, H., The Gold−Sulfur Interface at the Nanoscale. *Nat. Chem.* **2012,** *4* (6), 443−455.
235. Burgi, T., Properties of the Gold−Sulphur Interface: From Self-Assembled Monolayers to Clusters. *Nanoscale* **2015,** *7* (38), 15553−15567.
236. Liu, J.; Krishna, K. S.; Losovyj, Y. B.; Chattopadhyay, S.; Lozova, N.; Miller, J. T.; Spivey, J. J.; Kumar, C. S. S. R., Ligand-Stabilized and Atomically Precise Gold Nanocluster Catalysis: A Case Study for Correlating Fundamental Electronic Properties with Catalysis. *Chem. Eur. J.* **2013,** *19* (31), 10201−10208.
237. Tian, S. B.; Liao, L. W.; Yuan, J. Y.; Yao, C. H.; Chen, J. S.; Yang, J. L.; Wu, Z. K., Structures and Magnetism of Mono-Palladium and Mono-Platinum Doped Au25(PET)18 Nanoclusters. *Chem. Commun.* **2016,** *52* (64), 9873−9876.
238. Zhu, M.; Aikens, C. M.; Hollander, F. J.; Schatz, G. C.; Jin, R., Correlating the Crystal Structure of a Thiol-Protected Au25 Cluster and Optical Properties. *J. Am. Chem. Soc.* **2008,** *130* (18), 5883−5885.
239. Heaven, M. W.; Dass, A.; White, P. S.; Holt, K. M.; Murray, R. W., Crystal Structure of the Gold Nanoparticle [N(C8H17)4][Au25(SCH2CH2Ph)18]. *J. Am. Chem. Soc.* **2008,** *130* (12), 3754−3755.
240. Liu, M.; Pang, Y. J.; Zhang, B.; De Luna, P.; Voznyy, O.; Xu, J. X.; Zheng, X. L.; Dinh, C. T.; Fan, F. J.; Cao, C. H.; de Arquer, F. P. G.; Safaei, T. S.; Mepham, A.; Klinkova, A.; Kumacheva, E.; Filleter, T.; Sinton, D.; Kelley, S. O.; Sargent, E. H., Enhanced Electrocatalytic CO2 Reduction via Field-Induced Reagent Concentration. *Nature* **2016,** *537* (7620), 382−386.
241. Lu, L. F.; Lou, B. H.; Zou, S. H.; Kobayashi, H.; Liu, J. J.; Xiao, L. P.; Fan, J., Robust Removal of Ligands from Noble Metal Nanoparticles by Electrochemical Strategies. *ACS Catal.* **2018,** *8* (9), 8484−8492.